KU LEUVEN

FACULTY OF SCIENCE

Extrapolation of the Solar Coronal Magnetic Field by Means of an Optimization Method

Nicolas WIJSEN

Supervisor: Prof.Dr. S. Poedts
KU Leuven

Co-supervisor: Dr. J. Pomoell
University of Helsinki

Co-supervisor: Prof.Dr. E. Kilpua
University of Helsinki

Thesis presented in
fulfillment of the requirements
for the degree of Master of Science
in Astronomy and Astrophysics

Academic year 2015-2016

Preface

This thesis is written as completion to the the master Astronomy and Astrophysics, at the KU Leuven. Part of the thesis was accomplished during a four month stay at the University of Helsinki. This work would not have been possible without the help of my supervisors Stefaan Poedts, Emilia Kilpua, and Jens Pomoell.

I would like to thank Stefaan Poedts for giving me valuable advice and guidance throughout this project. He opened the window to the world of solar physics for me, and provided me the opportunity to accomplish part of my thesis at the University of Helsinki, which has been a wonderful and memorable experience.

Next, I would like to thank Emilia Kilpua for her support, suggestions and intellectual guidance during my stay in Helsinki. She gave me opportunities to participate in the research program, and to work with talented members of the research staff, for which I am very grateful.

Great thanks go to Jens Pomoell for his immense support, constant encouragement, and valuable advice from the very early stage of this research. His endless patience and training in all aspects of being a good solar scientist are greatly appreciated and will not be forgotten. Without him, this thesis would not have been completed or written.

Last but not least, I would like to thank my parents for their continued support and endless encouragement during my studies. Without them, this journey would not have been possible.

Scientific Summary

The solar atmosphere is a highly dynamical environment, producing lots of interesting phenomena. Among these phenomena are transient eruptive events that can strongly affect the conditions in interplanetary space and Earth's upper atmosphere. It is thus of crucial importance to gain a deep understanding of these phenomena. These eruptive events are believed to be powered by the magnetic field of the corona. Since it is really difficult to measure the coronal magnetic field, insight needs to be obtained by developing three-dimensional fields models. In most regions of the corona, the dynamics are governed by the magnetic field, rather than by the thermal pressure or gradient or gravity. As a consequence, it is often justified to neglect both thermal pressure gradients and gravity. This means that the Lorentz force exerted by the magnetic field is in balance with itself, i.e., the Lorentz force vanishes. Magnetic fields satisfying this condition are referred to as force-free fields.

In this work we will use the force-free assumption to model the coronal field above the solar active region. We review the mathematical framework of force-free fields, and discuss several methods that aim at reconstructing the coronal magnetic using the force-free assumption. These methods try to extrapolate the coronal field, starting from measurements of the magnetic vector at the photosphere. A problem is that these extrapolation methods assume a force-free field in the whole computational domain, whereas the photospheric magnetic field is not force-free. Consequently, the photosperic magnetogram needs to be transformed into a force-free chromospheric magnetogram, such that it can be used as boundary condition for the extrapolation methods. This process is generally referred to as preprocessing, and a numerical implementation of a preprocessing method is discussed in this thesis.

One of the extrapolation methods tries to reconstruct the coronal field by means of an optimization method. The major emphasis of this thesis is on the performance of this method and the results that it returns when applied to real solar data. A numerical implementation of the optimization method is discussed and subsequently tested using various different semi-analytical force-free models of solar active regions. We find that our optimization method is able to reproduce these semi-analytical test field reasonably well, both in a quantitative and qualitative way. We find that the optimization method performs best when considering a lower central volume in the computational domain. Such an inner box is the region where the effects of the boundary conditions are the weakest and the electrical currents and the magnetic fields the strongest. In addition, our results are observed to be better than the results obtained by Schrijver et al. (2006), who uses a different set of extrapolation methods. The optimization method is also observed to be able to reproduce magnetic fields that contain a flux-rope structure.

In the final part of the thesis, we used the optimization method to study the evolution of NOAA active region 12371 over a period of seven days. During this period, the AR showed significant flare activity and three CMEs were observed. The series of extrapolated fields showed a sheared arcade evolving into a flux-rope structure. Combining this result with the observations of a decreasing photospheric magnetic flux and an increasing free magnetic energy, we find strong evidence that a major flux cancellation event according to the model developed by van Ballegooijen & Martens (1989), resulted in the formation of a magnetic flux-rope. In addition, we remark that the existence of this flux-rope was confirmed as a filament-like structure in AIA EUV images.

Our findings suggest that a flux-rope can be present well before the onset of a CME. In addition, our results support the idea that a flux-rope does not need to erupt in its entirety to cause a CME. Studying the energetics of the magnetic fields before and after the eruptive events on 21 and 22 June 2015, we find an energy redistribution that is consistent with a magnetic implosion of the coronal field. Such an implosion is a consequence of a reduced magnetic pressure after solar flares and CMEs.

We studied the stability of the magnetic flux-rope against the torus instability, about three hours before the CME on 25 June. Our results showed that at that time the flux-rope was located in a region stable against the torus instability, yet a small expansion of the flux-rope would make it torus unstable. A clear shift of energy towards higher altitudes present in the extrapolations of 25 June, may be a signature of an expanding motion of the flux-rope. Therefore the torus instability should be regarded as a possible trigger mechanism of the CME on 25 June.

Finally, we find that the performance of the optimization method can show a strong spatial dependence within a single extrapolation. When using space-averaged metrics to quantify the goodness of the results, a good performance in one part of the computational volume may mask a bad performance in another part of the computational volume. This may lead to erroneous estimates of global variables like the total energy content of the magnetic field. To detect and prevent such errors, we recommend using spatial-dependent metrics in addition to space-averaged metrics, before performing any physical analysis of the extrapolated fields.

Vulgarising Summary

The Sun is a highly dynamical object, producing energetic phenomena like bright solar flares and violent eruptions called coronal mass ejections (CMEs). During these eruptions, the Sun hurls a billion-ton cloud of charged particles into space. When striking Earth, these eruption may, among other things, disrupt satellites, knock out power systems, and endanger human life in space. It is thus crucial to understand and predict these CMEs and their effects on the environmental conditions in outer space. This is only possible if the mechanism that creates these eruptive events is understood well. There is a consensus in the heliophysics community that solar eruptive events like flares and CMEs are powered by the magnetic field in the upper solar atmosphere, i.e., in the solar corona. Understanding CMEs and flares requires thus knowledge about the structure and evolution of the coronal magnetic field. This turns out to be a very challenging task, since it requires knowledge of a large variety of complex physical processes.

A major problem is that it is very hard to measure the magnetic field of the corona directly. Instead, most of our measurements provide data about the magnetic field in the lower solar atmosphere, i.e., in the photosphere. As a consequence, models need to be developed to reconstruct the coronal magnetic field, starting from the measurements of the photospheric magnetic field. In this thesis, we use such a model to study the three dimensional structure of the coronal magnetic field above solar active regions. These are regions that show enhanced magnetic activity, from which CMEs and flares are often observed erupting.

This thesis consists of two major parts. The first part is devoted to testing a numerical method that tries to reconstruct the coronal magnetic field. The performance of this method is tested by using some analytical magnetic field models of solar active regions. We find that the method is able to reconstruct the magnetic fields reasonably well. In the second part of the thesis, this reconstruction method is used to study the magnetic field of a specific active region of the Sun. This active region was visible on the solar disk from 19 June to 25 June, 2015. During this period, several flares and CMEs erupted from this active region. We find that the reconstructed magnetic field corresponds well with the observations of the active region, although there is still room for improvement.

Contents

Chapter 1

Introduction

For human beings, the Sun is without doubt the most important celestial object. Allowing liquid water to flow on Earth's surface, and providing organisms the necessary energy to grow through processes like photosynthesis, the Sun can be considered as the bringer of life on Earth. Moreover, the upraise of solar energy as renewable energy source, both in industry and households, proves once more the importance of the Sun. Whereas the Sun looks from Earth like a calm and unchangeable celestial object, the actual truth about the Sun could not be further away. Space missions in the twentieth centuries have illustrated that the Sun has also a "dark side", posing a direct threat to our high-tech societies.

The Sun is a highly dynamical object, producing energetic phenomena like solar flares and violent eruptions called coronal mass ejections (CMEs). A lot of research has been devoted to the understanding of these intrinsically magnetic phenomena. Especially CMEs have received a lot of attention in the past few years, as they are thought to be the main drivers of major geomagnetic storms at Earth. These geomagnetic storms are characterized by large disturbances in the magnetic field of the Earth. If strong enough, geomagnetic storms may induce electric currents at ground level that damage transformers in power grids. For example, the geomagnetic storm that struck Earth on 13 March 1989 damaged the power transmission system of Quebec in Canada, resulting in an electrical blackout that lasted nine hours.

In addition, CMEs can drive shock waves in which particles are accelerated to relativistic speeds. These particles are called solar energetic particles (SEP), and are also often generated in major flare sites. On impact, SEPs may cause severe damage to the electronics of satellites, and disrupt navigation systems. In addition, they pose a severe threat for astronauts in space, and they can disrupt radio communication (Committee On The Societal & Economic Impacts Of Severe Space Weather Events 2008). Understanding the physics of events like CMEs, flares and SEPs is thus essential to anyone working with one of the aforementioned technologies.

Events like CMEs, flares, and SEPs are often referred to as *space weather* events. According to the definition of the U.S. National Space Weather Plan, space weather refers to:

> Conditions on the Sun and in the solar wind, the magnetosphere, ionosphere, and thermosphere that can influence the performance and reliability of space-born and ground-based technological systems and that can affect human life and health.

Since damaging effects of space weather events can often be reduced by taking precautionary measures, an accurate space forecast would be highly valuable. However, developing such a space weather forecast turns out to be a very challenging task. This is because it requires a profound understanding of different physical processes occurring in a wide range of environments. Understanding geomagnetic storms requires a good understanding of the drivers of these storms, mostly CMEs. These CMEs are formed in complex processes occurring in the solar atmosphere, most of which are still poorly understood. A good space weather forecast also requires a profound understanding of the physics of the interplanetary medium and the Earth's magnetosphere and ionosphere. Apart from having their own complex dynamics, these environments are also coupled in a far from trivial manner. This coupling can be realized trough shocks, magnetic fields, electric currents, plasma dynamics, etc. (Schwenn 2006; Pulkkinen 2007).

Understanding space weather phenomena thus requires knowledge about a broad range of space environments and processes with completely different physical properties. This often forces researchers to specialize in a specific sub-domain, focussing on only a small part of the "big picture". Developing a good space weather forecast requires the combination of all these sub-domains in a consistent way. This has turned out to be a major challenge. Several attempts have been made by several research groups and institutes, with major contributions from the Space Weather Prediction Center at NOAA in the US, and from the Solar Influences Data Center of the Royal Observatory of Belgium. Despite some major improvements, the accuracy and reliability of the existing forecast methods is still relatively poor (Singer et al. 2013). Our high-tech society remains thus largely unwarned and unprotected against the vicissitudes of the Sun.

This thesis will focus on the solar coronal magnetic field. Understanding the evolution of the coronal magnetic field is essential since the major drivers of space weather, CMEs, are intrinsically magnetic phenomena originating from the solar corona. This chapter introduces the basic properties of the Sun, focussing on the solar atmosphere. The emphasis will be on the magnetic properties of the solar atmosphere, since almost every event occurring in the solar atmosphere has a magnetic origin. We will talk about active regions, flux-ropes, prominences and filaments, solar flares and CMEs. Apart from that we will also devote a section to how solar magnetic fields can be observed, and what the limitations are. We conclude by giving the scope and the outline of this thesis.

1.1 The Solar Magnetic Field

The majority of space weather phenomena, like CMEs and flares, essentially owe their existence to the solar magnetic field. The wide variety of phenomena is a consequence of the different ways the solar plasma responds to the underlying magnetic field evolution. Especially in the solar corona, where the ratio of the plasma to the magnetic pressure is much smaller than unity, the dynamics and the structures are controlled by the magnetic field. In this section we will briefly review the general properties of solar magnetism.

1.1.1 Origin of Solar Magnetism

The solar magnetic field is believed to be generated by a combination of convective motions and differential rotation. These plasma motions drive a *solar dynamo*, which converts mechanical energy into magnetic energy. This dynamo process can be studied either by looking to magnetic phenomena present in the solar atmosphere, or by using helioseismology to probe the interior of the Sun.

By studying solar oscillations, the Sun's internal rotation can be deduced. In doing so, a narrow shear layer, called the *tachocline* (Spiegel & Zahn 1992), located between the radiative zone and the convective zone was discovered. In this transition layer, the rotation changes from a nearly uniform rotation in the radiative interior, to a latitude dependent rotation in the convection zone (Elsworth et al. 1995). This dependence on latitude is illustrated in Fig. 1.1. It is now believed that the tachocline is the layer where the solar dynamo is active. The rapidly changing angular velocity at the tachocline, may induce all kind

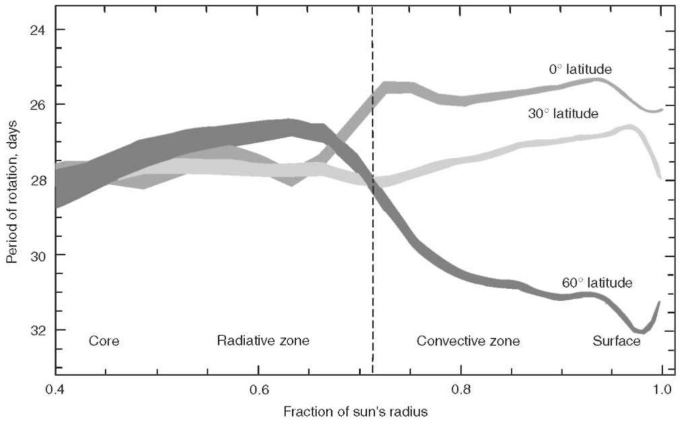

Figure 1.1: The latitude dependence of the internal rotation of the Sun. These rotation profiles have been inferred using data from the Michelson Doppler Imager on board Solar and Heliospheric Observatory (SOHO). Below the convection zone, the different latitudes appear to rotate more or less at the same pace. Figure adapted from Kosovichev et al. (1997)

of instabilities that can contribute to the solar dynamo. For a profound discussion about the tachocline, the reader is referred to Hughes et al. (2007)

Apart from helioseismology, the magnetic phenomena observed in the solar atmosphere also provide constraints for any model of the solar magnetic field. For example, a consistent, time-dependent model of the solar magnetic field should be able to reproduce the solar cycle (see below) and all its associated magnetic phenomena. Developing a dynamo model that reproduces all the known features of the solar magnetic field has proven to be a formidable task. It is fair to say that, despite some major progress made in the past decades, a consistent dynamo theory is still far from completion (Charbonneau 2010).

1.1.2 The solar Cycle

The *solar cycle* is a cycle of about 11 years, during which the magnetic polarity of the Sun is reversed. This means that after about 22 years, the original magnetic configuration is restored. A first indication of the solar cycle was discovered by studying the temporal evolution of the number of *sunspots* covering the Sun. Sunspots are features that appear as dark patches on the solar surface. They will be discussed in more detail in Section 1.2.1. The total number of sunspots covering the Sun varies constantly, yet, when plotting the number of sunspots versus time, a cyclic pattern with a period of 11 years becomes visible.

The period during which the solar magnetic field is closest to dipolar is called *solar minimum*, since then almost no sunspots cover the Sun. When the magnetic poles start reversing, the magnetic field becomes more and more complex. Halfway between two successive solar minima, the solar field is most complex. During this period, which is called *solar maximum*, the Sun typically contains several sunspots.

Since the solar magnetic field plays a prominent role in many solar phenomena, it is not surprising that this magnetic oscillation has profound effects on the solar activity. Near the solar minimum, the Sun produces about one CME every five days. Near the solar maximum, this number amounts to about three CMEs every day. Similarly, during the solar minimum there can be long periods of time during which no detectable flares occur, whereas during the solar maximum multiple flares occur on a daily base (Priest 2014).

1.2 The Solar Atmosphere and its Magnetic Features

The solar atmosphere is defined as the region from which photons can escape directly into space. This corresponds to the region that has optical depth smaller than $\sim 2/3$. Traditionally it is divided into three major regions: the *photosphere*, the *chromosphere*, and the *corona*. These regions have their own physical characteristics, which strongly differ from each other. However, despite these profound differences, the regions are strongly connected and influenced by each other through a multitude of magnetic, thermal and dynamical processes. As a result, the solar atmosphere is a highly variable environment that is spatially inhomogeneous on almost all scales.

From past observations, it has become clear that the inhomogeneity of the solar atmosphere results in a whole zoo of different physical phenomena. The cause of these phenomena strongly depends on the local properties of the plasma. Some phenomena are almost solely governed by gas dynamics, whereas other, especially eruptive phenomena, are intrinsically magnetic in nature. However, it is fair to say that at present, observations tend to be far ahead of theory. Indeed, the satellites and ground-based telescopes have improved tremendously over the recent decades in sensitivity, spectral coverage, and spatial resolution. This has resulted in the discovery of an unanticipated diversity of phenomena, for which good theoretical frameworks are still lacking. This section gives an overview of the properties of the different regions of the solar atmosphere, with emphasis on their magnetic features related to solar activity. A more in-depth discussion of the solar atmosphere can be found in Solanki & Hammer (2002); Wiegelmann et al. (2014) and Priest (2014).

1.2.1 The Photosphere

The photosphere is the region from where the majority of the photons escape into interplanetary space. Therefore, it can be regarded as the surface of the Sun. The continuous spectrum of the photosphere closely resembles that of a black body with an effective temperature of about 5778 K. The temperature varies from about 6000 K at the lower boundary, down to 5000 K at the upper boundary. Superimposed on the continuous spectrum, several absorption lines can be detected in the solar spectrum. The majority of these absorption lines originate from the photosphere. The absorption lines in the optical spectrum of the Sun are called the Fraunhofer lines, after the German physicist Joseph von Fraunhofer. Since the photosphere is relatively dense and opaque, most of these lines, except the weakest ones, are optically thick. As will be discussed in Section 1.3, some of these lines can be used to probe the photospheric magnetic field.

As illustrated in Fig. 1.2, the photosphere is covered by millions of cell-looking features, called *granules*. Granules typically have a diameter of about 1000 km, and dissipate over timescales of some minutes. They are the result of underlying convective motions. More precisely, they mark the upper boundary untill which plasma blobs can overshoot the outer convection zone of the Sun. Moreover, these convective motions constantly carry new magnetic flux towards the solar atmosphere. As a consequence, the photospheric magnetic field shows strong temporal variations and is highly inhomogeneously distributed.

The strongest magnetic concentrations are found in small, but intense flux tubes called *magnetic elements*. These tubes typically have a radius of about 100 km, and a vertical magnetic field of several kG. Going towards the upper regions of the photosphere, these flux tubes spread out, causing their magnetic field to decrease to some hundreds of G in magnitude. Moreover, these flux concentrations are often highly dynamic features, undergoing almost contentious fragmentation, merging and cancellation processes.

The most notable features of the photosphere are without doubt the *sunspots*. Section 1.1 already briefly

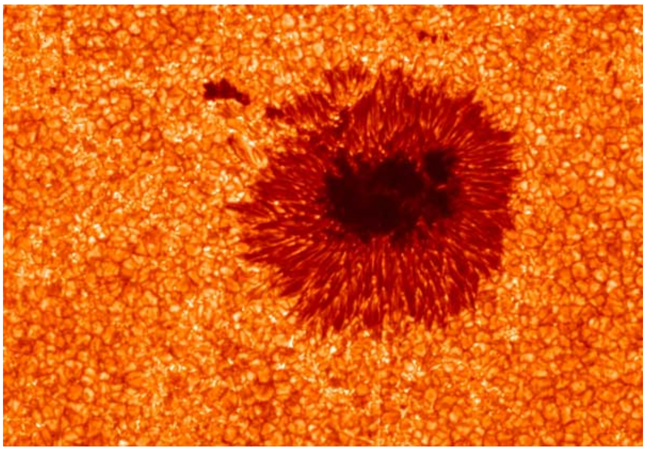

Figure 1.2: Granules surrounding a sunspot. The darkest part of the sunspot is the umbra, while the reddish part is the penumbra (courtesy of NASA).

discussed the relationship between sunspots and the solar cycle. Here we focus on the intrinsic properties of individual sunspots. Sunspots are relatively large (~ 40000 km) areas, that can sometimes be seen with naked eye during dusk or dawn. Solar sunspots can have a temperature of more than 1500 K below the temperature of the surrounding photosphere. With the usual exposure times, this contrast makes sunspots appear as dark spots on the photospheric surface. A Sun spot can be divided into two regions: a central dark *umbra*, surrounded by a filamentary, somewhat brighter *penumbra*. This division is clearly visible in the sunspot shown in Fig. 1.2. The umbra contains a very strong vertical magnetic field, up to several kG. This strong vertical magnetic field is believed to suppress convection, which explains the lower temperatures. In the penumbra, the magnetic field decreases in strength and becomes more and more horizontal.

Often, sunspots appear in pairs of different magnetic polarity that are connected with each other through coronal loops and/or filaments. These structures will be discussed in Section 1.2.3. Finally, we remark that most CMEs and flares are observed to originate from regions that contain one or more sunspots.

1.2.2 The Chromosphere

The chromosphere is located just above the photosphere. Compared to the photosphere, the chromosphere is a very dilute plasma with a density that is about 10^{-4} times smaller than the photospheric density. As a consequence, the chromosphere is optically thin in most wavelengths, apart from some strong spectral lines. Without filters it can only be observed at the start and the end of a solar eclipse. Outside of eclipses, spectral lines like the Hα Balmer line or the Ca II K line can be used to probe different layers in the chromosphere. The study of the spectral lines has shown that the temperature of the chromosphere decreases from about 6000 K at the inner boundary, to a minimum of approximately 3800 K. Afterwards, the temperature starts increasing again, such that the outer boundary has a temperature of ~ 25000 K. In contrast to the temperature, the plasma density decreases rapidly outwards.

On top of the chromosphere, there is thin layer which is called the *transition region*, marking the separation between the chromosphere and the corona. The transition region is characterised by a very large temperature and density gradient. Over a distance of only $\sim 100\mathrm{km}$, the temperature jumps with two orders of magnitude while the plasma density decreases with two orders of magnitude.

Like the photosphere, the magnetic field of the chromosphere is highly structured and dynamic. A difference between the photosphere and the chromosphere, is that in the photospheric magnetic fields appear to be mainly radially oriented, while in the chromospheric magnetic fields expand in all directions. Apart from that, the chromosphere is also the region where magnetic forces start to dominate the thermal gas pressure. This is often stated using the parameter β, which is defined as the ratio of the magnetic pressure to the thermal pressure. In the chromosphere β varies from a value larger than unity to $\beta \ll 1$. The height at which the transition from $\beta > 1$ to $\beta < 1$ occurs, varies strongly with position. Above a solar active region, $\beta \ll 1$ can already be reached at heights of about ~ 400 km above the photosphere Gary (2001). In contrast, in quiet solar region environments, the magnetic forces will only start to dominate at heights between 800 km and 1.6 Mm above the solar surface (Rosenthal et al. 2002).

Several chromospheric phenomena can be related to the magnetic field. When the chromosphere is seen in the red light of hydrogen, dark filaments are observed on the solar disk, whereas bright gaseous features are observed on the limb. Both observations are manifestations of the same phenomena viewed from a different perspective. These structures are called solar *prominences* and are discussed in Section 1.2.3.3. Apart from these prominences, the magnetic field also gives rise to phenomena like *plages* and *spicules* (see, e.g, de Pontieu et al. 2007; De Pontieu et al. 2004).

1.2.3 The Corona

The outer part of the solar atmosphere is called the corona, an extremely rarefied and hot plasma. It can be seen during a total solar eclipse as a highly structured glow around the solar disk. Alternatively, a coronagraph can be used to produce an artificial eclipse. The corona is optically thin in almost all wavelengths, and its spectrum shows emission lines of highly ionized heavy elements like calcium and iron. Less heavy elements, like oxygen and carbon, do not produce any spectral lines since they are completely ionized. This high degree of ionization indicates that the corona is an extremely hot plasma, with a temperature in excess of a million degree. The origin of this high temperature is still a major open-problem in solar physics, known as the *coronal heating problem.*

The extremely high temperature makes the corona a bright X-ray source. The first high resolution X-ray images of the corona were taken in the early 70s by the Skylab space station. These images made clear that the corona is a very structured and complex region. The complexity of the corona is essentially a consequence of the corona being a low β environment. This means that the magnetic pressure dominates the plasma pressure, and hence plasma transport across the magnetic field is strongly inhibited . Plasma is thus forced to flow in a 1D direction along the magnetic field lines. A priori, one could think that this largely simplifies the structure of the corona. However, the complex topology of the coronal magnetic field makes the corona a highly inhomogeneous region with a complicated density profile. Coronal magnetic phenomena include coronal holes, helmet streamers, loop arcades, soft X-ray jets, postflare loops, cusp-shaped loops, sigmoid structures and prominences. The differences found in these phenomena are essentially due to differences in the underlying magnetic topology.

1.2.3.1 Coronal Holes

Coronal holes are regions that appear as large dark patches in X-ray and extreme ultraviolet (EUV) images. An example of a coronal hole is given in panel (a) of Fig. 1.3. These regions are penetrated by open magnetic field lines, along which plasma is able to escape from the Sun. This escaping plasma that is believed to be the source of the fast solar wind. Another consequence of this plasma escaping the Sun is that these regions have a lower density and a lower temperature than the surrounding corona. This explains why they appear dark on X-ray images. During the solar minimum, large coronal holes normally cover both poles. When the solar cycle proceeds, these polar coronal holes will start shrinking, until they completely disappear around the solar maximum. Moreover, as the solar maximum approaches, more

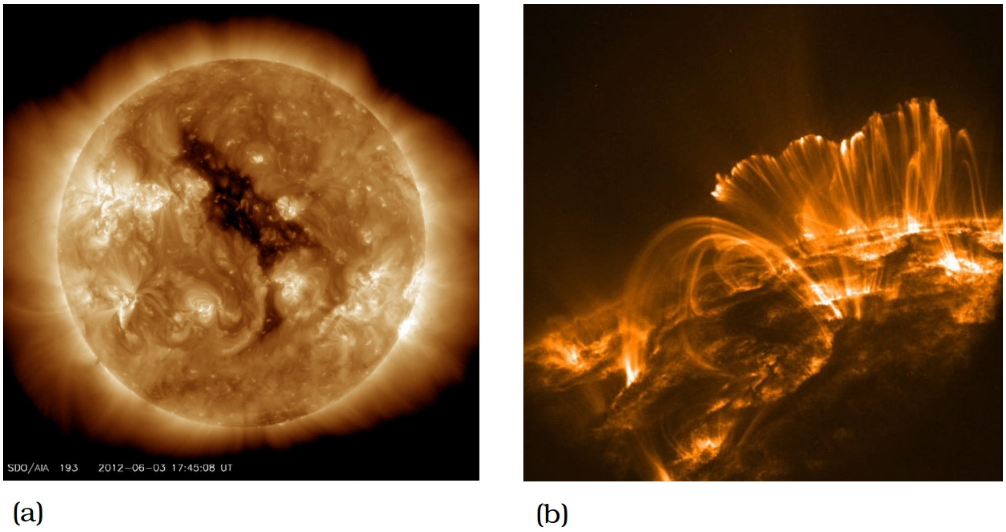

Figure 1.3: (1) EUV image (193Å) of the Sun, taken by the Atmospheric Imaging Assembly (AIA) on board of the Solar Dynamics Observatory (SDO). The black patch is a coronal hole, while the bright white regions are active regions. (b) Solar coronal loops, constituting a coronal arcade. Image taken by by the Transition Region And Coronal Explorer (TRACE).

coronal holes will form at lower latitudes. In contrast to the coronal holes at the poles, these low latitude coronal holes only exist for a few months.

1.2.3.2 Active Regions

In contrast to coronal holes, active regions are areas where most magnetic field lines appear in loops, closing on the solar surface (see Fig. 1.3). These field lines can either connect different polarity regions inside the active region, or they can interconnect different active regions with one another. Active regions are regions with enhanced solar activity. They are characterised by the appearance of sunspots, dynamic magnetic fields and enhanced electromagnetic emission. Moreover, active regions are the locations where CMEs and flares often originate from. These eruptive events are the product of non-stopping magnetic activity, like magnetic flux emergence, flux cancellation, and magnetic reconnection processes.

Most active regions are bipolar in nature, which explains why on an X-ray image, active regions will show several bright loops. These bright coronal loops are anchored in the photosphere, where they connect regions of opposite polarity. Often the zones with opposite polarity have large lateral extent, so that multiple coronal loops form next to each other. Such a loop system is called a loop arcade, and an example is shown in panel (b) of Fig. 1.3. The loops appear bright because plasma heating in the footpoints of the loops causes upflows of hot plasma into the coronal loops. As a result, these loops are hotter and denser than the surrounding corona. A single loop has typically a lifetime of about one day, yet the whole loop arcade may exist for several solar rotations. Moreover, during its lifetime, new magnetic flux may emerge into the active region. This new flux may have a different orientation, which leads to flux cancellation and magnetic reconnection processes. These processes can result in active transient phenomena like flares and CMEs.

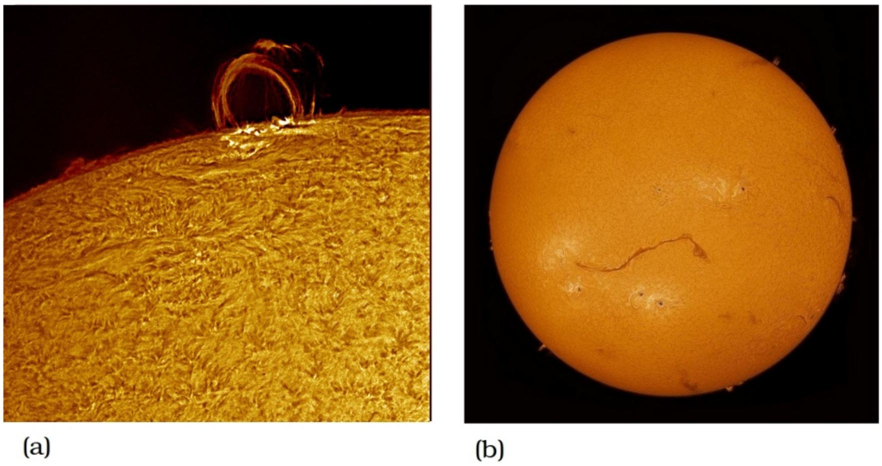

Figure 1.4: (a) Hα image of a prominence (upper right corner) (credit: Jack Newton). (b) Hα image of the Sun. The dark streak close to the center of the Sun is a solar filament (credit: Paul Andrew).

1.2.3.3 Solar Filaments and Magnetic Flux Ropes

Another feature appearing in the corona are *solar prominences*, which are large elongated plasma concentrations, suspended in the corona. The plasma of a prominence is much cooler and denser than the coronal plasma, and therefore prominences appear as thin, dark, filaments on Hα photographs of the solar disc (see panel (b) of Fig. 1.4). In contrast, when these structures are observed on coronagraph pictures, they appear as bright loops (see panel (a) of Figure 1.4). Depending on their location, three different types of filaments can be distinguished. *Quiescent prominences* appear outside active regions, *intermediate prominences* appear on the boundary of active regions, and *active-region prominences* are found inside active regions. In general, an active-region prominence has a much shorter lifetime and is much smaller in size than an quiescent prominence. Despite these differences between the three types, observations indicate that they have a similar structure and formation mechanism.

Filaments are located above polarity inversion lines (PILs). These are boundaries across which the polarity of the solar magnetic field reverses. The magnetic field inside prominences tends to be almost horizontal, aligned with the PIL. Remark that a horizontal magnetic field is a necessary requirement for having a vertical Lorentz force. Such a vertical force is necessary to balance the downward directed gravity. These horizontal fields can be curved either upward or downward. The latter is usually called a *magnetic dip*, and it is expected that filaments are located in such dips. Without these dips, gravity would pull this dense filament-plasma rapidly towards the solar surface, unless there is some other, non-magnetic force counteracting gravity.

Moreover, prominences tend to have inverse polarity, which means that the magnetic field inside filaments points from the negative side of the PIL to the positive side of the PIL. Prominences are thus embedded in highly non-potential magnetic fields, exhibiting strong magnetic shear. A prominence is often surrounded by a region of reduced density, called the *coronal cavity*. The above observations suggest that a filament is embedded in a *magnetic flux-rope*, although other explanations are also possible (Mackay et al. 2010). An illustration of a magnetic flux-rope is given in panel (a) of Fig. 1.5. This flux-rope in particular is a realisation of a semi-analytical model developed by (Titov & Démoulin 1999), and will be discussed in more detail in Section 2.4.1.2. In the flux-rope model, the rope is located horizontally above the PIL, with the prominence located in the lower concave part of the flux-rope. Panel (b) of Fig. 1.5 shows cross-sections of different possible magnetic topologies of flux-ropes. The gray patches located in the magnetic dips represent the filament plasma. The coronal cavity corresponds to the centre and upper part of the flux-rope.

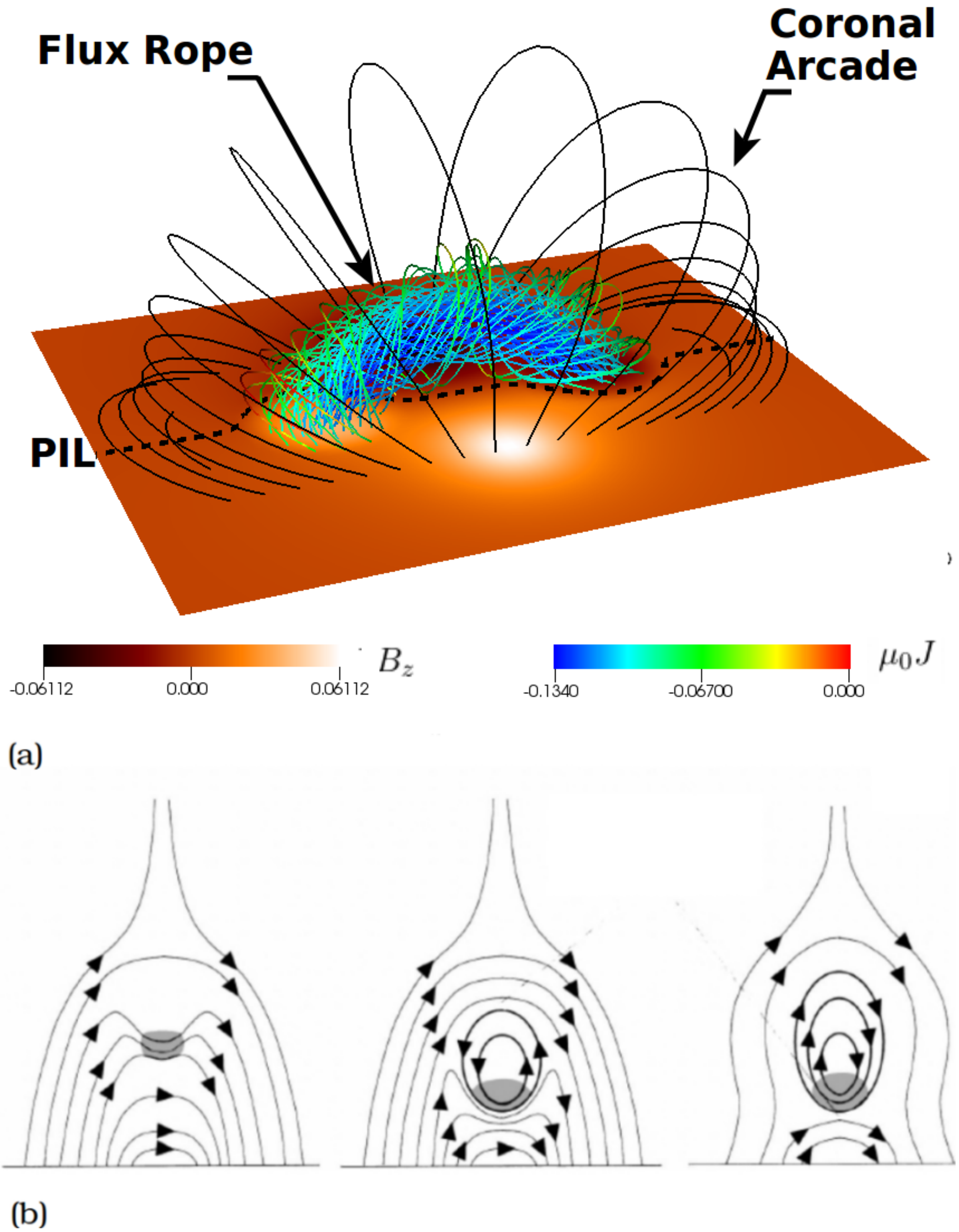

Figure 1.5: (a) Model of a flux-rope. The orange color-scale gives the vertical magnetic field, whereas the “rainbow”-color scale is proportional to the current density. (b) Schematic representation of three possible magnetic field topologies in a cross-section of a prominence. The gray patches, located in magnetic dips, represent the filament plasma. Image adapted from Gilbert et al. (2001).

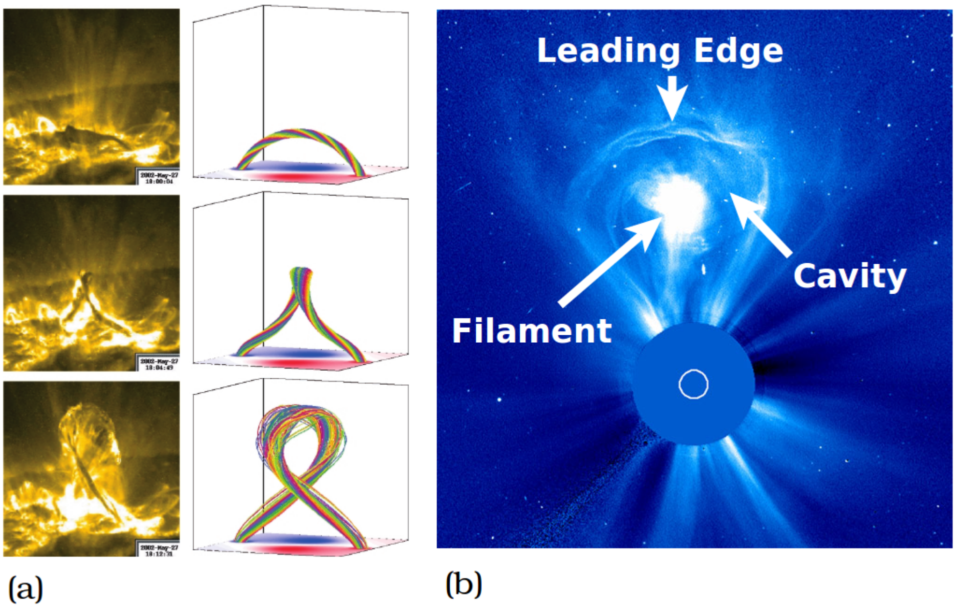

Figure 1.6: (a) The left column shows 195 Å images of a filament subjected to the kink instability. The images were taken by Transition Region and Coronal Explorer (TRACE) on May 27, 2002. The right column shows a simulation of the magnetic field of the filament. Image from Török & Kliem (2005). (b) A classic three-part CME observed by the Large Angle and Spectrometric Coronagraph Experiment (LASCO) on board of SOHO.

Coronal arcade structures overly flux-ropes. These coronal arcades are shown in panel (a) of Fig. 1.5 as black loops. The magnetic tension forces provided by these arcades are necessary to keep the flux-rope close to a stable magneto-static equilibrium. Without these arcades, the flux-rope would not be in force balance with its surroundings. Another important parameter for stability concerns the twist of the flux-rope. If the twist of the flux-rope exceeds some critical value (the *Kruskal-Shafranov criterion*), the rope becomes susceptible to the *kink instability* (Török & Kliem 2004). The amount of twist in a flux-rope may vary over time. Vortex motions at the footpoints of flux-ropes may increase the twist in the flux-rope, making the flux-rope eventually unstable (Hood & Priest 1981). An illustration of a filament subjected to a kink instability is shown in panel (a) of Fig. 1.6.

1.2.3.4 Coronal Mass Ejections

Coronal mass ejections are enormous solar eruptions, ejecting a huge cloud of magnetized plasma into interplanetary space. As already mentioned in the beginning of this chapter, the potential dangerous effects of CMEs c on our society make the development of good space weather forecast models essential. Achieving this is only possible if both the launching mechanism and the subsequent CME evolution are well understood. It is generally accepted that CMEs are powered by the magnetic field in the lower corona. The energy necessary for the eruption is the free energy stored in highly non-potential fields. A likely mechanism responsible for converting this magnetic energy into kinetic and gravitational potential energy is magnetic reconnection. Several models for the launching mechanism of CMEs have been developed, involving different kinds of instabilities, magnetic reconnection processes, shearing motions, catastrophic flux cancellations, and mass unloading. An overview of these different mechanisms can be found in Chen (2011). These models are similar in the sense that they all involve the conversion of large amounts of magnetic energy into kinetic energy in a relatively short timespan. However, none of these mechanisms is able to reproduce all the observed properties of CMEs, and it is thus fair to say that the exact launch mechanism remains unknown. In order to make progress, it is essential that the configuration of the magnetic field before the eruption is well understood. Knowledge about the magnetic configuration prior to the eruption may lead to insights about the triggering mechanism of the CME.

CMEs and prominences are closely related phenomena. This is illustrated in the classical three-part CME, which has a leading edge, followed by a dark cavity, followed by a bright cloud of plasma (see panel (b) of Fig. 1.6). This bright cloud of plasma is almost certainly an erupting filament. The leading edge and the cavity of the CME are probably a consequence of the flux-rope structure of prominences. One should however note that not every CME has this three-part structure and not every CME is thus related to an erupting filament. It is possible that those CMEs still originate from a magnetic structure similar to that of a filament, with the only difference that there is no dense plasma embedded in the flux-rope. Moreover, not every prominence eruption is associated with a CME either. Apart from that, prominences can also break up or dissipate without erupting.

1.2.3.5 Solar Flares

Solar flares are fast and sudden releases of large amounts of energy, mostly in the form of fast-particle energy and radiation. The emitted radiation often covers the whole electromagnetic spectrum, from radio waves to gamma-rays. When observed on the Sun, a flare appears as a sudden flash of brightness. Like CMEs, solar flares often originate from ARs, and they are also expected to be powered by magnetic energy. In addition, CMEs are often accompanied by solar flares, although this is definitely not always the case.

An interesting feature of flares is that they are often observed in ARs with a very complicated magnetic topology. In contrast, simple bipolar active regions often show almost no flare activity (Priest 2014). It is generally believed that flares are powered through magnetic reconnection processes occurring in the solar corona (Shibata & Magara 2011). However, the exact details of the full three dimensional generation mechanism of flares are still an open question.

1.3 Observing the Solar Magnetic Field

From the previous sections it is clear that a lot of interesting solar phenomena are intrinsically magnetic in nature. Understanding these phenomena is thus tantamount to understanding the dynamics and evolution of the solar magnetic field. Therefore, it would be very helpful if one could actually observe the solar magnetic field. It turns out that this is indeed possible in some regions of the Sun, by using the Zeeman effect and by analysing the polarisation of the electromagnetic waves emitted by the Sun.

The Zeeman effect is a quantum mechanical effect that results in the splitting and polarisation of spectral lines of atoms in an external magnetic field. The possible polarisations are shown in panel (a) of Fig 1.7. σ_+ and σ_- are, respectively, the right handed and left handed circular polarizations around the external magnetic field. π is the linear polarisation parallel to the magnetic field. To illustrate the Zeeman effect, we consider a normal Zeeman triplet shown on panel (b) of Fig. 1.7. The total angular momentum quantum number J of the lower level is 0, whereas the upper level has $J = 1$. From quantum mechanics we know that this implies that the upper level contains three sublevels, having magnetic quantum number $M = -1, 0, 1$. In contrast, the $J = 0$ level has has only one sublevel ($M = 0$). Conservation of angular momentum requires that the emitted photon of the $\Delta M = -1$ transition has angular momentum $-\hbar$, and is therefore right-handed polarized (σ_-). Analogous, the emitted photon of the $\Delta M = 1$ transition has angular momentum $-\hbar$, and is therefore left-handed polarized (σ_+). Finally, the transition $\Delta M = 0$

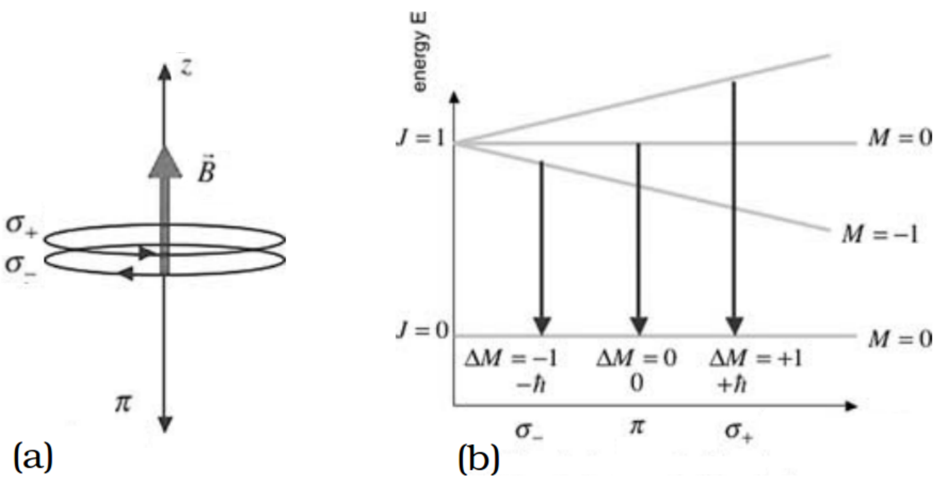

Figure 1.7: (a) Illustration of the possible polarizations: σ_+ (σ_-) is right (left) handed circular around the external magnetic field$\vec{B}$, and π is parallel to $\vec{B}$. The diagram at the right illustrates the polarization of a normal Zeeman triplet. Figure addapted from J.-P. Zahn (auth.).

emits a photon with zero angular momentum and is therefore linearly polarized (π). In addition, the different transitions emit photons at slightly different wavelengths. As a consequence, the polarization will vary along the spectral line profile.

The polarization[1] of the solar light arriving at Earth is measured in terms of the Stokes parameters I, Q, U, and V. I gives the total intensity, Q is the intensity difference between horizontal and vertical linear polarizations, U is the intensity difference between linear polarizations at $\pm 45°$, and finally, V is the intensity difference between right- and left-handed circular polarizations. The parameter V can be used to obtain the line-of-sight (LOS) component of $\mathbf{B}$. The parameters U and Q both sample the transverse magnetic component. Under some assumptions about the radiative transport of the polarized waves, it is possible to invert the Stokes profiles and thereby obtain a complete vector magnetogram (see del Toro Iniesta (2007) for details). However, there are some limitations that have to be taken into consideration.

Detecting the Zeeman effect in a coronal spectrum is very difficult for a couple of reasons. First, the high temperature of the corona broadens the line profile orders of magnitudes above the Zeeman splitting. Second, as discussed in Section 1.2.3, coronal spectral lines are optically thin. The observed line is thus the result of a complicated LOS integration, making the interpretation difficult. For example, polarity changes of the LOS component can strongly reduce the value of the measurements, unless the structure along the LOS can be detected. For these reasons, attempts to measure directly the coronal field have been relatively rare (but see e.g., Lin et al. (2004) and Kramar et al. (2006)). The photospheric environment is more favourable for using physical processes like the Zeeman effect to measure the magnetic field $\mathbf{B}$. As a consequence, most of our solar magnetic data consists of measurements of the photospheric magnetic field. From the discussion in Section 1.2.3 it should be clear that a lot of interesting magnetic phenomena take place in the corona. Therefore, the difficulties regarding the measurements of the coronal magnetic field represent a major drawback.

An additional complication is that obtaining the transverse magnetic component is in general harder than obtaining the LOS component. This can be explained as follows. The tangential component of the magnetic field goes roughly as $B_t^2 \propto \sqrt{Q^2+V^2}/I$. Therefore, the photon noise can be estimated as $B_t \delta B_t \propto \frac{Q\delta Q + U\delta U}{\sqrt{Q^2+V^2}I}$. For the minimum detectable magnetic field, i.e., $\delta B_t \sim B_t$, we have then

---

[1] Remark that the polarisations $\sigma_\pm$ and π were with respect to the external magnetic field, while the polarizations here follow the usual definitions of electromagnetic radiation.

that

$$\delta B_t \sim \frac{\sqrt{\delta Q^2 + \delta V^2}}{I B_t} \sim \frac{1}{B_t}\frac{\delta I}{I} \sim \frac{\sqrt{I}}{B_t}. \tag{1.1}$$

In contrast, the LOS component B_{LOS} can be approximated by $B_{\mathrm{LOS}} \propto V/I$, and therefore

$$\delta B_{\mathrm{LOS}} \propto \frac{\delta V}{I} \sim \frac{\delta I}{I} \sim \sqrt{I}. \tag{1.2}$$

Comparing Eq. (1.2) with Eq. (1.1), it can be seen that the noise on the transverse magnetic field can be considerably larger for weak magnetic fields. For example, the Helioseismic and Magnetic Imager (HMI) on board of SDO has estimated noise levels of about 10G and 100G for the LOS and transverse magnetic field, respectively.

Another problem concerns the spatial resolution of the observation. A limited spatial resolution leads to a loss in information about the fine structure of the magnetic field. A spatial resolution element may contain magnetic fields of different polarity. Since these magnetic features are unresolved, opposite magnetic polarities will partially cancel each other out. In the most dramatic case, the positive magnetic flux of the resolution element will exactly equal the negative magnetic flux, such that V equals zero. As a consequence, the LOS magnetic component will be wrongly put equal to zero.

A final problem with the inversion of the Stokes parameters to obtain $\mathbf{B}$, concerns the direction of the longitudinal magnetic component. The symmetry of the linear polarisation parameters Q and U causes a 180° ambiguity in the direction of the transverse magnetic component. Numerous methods have been invented to remove this ambiguity. Although some of these methods show good results, none of them removes the ambiguity everywhere perfectly. An overview and comparison of these different methods can be found in Metcalf et al. (2006).

1.4 Motivation and Outline of Thesis

From the discussion given above, it should be clear that the solar magnetic field plays a central role in many phenomena occurring in the solar atmosphere, including transient eruptive events. Understanding these phenomena is essential towards developing a reliable space weather forecast (see also the recent COSPAR roadmap by Schrijver et al. (2015)), and is therefore the subject of intensive research. Since several important space weather events, like flares and CMEs, are powered by the solar magnetic field, it is essential to gain a deep understanding about the structure and evolution of the solar magnetic field. However, as explained in Section 1.3, it is very difficult to measure the coronal magnetic field directly. Therefore, one needs to develop good models of the coronal field. These models are often based on the photospheric magnetic field, which can be measured.

In this work, we present a study of the three-dimensional structure of the coronal magnetic field above active regions. More specifically, we will look at methods that reconstruct the coronal magnetic field under the assumption that the corona is well approximated by a *force-free magnetic field*. This is a magnetic field in which the Lorentz force is essentially zero. Chapter 2 elaborates on the mathematical theory of force-free magnetic fields and their applicability for modelling the coronal magnetic field. Within this mathematical framework, several methods for reconstructing the coronal magnetic field are discussed. These methods try to obtain the coronal magnetic field by extrapolating photospheric magnetogram data. One of these methods does this by means of an optimization approach. In Chapter 3, a numerical implementation of the optimization method is discussed. Using semi-analytical solar active region models, the performance of the method is qualitatively and quantitatively evaluated. In chapter 4, we use the optimization method to study the evolution of a solar active region during a period of seven days. In Chapter 5, the main results of this thesis are summarised.

Chapter 2

Force-Free Fields

Numerous interesting phenomena, like filaments, CMEs and flares, occur in the solar corona. Since these phenomena are magnetic in nature, understanding them requires knowledge of the coronal magnetic field. However, as explained in Section 1.3, direct measurements of the coronal magnetic field are difficult and only available for a few individual cases. The magnetic measurements that are feasible provide instead the photospheric magnetic field. To obtain the coronal magnetic field, it is therefore necessary to develop methods that extrapolate the coronal magnetic field from the photospheric magnetograms. This is only possible if one has a good mathematical model for the coronal magnetic field.

In this chapter we will elaborate on a popular model for the coronal magnetic field, called the *force-free field assumption*. Section 2.1 details how the equations that govern force-free fields can be obtained, and why force-free fields are interesting for modelling the coronal magnetic field. Moreover, we will see that force-free magnetic fields can be divided into three groups of increasing complexity: potential fields, linear force-free fields, and nonlinear force-free fields. These three types of magnetic field, and there applicability to model the coronal field are discussed in Section 2.2, 2.3, and 2.4, respectively. Since the equations governing force-free fields are differential equations, they need to be supplied with appropriate boundary conditions. As it turns out, this is far from trivial for the coronal setting and is discussed in Section 2.5.

2.1 Force-Free Field Equations

The road towards finding a good model of the coronal magnetic field, starts by gaining knowledge about the features of the coronal plasma that influence the magnetic field. The natural way to do this is by studying the different terms in the equation of motion of the coronal plasma in the single-fluid ideal magnetohydrodynamics (MHD) setting. This equation is given by

$$\begin{aligned} \rho\frac{d\mathbf{v}}{dt} &= -\nabla p + \mathbf{j}\times\mathbf{B} + \rho\mathbf{g}, && (2.1)\\ &= -\nabla p + \frac{1}{\mu_0}(\nabla\times\mathbf{B})\times\mathbf{B} + \rho\mathbf{g} && (2.2) \end{aligned}$$

where $\mathbf{v}$ denotes the velocity, ρ the density, p the thermal pressure, $\mathbf{g}$ the gravitational acceleration, μ_0 the permeability of free space, $\mathbf{j}$ the current density, and $\mathbf{B}$ the magnetic field. The second equality is obtained by using Ampère's law. In addition to Eq. (2.2), the solenoidal condition for the magnetic field, i.e., $\nabla\cdot\mathbf{B} = 0$, has to be taken into account. Furthermore, one also needs an appropriate equation of state. Most equations of state, like the ideal gas law, show a temperature dependence which in turn requires an additional energy equation. In general, the resulting system of equations cannot be solved analytically and a numerical approach is required. To solve these equations, one has to impose an appropriate set of boundary conditions for the different physical variables. Since the magnetic field of the photosphere can be measured, it is natural to consider the photosphere as a boundary of the computational domain. However, the photospheric density and temperature are very hard to measure. In addition, when using the photosphere as boundary, one needs to include the transition region, and thereby a description of the coronal heating, which further increases the difficulties. As a consequence, the equations are often simplified by making additional assumptions. This is justified as long as one understands the limitations of the approximations.

A first popular assumption is to consider a static plasma configuration. This assumption can be justified as follows. Using a characteristic length scale L_0, a typical density ρ_0 and pressure p_0, a time scale t_0, and a magnetic field strength B_0, we can make the following estimations:

$$\rho\frac{d\mathbf{v}}{dt} \sim \rho_0\frac{L_0}{t_0^2}, \quad \nabla p \sim \frac{p_0}{L_0}, \quad \frac{1}{\mu_0}(\nabla\times\mathbf{B})\times\mathbf{B} \sim \frac{B_0^2}{\mu_0 L_0}, \quad \rho\mathbf{g} \sim \rho_0 g. \tag{2.3}$$

Using these estimates in Eq. (2.2), we obtain that the inertia term in the left-hand side can be neglected if the flow speed is much smaller than the sound speed $v_s \sim \sqrt{p_0/\rho_0}$, the Alfvén speed $v_A = B_0/\sqrt{\mu_0\rho_0}$, and the gravitational free fall speed $v_{\rm ff} \sim \sqrt{gL_0}$. If these conditions are fulfilled, one obtains the following equation for magnetohydrostatic balance

$$\mathbf{0} = -\nabla p + \mathbf{j}\times\mathbf{B} + \rho\mathbf{g}. \tag{2.4}$$

In the corona, values for the sound speed and the free fall speed are about $\sim$ 150 km/s, and the Alfvén speed is on average about $\sim$ 6000 km/s, although its value may strongly vary depending on the local plasma properties. A static configuration is often a good first approximation, as long as one stays away from regions where the magnetic field is evolving very rapidly, e.g., in current sheets. Evidently, a static approach cannot be used to model CMEs or flares, yet it can be used to study the magnetic field before and after such eruptive events. A comparison of the prior and anterior magnetic field properties can then be used to gain knowledge about the actual eruptive event. For example, by comparing the energy stored in the magnetic field before and after the eruption, an estimate about the energy content of the eruptive event is obtained. Moreover, by studying the magnetic topology before the eruption, one can hope to gain insight in which magnetic topologies are able to launch eruptions.

For the solar corona, Eq. (2.4) can be further simplified by realizing that often not all the terms are of equal importance. The gravity force can be neglected in comparison with the pressure gradient when the length scale L_0 is much less than the pressure scale-height Λ[1]. In addition, in a large part of the corona, the pressure force can be neglected in comparison with the Lorentz force $\mathbf{j}\times\mathbf{B}$. This is a consequence of the relatively strong coronal magnetic field and the low plasma density. It is often expressed by stating that $\beta = 2\mu_0 p/B^2$ (i.e., the ratio between the gas pressure and magnetic pressure), is much smaller than one. For solar active regions, $\beta \ll 1$ is valid in most of the low and mid corona (see e.g., Gary 2001). However, at small heights above the photosphere and in the upper part of the corona, β often exceeds unity. In addition, coronal regions may contain extended structures, like helmet streamers, where β is also not small.

In the regions where $\beta \ll 1$ is satisfied, the pressure and gravity terms in Eq. (2.4) can be neglected, leading to the following equation:

$$\mathbf{j}\times\mathbf{B} = 0. \tag{2.5}$$

---

[1] The pressure scale height is defined as $\Lambda = RT/\tilde{\mu}g$, with T the temperature, R the gas constant, and $\tilde{\mu}$ the mean molecular weight. It gives the distance over which the pressure decreases with a factor e and can be found by solving $dp/dz = -\rho(z)g$, (see, e.g., Priest 2014).

A magnetic field that satisfies this equation is called a *force-free field*. For such fields, any electrical current has to be aligned with the magnetic field, i.e., currents only flow along the magnetic field lines. Mathematically, this can be expressed as

$$\mu_0 \mathbf{j} = \alpha \mathbf{B}, \tag{2.6}$$

where the force-free parameter α gives the proportionality between the magnetic field and the current density. Inserting this in Ampère's law then gives

$$\nabla \times \mathbf{B} = \alpha \mathbf{B}. \tag{2.7}$$

In general, the force-free parameter α is a space-dependent function. The only restriction on α can be found by taking the divergence of Eq. (2.7), and using the solenoidal condition $\nabla \cdot \mathbf{B} = 0$. In doing so, one obtains that

$$\mathbf{B} \cdot \nabla \alpha = 0, \tag{2.8}$$

implying that α is constant along magnetic field lines. Remark that the spatial dependence of α allows different field lines to have a different value of α. The function α identifies thus the amount of current that flows along each magnetic field line.

Together, Eq. (2.7) and Eq. (2.8) constitute a set of four differential equations for the three magnetic field components and the force-free parameter α. It is thus a complete set of differential equations. Despite looking simple, solving Eqs. (2.7) and (2.8) is far from trivial. The complexity of the problem follows from the $\alpha\mathbf{B}$ term in Eq (2.7), making it a nonlinear differential equation.

One way to proceed in solving the force-free equations is by imposing extra conditions on the spatial behaviour of α. A widely used approximation is to assume that α is constant. Within this approximation, the case $\alpha = 0$ is often considered separately. These approximations will be discussed in Sections 2.2 and 2.3. However, whereas the approximations to obtain the force-free equations are fairly well justified in the corona, it turns out that a constant α assumption is rarely a good approximation of the coronal magnetic field. Therefore, it is necessary to solve the force-free equations in general. This will be discussed in Section 2.4.

Solving the force-free equations requires the addition of boundary conditions that are compatible with a force-free magnetic field. To reconstruct the coronal magnetic field, these boundary conditions can be deduced from magnetograms. However, as explained in Section 1.3, we mostly measure the photospheric magnetic field, where force-freeness is often a poor approximation. Therefore, methods have been developed to make magnetograms more force-free. These methods, together with the boundary conditions, will be discussed in Section 2.5.

2.2 Potential Magnetic Field

The simplest way to obtain a solution satisfying Eqs. (2.7) and (2.8), is by assuming that $\alpha = 0$ everywhere. Since $\mathbf{j} = \alpha\mathbf{B}$, there are no electric currents present in this solution. This means that $\nabla \times \mathbf{B} = 0$, such that the magnetic field has a scalar potential ϕ

$$\mathbf{B} = -\nabla \phi, \tag{2.9}$$

clarifying why $\mathbf{B}$ is in this case called a potential magnetic field. The solenoidal condition implies that ϕ satisfies the Laplace equation $\nabla^2 \phi = 0$. This is a well-known differential equation which can be solved as a well posed boundary value problem (see Jackson 1975). The boundary conditions can be either the value of ϕ on the boundary or its derivative normal to the boundary: $\hat{\boldsymbol{n}} \cdot \nabla \phi$. The former is called the Dirichlet boundary condition, whereas the latter is called the Neumann boundary condition.

There exist several reasons why potential fields are of interest to solar physics, including the following

- Potential fields can be easily computed and provide a first estimate of the magnetic field strength and topology.
- As boundary condition, only the normal magnetic field component B_n at the photosphere is needed to compute the potential field.
- Potential fields can be used to estimate the shapes of coronal magnetic loops.
- Potential fields correspond to the lowest energy configuration (see Section 2.2.1).
- Potential fields are used in several nonlinear force-free extrapolation methods (see Section 2.4.2).

2.2.1 Potential Minimum-Energy Theorem

One of the most interesting features of potential magnetic fields is that they correspond lowest possible energy states in which magnetic fields can reside. More precisely, given a domain Ω with the normal component B_n fixed on the boundary $\partial\Omega$, the potential field will be the field with the smallest amount of energy

$$E_{\text{mag}} = \int_\Omega \frac{B^2}{2\mu_0} dV.$$

This means thus that all other magnetic fields, with the same B_n on the boundary of the volume, will have higher energy. The volume can be a semi-infinite region such as the solar corona, as long as there are no sources at infinity.

The proof of this theorem goes as follows. Let $\nabla\phi$ be a potential field and $\mathbf{B}$ any other magnetic field, such that both fields have the same normal component on $\partial\Omega$. We can write $\mathbf{B} = \nabla\phi + \tilde{\mathbf{B}}$, with $\tilde{\mathbf{B}} = \mathbf{B} - \nabla\phi$. Remark that $\tilde{\mathbf{B}} \cdot \hat{\boldsymbol{n}} = 0$ on $\partial\Omega$ since $\mathbf{B}$ and $\nabla\phi$ have the same normal component on $\partial\Omega$.

The magnetic energy of $\mathbf{B}$ can be calculated as

$$\begin{aligned}
E_{\text{mag}} &= \int_\Omega \frac{(\nabla\phi + \tilde{\mathbf{B}})^2}{2\mu_0} dV \\
&= \int_\Omega \frac{(\nabla\phi)^2 + 2\nabla\phi \cdot \tilde{\mathbf{B}} + \tilde{B}^2}{2\mu_0} dV \\
&= \int_\Omega \frac{(\nabla\phi)^2 + 2\nabla \cdot (\phi\tilde{\mathbf{B}}) + \tilde{B}^2}{2\mu_0} dV,
\end{aligned}$$

where the last equality was obtained by using the solenoidal condition for $\tilde{\mathbf{B}}$. The middle term can be rewritten using Gauss's theorem

$$\begin{aligned}
E_{\text{mag}} &= \int_\Omega \frac{(\nabla\phi)^2 + \tilde{B}^2}{2\mu_0} dV + \frac{1}{\mu_0} \int_{\partial\Omega} \phi\tilde{\mathbf{B}} \cdot \hat{\boldsymbol{n}} dA \qquad (2.10) \\
&= \int_\Omega \frac{(\nabla\phi)^2 + \tilde{B}^2}{2\mu_0} dV, \qquad (2.11)
\end{aligned}$$

where we used that $\tilde{\mathbf{B}} \cdot \hat{\boldsymbol{n}} = 0$ on $\partial\Omega$. Since $\tilde{B}^2 \geq 0$, it follows that the energy stored in $\mathbf{B}$ exceeds the energy stored in the potential field. The excess energy of $\mathbf{B}$ compared to the energy of the potential field

$\nabla\phi$ is called the *magnetic free energy* ΔE_{mag}. We have thus that

$$\Delta E_{\mathrm{mag}} = E_{\mathrm{mag}} - \int \frac{(\nabla\phi)^2}{2\mu_0} dV = \int \frac{\tilde{B}^2}{2\mu_0} dV \geq 0. \tag{2.12}$$

ΔE_{mag} is called *free* energy since it is the maximal amount of magnetic energy that can be released by a magnetic field. The fact that potential fields satisfy $\Delta E_{\mathrm{mag}} = 0$ implies that they are unable to drive solar eruptions. This is because the magnetic field before the eruption should have a higher energy state than after the eruption. If not, an eruption would have to bring extra energy into the magnetic field, which is unrealistic. In contrast, a magnetic field can evolve to a more potential state by releasing magnetic energy through a solar eruption.

2.2.2 Calculation Methods

This section presents a brief review of two important methods for solving the Laplace equation. When modelling the coronal magnetic field, one often represents the corona by the semi-infinite half-space $\Omega = \{z > 0\}$, with the z-axis pointing towards the observer. The boundary $\partial\Omega = \{z = 0\}$ corresponds then with the photosphere, where magnetic measurements provide the value of B_n. Hence the Neumann boundary condition is applicable on $\partial\Omega$:

$$\hat{\boldsymbol{n}} \cdot \nabla\phi = -B_n. \tag{2.13}$$

As a second boundary condition one assumes that the field strength decays to zero at infinity

$$\lim_{z \to \infty} \phi(\mathbf{r}) = 0. \tag{2.14}$$

Remark that measurements of the solar magnetic field are often limited to a small patch on the solar surface. However, to solve the Laplace equation in the half space $z > 0$, one has to provide boundary conditions on the whole $z = 0$ plane. This can be done by either assuming that $B_n = 0$ everywhere outside the finite domain, or by extending the magnetic data periodically onto the whole half-space. The former is chosen when the Laplace equation is solved with a Green's function method, whereas the latter is preferred when using a Fourier expansion method (see below).

2.2.2.1 Green's Function Method

The Green's function method is extensively discussed in Sakurai (1982). It gives the potential ϕ as

$$\phi(\mathbf{r}) = \int_{z=0} B_n(\mathbf{r}') G_n(\mathbf{r}, \mathbf{r}') dA', \tag{2.15}$$

where $dA = dxdy$ and $\mathbf{r}' = (x', y', 0)$ is a point in the $z = 0$ plane. The Green's function $G_n(\mathbf{r}, \mathbf{r}')$is given by a monopole located at $\mathbf{r}'$, i.e.,

$$G_n(\mathbf{r}, \mathbf{r}') = \frac{1}{2\pi|\mathbf{r} - \mathbf{r}'|}. \tag{2.16}$$

Eq. (2.15) gives thus the potential ϕ as an integral over a series of monopoles covering the $z = 0$ plane. Since a monopole has a magnetic flux $B_n dxdy$, it is easy to see that ϕ as given by Eq. (2.15) satisfies the Neumann boundary conditions.

In practice, solar observations only provide B_n on discrete mesh points. Therefore, the integral in Eq. (2.15) has to be transformed into a sum over the grid points:

$$\phi(\mathbf{r}) = \sum_{\mathbf{r}'_{\mathbf{ij}}} B_n(\mathbf{r}'_{\mathbf{ij}}) G_n(\mathbf{r}, \mathbf{r}'_{\mathbf{ij}}) \Delta^2, \tag{2.17}$$

where $\mathbf{r}'_{\mathbf{ij}}$ gives the positions of the grid points and Δ the distance between two adjacent grid points. The discreteness of the data also requires a modified Green's function, such that ϕ still fulfils the boundary conditions approximately. The simplest solution is a monopole located at a depth $\Delta/\sqrt{2\pi}$ under the $z = 0$ plane(Sakurai 1982):

$$G_n(\mathbf{r}, \mathbf{r}'_{\mathbf{ij}}) = \frac{1}{2\pi|\mathbf{r} - \mathbf{r}'_{\mathbf{ij}} + (\boldsymbol{\Delta}/\sqrt{\mathbf{2}\boldsymbol{\pi}})\hat{\boldsymbol{n}}|}. \tag{2.18}$$

The Green's function method described above was first used in Schmidt (1964), and is therefore called the *classical Schmidt method*. However, remark that this method can only be used for regions that are close to the centre of the solar disk, since the method requires that the line-of-sight (LOS) is perpendicular to the boundary. The method can however be generalized such that the magnetic field of regions located far from the solar centre can also be reconstructed. This method is called the *oblique Schmidt method*, and was first derived in Chapter 4 of Semel (1967). In the oblique Schmidt method, the Neuman boundary condition (2.13) is changed to

$$-\hat{\boldsymbol{l}} \cdot \nabla\phi = -B_l,$$

where $\hat{\boldsymbol{l}}$ is a unit vector along the LOS, and B_l is the magnetic field along the LOS. The magnetic potential is given by (Sakurai 1982):

$$\phi(\mathbf{r}) = \int_{z=0} B_n(\mathbf{r}') G_n(\mathbf{r}, \mathbf{r}') dA', \tag{2.19}$$

with

$$G_l(\mathbf{r}, \mathbf{r}') = \frac{1}{2\pi}\left(\frac{\hat{\boldsymbol{n}} \cdot \hat{\boldsymbol{l}}}{|\mathbf{r} - \mathbf{r}'|} + \frac{\mu \cdot (\mathbf{r} - \mathbf{r}')}{|\mathbf{r} - \mathbf{r}'|(|\mathbf{r} - \mathbf{r}'| + \hat{\boldsymbol{l}} \cdot (\mathbf{r} - \mathbf{r}'))}\right), \tag{2.20}$$

and $\mu = \hat{\boldsymbol{l}} \times (\hat{\boldsymbol{n}} \times \hat{\boldsymbol{l}})$. Remark that if $\hat{\boldsymbol{l}} = \hat{\boldsymbol{n}}$, the classical Schmidt method is recovered.

The classical and oblique Schmidt method are only valid when relatively small areas on the solar surface are studied. If large regions are studied, the curvature of the solar surface has to be taken into account. The *spherical Schmidt method*, as described in Sakurai (1982), uses a Green's function method to obtain a solution. Alternatively, one can use methods that use the expansion of the solution into spherical harmonics (see below).

2.2.2.2 Expansion Method

Another way to solve the Laplace equation with boundary conditions (2.13) and (2.14), is by using the method of separation of variables (Teuber et al. 1977). In doing so, it is found that ϕ equals

$$\sum_{\mathbf{k}} \phi_{\mathbf{k}} \exp(ik_x x + ik_y y - kz), \tag{2.21}$$

where $k^2 = k_x^2 + k_y^2$ and k_x, k_y, $k > 0$ are real. The terms $\phi_{\mathbf{k}}$ can be found by expanding the boundary value B_n in its Fourier components:

$$B_n = B_{n0} + \sum_{\mathbf{k}\neq 0} B_{\mathbf{k}} \exp(ik_x x + ik_y y),$$

where B_{n0} is a constant. From Eq. (2.13), it then follows that $\phi_{\mathbf{k}} = B_{\mathbf{k}}/k$.

When the curvature of the solar surface is taken into account, it is convenient to expand ϕ in spherical harmonics (Altschuler & Newkirk 1969):

$$\phi(r,\theta,\varphi) = R_\odot \sum_{l=1}^{N} \sum_{m=0}^{l} f_l(r) P_l^m(\theta)(g_l^m \cos m\varphi + h_l^m \sin m\varphi), \tag{2.22}$$

with (r,θ,φ) the usual spherical coordinates and $P_l^m(\theta)$ the Legendre polynomials. The function $f_l(r)$ gives the radial dependence of ϕ and is given by

$$f_l(r) = \frac{(r_w/r)^{l+1} - (r/r_w)^l}{(r_w/R_\odot)^{l+1} - (R_\odot/r_w)^l}, \tag{2.23}$$

where r_w is the location of the so-called *source surface*. These potential fields are commonly called *potential field source surface* (PFSS) models of the coronal magnetic field. Remark that if $r = r_w$, then $f_l(r) = 0$, meaning that the magnetic field lines become radial at $r = r_w$. This simulates the effect of the solar wind which distort the magnetic field in the outer corona. The solar wind drags out the magnetic field lines, making them approximately radial at a distance of typically $2.5R_\odot$. Remark that in the limit of $r_w \to \infty$, one obtains the potential field that approaches zero at infinity.

Equations (2.21) and (2.22) illustrate that the expansion method involves the evaluation of an infinite series. In practical applications this is not possible and hence the series has to be truncated at a certain point.

The solution to Laplace's equation with given boundary conditions like equations (2.13) or (2.14), is uniquely determined (see, e.g., Jackson 1975). Therefore, the potential fields obtained with the Green's function method and the expansion method have to be identical. However, as discussed above, numerical codes can only use the Green's function method if integral (2.15) is replaced by a finite summation. Similar, numerical codes have to truncate the infinite series (2.22) after a finite amount of terms. Therefore, numerical codes will produce slightly different magnetic fields, depending on the used method.

2.2.3 Applicability of Potential Fields in the Solar Corona

The relative straightforward implementation of numerical codes calculating the potential field has resulted in numerous applications. Apart from computational tractability, potential fields are also popular since they only require knowledge of the radial magnetic field component. When calculating a global potential field, this radial magnetic component is obtained from Carrington maps of the photospheric magnetic field. These maps consist of an assembly of magnetograms measured over an entire solar rotation. A major drawback of this method is that it assumes that there are no temporal variations within a single solar rotation.

The applicability of a potential field model in the corona depends strongly on the properties of the region of interest. A potential field requires a region that has a magnetic field with low helicity, and the underlying magnetic sources must have remained stationary for a certain amount of time, allowing the field to reach its minimum energy state. Active regions that show flux emergence and contain highly sheared or twisted magnetic fields are therefore poorly approximated by potential fields. This is for example illustrated in Sandman et al. (2009), where the magnetic loops reconstructed with STEREO data clearly deviated from the calculated potential field. Furthermore, in Schrijver et al. (2005) it was shown that active regions have a non-potential magnetic topology, especially when magnetic flux has recently emerged in or close to the active region. Finally, as discussed in Section 2.2.1, the minimum energy of potential fields makes them unable to drive solar eruptions.

Despite these clear limitations, the potential field remains of great interest for solar physics. The reason is that PFSS fields show a good agreement with observations on large scales. In other words, large coronal loops are generally seen to coincide rather well with those predicted from PFSS. Also, PFSS gives rather good approximations for locations of coronal holes and their sizes. Actually, the PFSS model works surprisingly well considering the approximations involved. This can be understood by performing a multipole expansion of the magnetic field, which shows that the current-dependent terms decay faster than the potential terms. This implies that at large distances from the sun, the magnetic field should become increasingly potential.

In addition, potential fields can be used as a starting point in the construction of more realistic magnetic field configurations. For example, in Section 2.4.2, we will see that most of the nonlinear force-free extrapolation methods evolve a potential field towards a more accurate field topology.

2.3 Linear Force-Free Fields

A force-free field is called linear if the force-free parameter α is constant. Hence, the linear force-free field model allows currents to flow, making it a more realistic approach than the potential field model. The computation of a linear force-free field can be treated in a similar way as the potential field. Taking the curl of Eq. (2.7) gives, after some algebra, the following equation

$$(\nabla^2 + \alpha^2)\mathbf{B} = \mathbf{0}, \tag{2.24}$$

which is a linear differential equation, known as the vector Helmholtz equation. Similar to the Laplace equation, the Helmholz equation can be solved by providing the normal component of the magnetic field on the boundaries of the domain.

By expressing the magnetic field in terms of a toroidal scalar field T and a poloidal scalar field P, i.e., $\mathbf{B} = \nabla \times [T\hat{\boldsymbol{z}} + \nabla \times (P\hat{\boldsymbol{z}})]$ (Morse & Feshbach 1953), the vector Helmholtz equation can be transformed into a scalar Helmholtz equation for P:

$$(\nabla^2 + \alpha^2)P = 0. \tag{2.25}$$

Since Eq. (2.7) implies that $T = \alpha P$, solving Eq. (2.25) is sufficient to obtain the magnetic field. Similar to Laplace's equation, a solution of the scalar Helmholtz equation can be found using either a Green's function (see, e.g., Chiu & Hilton 1977; Seehafer 1978), or a series expansion method (see, e.g., Nakagawa & Raadu 1972; Altschuler & Newkirk 1969).

Several limitations of linear force-free fields can be listed:

1. A linear force-free magnetic field behaves as a spherical wave at infinity. This means that the field decays slowly, as $\exp(\pm i\alpha)/r$, such that the magnetic energy integral diverges (Seehafer 1978).
2. Related to the previous remark is the observation that currents in linear force-free fields have an infinite extent, which is unrealistic.
3. Solutions of Eq. (2.25) show oscillatory behaviour at large distance, such that there are no appropriate boundary conditions at infinity.
4. A model in which the magnetic field becomes radial at a certain source surface, like the potential field in Eqs. (2.22) and (2.23), is not possible for a force-free field. The reason is that the boundary conditions $B_\theta = B_\varphi = 0$ and $B_r \neq 0$ can only be satisfied if $\alpha = 0$ or if α is allowed to vary in space (Aly & Seehafer 1993).

5. A solution of Eq. (2.25) for given boundary conditions is not necessarily unique. In general, this is because the equation
$$(\nabla^2 + \lambda^2)P = 0, \quad B_n = 0 \text{ at } z = 0,$$
has an infinite number of eigenfunctions corresponding to eigenvalues $\lambda = \lambda_0, \lambda_1, \lambda_2, \ldots$. Therefore, if α coincides with one of these λ's, one can add the corresponding eigenfunction, scaled by an arbitrary constant. One way to ensure a unique solution is by choosing α smaller than the smallest eigenvalue λ_i.

6. Observations of the solar magnetic field have illustrated that coronal fields often contain twisted magnetic structures, indicating that both the magnitude and sign of α can vary significantly, even in small regions. This was illustrated in Wiegelmann & Neukirch (2002), where α was shown to switch sign within the studied active region. This result implies that the actual magnetic fields in active regions are highly nonlinear.

Despite these limitations, linear force-free fields remain popular for modelling the coronal magnetic field. The main reason is that solving the Helmholz equation is fairly straightforward and as boundary condition only B_n is required. However, the above list of limitations makes it clear that the use of linear force-free fields is rather limited and will therefore not be discussed any further.

2.4 Nonlinear Force-Free Field

The previous discussion has made clear that both potential fields and linear force-free fields are often an inadequate representation of coronal magnetic fields. As mentioned above, observations have illustrated that the force-free parameter α can vary significantly, giving rise to strongly localized currents. Apart from these observations, the potential field and a linear force-free field are also inadequate since they possess a minimum energy and an infinite energy[2], respectively. Therefore it is necessary obtain force-free fields in which α can vary from one field line to another, allowing (strongly) localized current densities. Such a magnetic field is called a nonlinear force-free field (NLFFF).

The equations describing the force-free field, repeated here for referential convenience, are

$$\nabla \times \mathbf{B} = \alpha \mathbf{B}, \tag{2.26}$$
$$\mathbf{B} \cdot \nabla \alpha = 0. \tag{2.27}$$

To solve Eqs. (2.26) and (2.27) in a certain domain Ω, one would like to have a combination of boundary conditions such that the problem becomes a well-posed problem in Hadamard sense. Finding such a formulation is a non-trivial problem since Eq. (2.26) and Eq. (2.27) are partial differential equations of mixed elliptic and hyperbolic type. If $\mathbf{B}$ is prescribed, the equation for α is hyperbolic, such that an appropriate boundary condition is to give α at only one polarity [3]. On the other hand, if α is given, the equation for $\mathbf{B}$ becomes elliptic, such that it is natural to provide the normal component B_n on $\partial\Omega$. Bineau (1972) and Boulmezaoud & Amari (2000) showed that these boundary conditions for α and $\mathbf{B}$ can be used to prove an existence and uniqueness theorem for Eq. (2.26) and Eq. (2.27) in a bounded domain Ω_b, if $\alpha|_{\partial\Omega}$ remains small enough. To the best of my knowledge, a general existence and uniqueness theorem valid for all values of α has not yet been proven, neither in a bounded nor in an unbounded domain.

---

[2] Remark that a linear force-free field has only an infinite energy when considering a (semi-)infinite domain, but not for a finite volume.

[3] α is only required at one polarity because it is constant along magnetic field lines. Therefore the values of α of one polarity are mapped to the other polarity by following the magnetic field lines.

The complexity of Eqs. (2.26) and (2.27) makes finding analytical solutions very hard. Semi-analytical solutions can only be obtained by making certain symmetry assumptions, such that the magnetic field becomes independent of at least one of the coordinates. Two such solutions will be discussed below. The importance of these solutions resides in their applicability as test cases to validate numerical extrapolation codes. Such numerical schemes try solve the force-free equations by extrapolating the coronal magnetic field from photospheric vector magnetograms. Various extrapolation methods have been developed and they are discussed in Section 2.4.2. We remark that if these extrapolation methods are not able to reproduce smooth analytical solutions, then there is little hope that they perform well with real solar data. Moreover, the obtained analytical solutions are also valuable since the nonlinearity of the problem does not allow the superposition of solutions to obtain new ones.

2.4.1 Semi-Analytical Solutions

2.4.1.1 The Low and Lou Equilibrium

In this section, we will describe a class of semi-analytical nonlinear force-free fields, found by Low & Lou (1990) (henceforth LL). As shown in the following, these solutions can be used as a model of the magnetic field of a solar active region. To obtain the LL equilibrium, one solves equations (2.26) and (2.27) in infinite space, under the assumptions that the magnetic field is axisymmetric. This means that it can be expressed in terms of two scalars functions A and Q. In spherical coordinates this becomes

$$\mathbf{B} = \frac{1}{r\sin\theta}\left(\frac{1}{r}\frac{\partial A}{\partial\theta}\hat{\boldsymbol{r}} - \frac{\partial A}{\partial r}\hat{\boldsymbol{\theta}} + Q\hat{\boldsymbol{\varphi}}\right), \tag{2.28}$$

where A is called the *flux function*, since $A =$ constant represents a flux surface. Using the force-free equations, it can be shown that Q is a function of A, that $\alpha = \frac{dQ}{dA}$, and that A satisfies the Grad-Shafranov equation (see e.g., Marsh 1992)

$$\frac{\partial^2 A}{\partial r^2} + \frac{1-\mu^2}{r^2}\frac{\partial^2 A}{\partial \mu^2} + Q\frac{dQ}{dA} = 0, \tag{2.29}$$

where $\mu = \cos\theta$. This equation can be solved by seeking solutions of the form:

$$Q(A) = aA^{1+1/n} \tag{2.30}$$

$$A = \frac{P(\mu)}{r^n}, \tag{2.31}$$

where a and n are constants, and P is a scalar function of μ. Remark that $a = 0$ corresponds to a potential field, i.e., $\alpha = 0$. By substituting Eqs. (2.31) and (2.30) into Eq. (2.29), the following ordinary differential equation for P is obtained:

$$(1-\mu^2)\frac{d^2P}{d\mu^2} + n(n+1)P + a^2\frac{1+n}{n}P^{1+2/n} = 0. \tag{2.32}$$

One way to solve this equation is by fixing a value for n, and solving (2.32) as an eigenvalue problem, with a^2 the corresponding eigenvalue. To ensure that the solutions are well behaved, one has to require that B_φ and B_θ vanish along the symmetry axis. This can be done by requiring that $P = 0$ at $\mu = \pm 1$. The origin remains a singularity [4] and can be viewed as the location of a magnetic point source

---

[4] The existence of such a singularity is intrinsic to nonlinear force-free fields with finite energy in infinite space. For such a field, the magnetic energy E_{mag} can be written as $E_{\text{mag}} = \int_\Omega \frac{\mathbf{r}\cdot\mathbf{j}\times\mathbf{B}}{\mu_0} dV$. If the force-free field has no singularity, one obtains thus that $E_{\text{mag}} = 0$ and hence $\mathbf{B} = 0$.

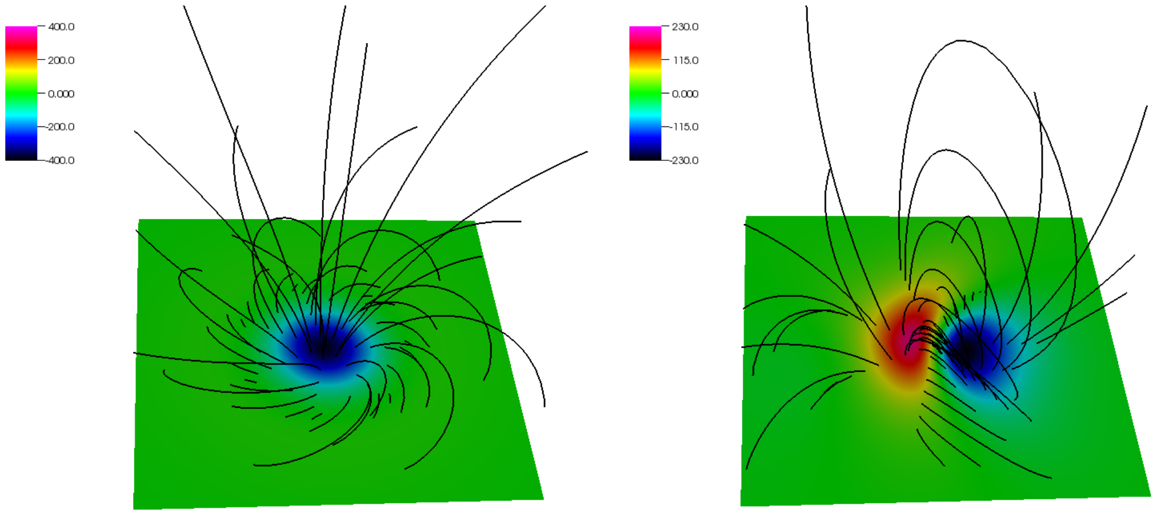

Figure 2.1: LL equilibriua for parameters $n = 1$, $a^2 = 0.425$, and $\ell = 0.3$. The left panel corresponds to a LL equilibrium with $\Phi = 0$. The right panel corresponds to a LL equilibrium with $\Phi = \pi/3$. The colour-coding corresponds to the vertical magnetic field B_z (in G). The black lines are a number of arbitrary selected magnetic field lines.

To mimic the solar magnetic field in an active region, the point source is translated over a distance L away from the origin, while keeping it outside the computational domain. In addition, the symmetry axis is rotated over a certain angle Φ with respect to the vertical axis. This means that the Cartesian coordinates used to describe the LL equilibrium, i.e., $X = r \sin\theta \cos\varphi$, $Y = r \sin\theta \sin\varphi$, and $Z = r\cos\theta$, can be written in term of the physical Cartesian coordinates as

$$\begin{aligned} X &= x\cos\Phi - (z + L)\sin\Phi, && (2.33)\\ Y &= y, && (2.34)\\ Z &= x\sin\Phi + (z + L)\cos\Phi. && (2.35) \end{aligned}$$

The distance L is often expressed in units of a typical length scale r_0, i.e., $L = \ell r_0$. The obtained magnetic field configuration shows resemblance with a realistic magnetic field of a solar active region. The translation of the point source and the rotation of the symmetry axis are done in order to obtain a solution that is not symmetric in the considered domain.

Fig. 2.1 shows two examples of LL equilibria for $n = 1$ and $a^2 = 0.425$. The magnetic point source is translated a distance $0.3r_0$ underneath the $z = 0$ plane, which represents the photosphere. On the left plot, $\Phi = 0$, which means that the symmetry axis of the LL equilibrium is aligned with the vertical axis. On the right plot, the symmetry axis of the LL equilibrium was rotated over an angle $\Phi = \pi/3$. In this plot, the symmetry is no longer obvious and a magnetic field configuration somewhat similar to a solar active region is obtained.

Analogously, if the photosphere is represented by (part of) a spherical shell with radius $r = R_\odot$, the point source is shifted a distance L away from to origin, while keeping it outside the computational domain. Such a configuration is shown in Fig. 2.2.

By changing the parameters n and Φ, a whole class of different magnetic configurations is obtained. These magnetic fields are often used for testing numerical methods that extrapolate a nonlinear force-free field from photospheric boundary conditions. By prescribing the magnetic field at the boundary of the computational box, the extrapolation tool should be able to reproduce the LL equilibrium.

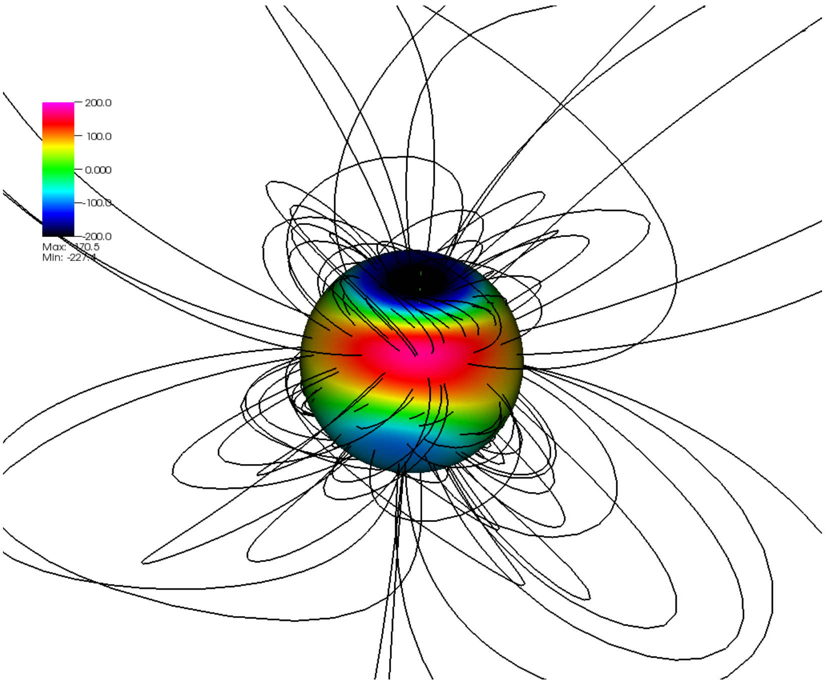

Figure 2.2: LL equilibrium in spherical coordinates for parameters $n = 1$, $a^2 = 0.425$, $\ell = 0.3$ and $\Phi = \pi/3$. The photosphere is represented by $\{r = R_\odot\}$ and the colour-coding corresponds to the radial magnetic field B_r (in G). The black lines are a number of arbitrary selected magnetic field lines.

2.4.1.2 The Titov-Démoulin equilibrium

In this section, we discuss a flux-rope model called the Titov-Démoulin (henceforth TD) equilibrium (Titov & Démoulin 1999). Despite that this model is only approximately force-free, it is still a popular model for testing nonlinear force-free numerical codes. The set-up of the model is illustrated in Fig. 2.3 and consists of a current-carrying toroidal flux-rope of major axis R_0 and minor axis a, and two magnetic monopoles $\pm q$. The original TD model also contained a line current I_0 flowing along the symmetry axis of the torus. The symmetry axis of the toroidal flux-rope, the line current, and the monopoles are all a distance d submerged under the solar surface ($z = 0$). In doing so, the resulting configuration in the $z > 0$ plane resembles a magnetic flux tube, line-tied to the photosphere.

Titov et al. (2014) generalized the Titov-Démoulin equilibrium by including flux-ropes that do not have a uniform axial current. Two different current density profiles are considered by the authors. The first one is a current distribution in which the current is limited to a small layer at the outer boundary of the flux-rope. This configuration is called the *hollow-core distribution*. Next, a *parabolic current distribution* is considered, in which the current distribution obtains its maximum at the centre of the flux-rope. These two configurations will be used in Chapter 3. Titov et al. (2014) determined the magnetic field in terms of a magnetic vector potential. Here we limit ourself to the description of the basic parameters and the stability of the flux-rope.

In contrast to the original TD model, the configurations developed by Titov et al. (2014) do not contain a line current flowing along the symmetry axis of the torus. The total magnetic field is then equal to the sum of the bipolar field $\mathbf{B}_q$, and the magnetic field $\mathbf{B}_\mathrm{t}$ of the flux-rope. The magnetic component produced by the magnetic charges $\pm q$ is given by

$$\mathbf{B}_q = q\left(\frac{\mathbf{r}_+}{|\mathbf{r}_+|^3} + \frac{\mathbf{r}_-}{|\mathbf{r}_-|^3}\right), \tag{2.36}$$

with $r = (x \mp L, y, z - L)$. Remark that the use of magnetic monopoles does not violate the solenoidal condition, since the magnetic monopoles are located outside the domain. This overlaying potential field exercises a force on the toroidal current in the magnetic flux tube. This is necessary to keep the flux-rope down, since the outward hoop force of the torus , i.e., the Lorentz force resulting from the curvature of the tube axis, will try to expand the flux tube (Shafranov 1963)

To proceed, it is assumed that $a \ll R_0$, which means that the flux-rope is thin compared to its global size. Assuming in addition that the plasma pressure is negligible, i.e., assuming a low β environment, the magnitude of the magnetic hoop force is given by

$$F_{\text{hoop}} = \frac{\mu_0 I^2}{4\pi R_0}\left(\ln\frac{8R_0}{a} - \frac{3}{2} + \frac{l_i}{2}\right),$$

where l_i is the total internal self-inductance per unit length of the flux-rope. This hoop force needs thus to be balanced by an opposite Lorentz force due to the ambient bipolar field. This force balance can be written as:

$$\frac{\mu_0 I^2}{4\pi R_0}\left(\ln\frac{8R_0}{a} - \frac{3}{2} + \frac{l_i}{2}\right) + IB_\perp = 0, \tag{2.37}$$

where $B_\perp$ denotes the component of the ambient bipolar field orthogonal to the torus-plane, i.e.,

$$B_\perp = -\frac{2qL}{\left(R_0^2 + L^2\right)^{3/2}}\hat{\mathbf{x}}.$$

Solving this equation for the current I yields the so-called *Shafranov's equilibrium current*

$$I_{\text{S}} = -\frac{4\pi R B_\perp/\mu_0}{\ln\left(\frac{8R}{a}\right) - \frac{3}{2} + \frac{l_i}{2}} \tag{2.38}$$

$$= \frac{8\pi L R_0 (R_0^2 + L^2)^{-3/2}}{\mu_0\left[\ln\left(\frac{8R}{a}\right) - \frac{3}{2} + \frac{l_i}{2}\right]}. \tag{2.39}$$

If $I > I_{\text{S}}$, the outward hoop force will be larger than the inward force due to the overlaying bipolar field, and hence the flux-rope will expand. This may lead to an instability called the *torus instability*. In contrast, when $I < I_{\text{S}}$ the flux-rope will be pulled towards the photosphere since the hoop force is now smaller than the inward force due to the overlaying field. An expanding or shrinking flux-rope will compress the ambient magnetic field in the direction of motion. This increase in magnetic pressure will counteract the hoop force of the magnetic flux-rope. Whether this is sufficient to avoid the torus instability depends largely on the strength of the ambient field (Kliem & Török 2006). Also, magnetic reconnection at the bottom of an expanding flux-rope may complicate things, since it can slowly drive the flux-rope towards an unstable configuration. In addition, Török et al. (2004) showed that the flux-rope may be subject to the kink instability when the twist of the rope exceeds a certain value Φ_c which depends on the ratio a/R.

2.4.2 Extrapolation Methods

In practice, solar observations provide magnetograms which can be used as boundary conditions for the nonlinear force-free equations. Obtaining a solution of Eqs. (2.26) and (2.27) with such boundary data requires a numerical approach. Different numerical models, also called extrapolation models, have been developed for the computation of nonlinear force-free coronal magnetic fields. An important difference between those models is the way the boundary conditions are imposed. Some methods use the full vector magnetogram, whereas other methods use the normal magnetic field and the α-distribution of one

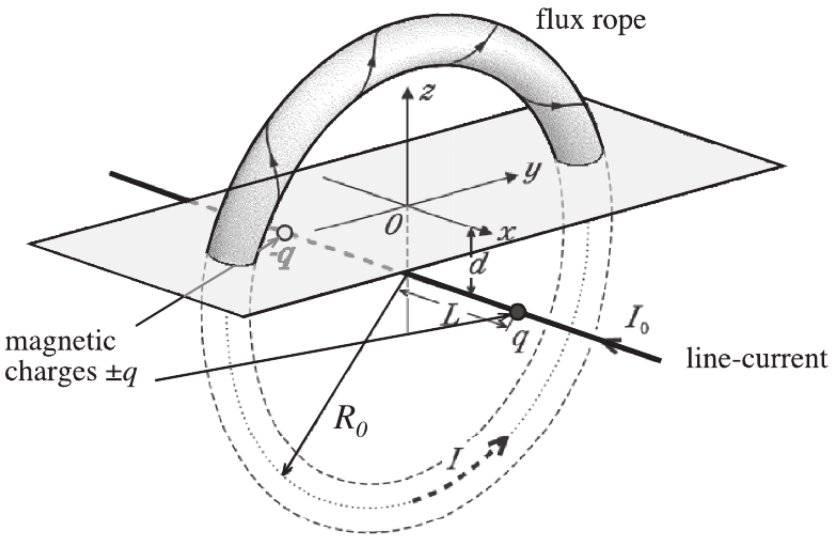

Figure 2.3: The Tidov-Démoulin model, consisting of a toroidal flux tube, a line current I_0, and two opposite magnetic monopoles $\pm q$. Figure adapted from Titov & Démoulin (1999).

polarity. As it turns out, there is a strong dependence of the solutions on the boundary conditions, as we will discuss in Section 2.5.1.

In the remainder of this section, we will introduce three important extrapolation methods: the optimization method, the magnetofrictional method, and the Grab-Rubin method. We focus on these three methods since they have shown the most promising results (see, e.g., Schrijver et al. 2006, 2008). For an extended review of these methods, we refer to Wiegelmann & Sakurai (2012).

2.4.2.1 The Optimization Method

The optimization method was originally proposed by Wheatland et al. (2000). The idea behind the method is to minimize a functional $L(\mathbf{B})$ that measures the Lorentz force and the divergence of the magnetic field in a computational volume. More specifically, this functional is defined as

$$L = L_f + L_d, \tag{2.40}$$

where

$$L_f = \int_V B^2 w_f \mathbf{\Omega}_f^2 dV, \qquad L_d = \int_V B^2 w_d \mathbf{\Omega}_d^2 dV. \tag{2.41}$$

In these equations w_f and w_d are dimensionless weighting functions and

$$\mathbf{\Omega}_f = \frac{\mathbf{j}\times\mathbf{B}}{B^2}, \qquad \mathbf{\Omega}_d = \frac{(\nabla\cdot\mathbf{B})\mathbf{B}}{\mu_0 B^2}. \tag{2.42}$$

The quantity L_f gives the Lorentz force integrated over a volume V. Similarly, L_d gives the divergence of the field $\mathbf{B}$, integrated over V. For a nonlinear force-free magnetic field both quantities should be zero, and hence L will also be zero. Moreover, choosing w_f and w_d as positive functions implies that $L \geq 0$.

To minimize the function L, a time-like iteration parameter t is introduced. Differentiating L with respect to t yields the following expression

$$\frac{1}{2}\frac{\partial L}{\partial t} = -\int_V \frac{\partial \mathbf{B}}{\partial t}\cdot\mathbf{F}_{\text{opt}} dV - \int_S \frac{\partial \mathbf{B}}{\partial t}\cdot\mathbf{G}_{\text{opt}} dS, \tag{2.43}$$

where

$$\begin{aligned}\mathbf{F}_{\mathrm{opt}} &= \frac{1}{\mu_0}\left(\boldsymbol{\Omega}_f \times \mathbf{B}\right) \times \nabla w_f + \frac{1}{\mu_0}\left(\boldsymbol{\Omega}_d \cdot \mathbf{B}\right) \nabla w_d + w_f \mathbf{F}_f + w_d \mathbf{F}_d, &(2.44)\\ \mathbf{G}_{\mathrm{opt}} &= w_f \hat{\boldsymbol{n}} \times \left(\boldsymbol{\Omega}_f \times \mathbf{B}\right) - w_d (\boldsymbol{\Omega} \cdot \mathbf{B})\hat{\boldsymbol{n}}, &(2.45)\end{aligned}$$

with

$$\begin{aligned}\mathbf{F}_f &= \frac{1}{\mu_0}\nabla \times \left(\boldsymbol{\Omega}_f \times \mathbf{B}\right) + \mathbf{j} \times \boldsymbol{\Omega}_f + \boldsymbol{\Omega}_f^2 \mathbf{B}, &(2.46)\\ \mathbf{F}_d &= -\frac{1}{\mu_0}\left(\nabla \cdot \mathbf{B}\right) \boldsymbol{\Omega}_{\mathbf{d}} + \frac{1}{\mu_0}\nabla\left(\boldsymbol{\Omega}_d \cdot \mathbf{B}\right) + \boldsymbol{\Omega}_d^2 \mathbf{B}. &(2.47)\end{aligned}$$

For the derivations of these expressions we refer to Appendix A. If $\mathbf{B}$ is kept fixed on the surface S, the surface integral in Eq. (2.43) disappears. Iterating the magnetic field by

$$\frac{\partial \mathbf{B}}{\partial t} = \mu \mathbf{F}, \tag{2.48}$$

with $\mu > 0$ an arbitrary function, results then in the following evolution for L

$$\frac{1}{2}\frac{dL}{dt} = -\int_V \mu F^2 dV. \tag{2.49}$$

From this expression it is clear that L will decrease monotonically. Moreover, remark that if the solution space is convex, the obtained magnetic field for which L is minimal is also a global minimum. In contrast, if the solution space is non-convex, the obtained magnetic field may only be a local minimum.

The minimization procedure is initiated by choosing an initial magnetic field in the computational volume and subsequently replacing the lower boundary by the required vector boundary condition. Often, the initial field is a potential field computed from the normal component of the vector magnetogram. The tangential components of this potential field on the bottom boundary are then changed to fully match the vector magnetogram. Replacing the lower boundary with the measurements, results in an initial field that is in general not force-free nor divergence-free at the lower boundary. As a consequence, L will be larger than zero.

Remark that the optimization method requires boundary conditions on all sides of the computational box, and that these boundaries all have the same influence on the final solution. However, solar observations only provide photospheric magnetograms such that only the boundary conditions at the bottom boundary are known. As a consequence, the magnetic field on the lateral and top boundaries of the computational box is approximated by the initial potential field. In reality this potential field can be a poor approximation of the true magnetic field. Therefore it is desirable to decrease the importance of the side an top boundaries with respect to the bottom boundary of the computational box. This can be realized by choosing w_f and w_d to be equal to unity in the entire computational volume, except at the problematic boundaries, where they smoothly drop to zero. As a consequence, the problematic boundaries influence the magnetic field less severely compared to the optimization method without weighting functions. Test calculations performed by Wiegelmann (2004) showed that the use of weighting functions can strongly improve the results. Finally, remark that if vector magnetogram data is available on the whole photosphere, it is in principle possible to reconstruct the complete coronal field. In that case, the computational box has no lateral boundaries such that only the top boundary has to be worried about. This is similar to the potential field source surface approach discussed in Section 2.2.2.2.

Apart from creating boundary layers, the weighting functions w_f and w_d can also be used to increase the importance of the solenoidal condition compared to the force-free condition or vice-versa. For example, by choosing $w_d > w_f$, more effort is spent in making the magnetic field divergence-free than making it force-free. In the test cases considered in Schrijver et al. (2006), the optimal choice was to use equal weighting functions, i.e., $w_d = w_f$. In Chapter 3 we will further investigate the effects of these weighting functions.

2.4.2.2 The Magnetofrictional Method

The magnetofrictional method is in some aspects similar to the optimization method. As we will see below, the magnetofrictional method also starts from an initial state which is then evolved to a force-free state by solving an equation of the same form as Eq. (2.48). Like for the optimization approach, the initial field configuration is often a potential field in the numerical box, where the bottom boundary has been replaced by the measured vector magnetogram. This results in non-zero Lorentz forces at the bottom of the box, which induce flows with plasma velocity $\mathbf{v}$. The magnetofrictional method tries to relax this initial non-equilibrium state towards a relaxed stationary state that is a solution of the MHD equations. This is done by introducing a dissipative term, $\mathbf{D}(\mathbf{v})$, into the momentum equation,

$$\rho\left(\frac{\partial \mathbf{v}}{\partial t}+\mathbf{v}\cdot\nabla\mathbf{v}\right)+\nabla p=\mathbf{j}\times\mathbf{B}+\mathbf{D}. \tag{2.50}$$

The dissipative term should be chosen such that it vanishes when a static equilibrium is reached. Therefore, a friction term is often used as dissipative term: $\mathbf{D}(\mathbf{v})=-\nu\mathbf{v}$. The parameter ν is an arbitrary function of space and time which is usually chosen as

$$\nu=\frac{\mathbf{B}^2}{\mu(t)}, \tag{2.51}$$

where $\mu(t)$ is an adjustable parameter that can depend on time. This parameter is chosen such that it optimizes the relaxation process and reduces oscillations at the end of the relaxation process.

The pressure gradient term and the inertial terms in Eq. (2.50) are often neglected (see, e.g., Yang et al. 1986; Valori et al. 2005) such that Eq. (2.50) can be rewritten as

$$\mathbf{v}=\frac{1}{\nu}\mathbf{j}\times\mathbf{B}. \tag{2.52}$$

The time evolution of the plasma is then governed solely by the induction equation for the magnetic field

$$\begin{aligned}\frac{\partial \mathbf{B}}{\partial t} &= \nabla\times(\mathbf{v}\times\mathbf{B}) && (2.53)\\ &= \mu\nabla\times\left(\frac{[\nabla\times\mathbf{B})\times\mathbf{B}]\times\mathbf{B}}{\mu_0 B^2}\right) && (2.54)\\ &= \mu\mathbf{F}_{\mathrm{mfm}}, && (2.55)\end{aligned}$$

where

$$\mathbf{F}_{\mathrm{mfm}}=\nabla\times\left(\frac{[\nabla\times\mathbf{B})\times\mathbf{B}]\times\mathbf{B}}{\mu_0 B^2}\right). \tag{2.56}$$

Remark that if the initial field has zero divergence, then Eq. (2.53) ensures that the magnetic field remains divergence-free. Moreover, any numerically generated divergence can be minimized using a diffuse approach (see, e.g., Dedner et al. 2002). This is only required if the numerical method used to compute Eq. (2.53) is such that it does not keep the value of $\nabla\cdot\mathbf{B}$ as the magnetic field is updated.

The magnetofricitonal method assumes that there exists a static force-free equilibrium to which the system can relax. Remark however that if a force-free equilibrium indeed exists, reconnection processes may be needed to transform the field line connectivity of the initial field to the equilibrium field. This is in particular the case if the topology of the initial starting field is very different from the topology of the force-free field.

Comparing Eq. (2.55) with Eq. (2.48), reveals that both the optimization method and the magnetofrictional method evolve the magnetic field by using an equation of the form

$$\frac{\partial \mathbf{B}}{\partial t} = \mu \mathbf{F}.$$

A closer inspection of the first term of Eq. (2.46) reveals that $\mathbf{F}_{\mathrm{mfm}}$ is contained in the expression of $\mathbf{F}_{\mathrm{opt}}$, yet $\mathbf{F}_{\mathrm{opt}}$ contains additional terms.

2.4.2.3 Grad-Rubin Method

The Grad-Rubin method uses that equations (2.26) and (2.27) can be decomposed into an elliptical part and a hyperbolic part, as explained at the beginning Section 2.4. These two parts are then successively solved in an iterative manner. More specifically, each iteration step k starts by solving the hyperbolic part to obtain $\alpha^{(k)}$ in the volume Ω:

$$\begin{aligned} \mathbf{B}^{(\mathbf{k})} \cdot \nabla \alpha^{(k)} &= 0 \qquad (2.57)\\ \alpha^{(k)}|_{\partial\Omega^{\pm}} &= \alpha_0, \qquad (2.58) \end{aligned}$$

where $\Omega^{\pm}$ corresponds to the boundaries where the magnetic field has either positive or negative polarity. Subsequently the elliptical part is solved to obtain $\mathbf{B}^{(k+1)}$:

$$\begin{aligned} \nabla \times \mathbf{B}^{(k+1)} &= \alpha^{(k)} \mathbf{B}^{(k)}, \qquad (2.59)\\ \nabla \cdot \mathbf{B}^{(k+1)} &= 0, \qquad (2.60)\\ B_z^{(k+1)}|_{\partial\Omega^{\pm}} &= B_{z0}, \qquad (2.61)\\ \lim_{|r|\to\infty} |\mathbf{B}^{(\mathbf{k+1})}| &= 0. \qquad (2.62) \end{aligned}$$

This iteration is continued until the updated magnetic configuration does not change any more.

$\mathbf{B}^{(0)}$ is normally set equal to the potential field computed from the observed line-of-sight magnetic field. The parameter α can be computed from the magnetogram data as

$$\alpha(x, y) = \frac{1}{B_z} \left(\frac{\partial B_y}{\partial x} - \frac{\partial B_x}{\partial y} \right). \qquad (2.63)$$

Mathematically, the Grad-Rubin method is interesting since it solves the force-free equation as a well posed boundary value problem. For a detailed mathematical study of this method we refer to Amari et al. (2006) and references therein. Remark that the method disregards a large part of the observations, i.e., it uses only one polarity for computing the parameter alpha needed for the boundary conditions (see Eq. (2.58)). Hence, by applying the method twice, once for each polarity, one obtains two solutions. Noise and measurement errors often result in differences between these two solutions (see, e.g., De Rosa et al. 2009). Alternatively, one can attach a certain weight to each boundary value of α, on both polarities. These weights may depend on the noise of the measurements. The final value for α is then obtained as a weighted average of the α values on both footpoints of a field line.

Different approaches exist to fulfil the solenoidal condition, i.e., Eq. (2.60). One possibility is to rewrite Eqs. (2.59)–(2.62) in terms of a vector potential $\mathbf{A}$, with $\nabla \times \mathbf{B} = \mathbf{A}$. This is done in the ‘XTRAPOL’ code as explained in Amari et al. (2006). Alternatively one can keep working with Eqs. (2.59)–(2.62) and minimize the divergence of $\mathbf{B}$ in a least-square sense. This method is for example used in the ‘FEMQ’ code, also introduced in Amari et al. (2006).

Optimization Method Magnetofrictional Method

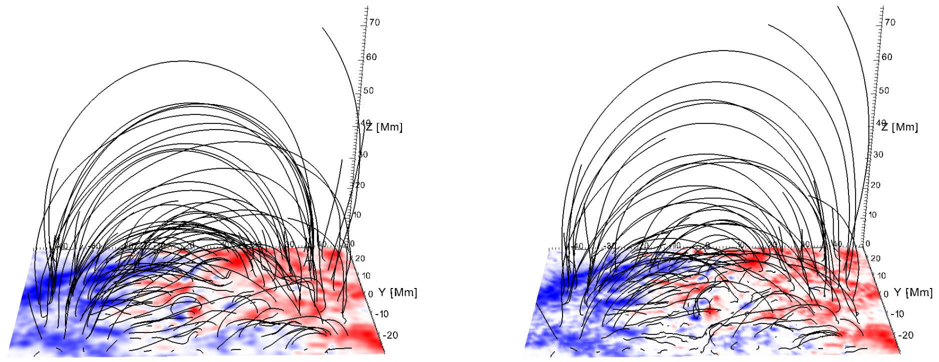

Grad-Rubin Method (XTRAPOL) Grad-Rubin Method (FEMQ)

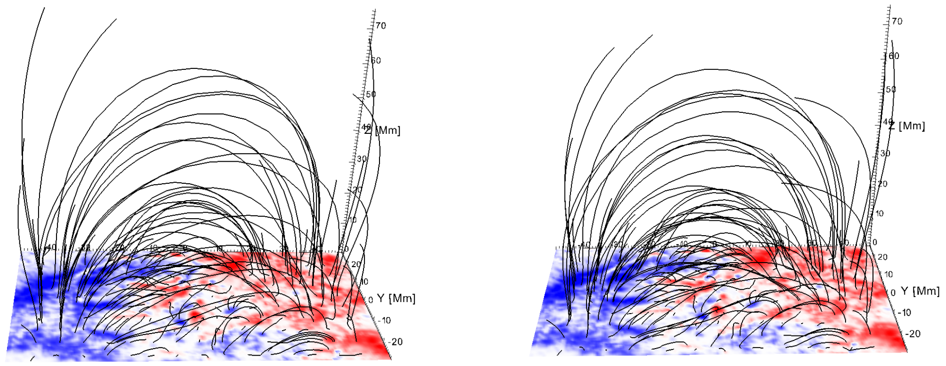

Figure 2.4: The first row shows the resulting magnetic fields of the optimization method and the magnetofrictional method, respectively. The second row shows the results of the XTRAPOL code and the FEMQ code. The starting points for the field lines are in all the plots equal.

2.4.2.4 Discussion

When the different methods are applied to real solar data, they often return magnetic field configurations that are not identical to each other. One of the reason is that the magnetograms which are used as boundary conditions are not exactly force-free, and thus not compatible with a force-free solution. Moreover, since the different methods treat the boundary conditions differently, it is thus not surprising that the resulting fields differ from each other. Many studies have been dedicated to the comparison of the performance of the different methods. Examples are Schrijver et al. (2006, 2008); Metcalf et al. (2008); De Rosa et al. (2009); DeRosa et al. (2015).

DeRosa et al. (2015) applied the optimization method, the magnetofrictional method and the Grad-Rubin method to a magnetogram of the NOAA solar active region 10978 on 2007 December 13. In order to demonstrate how the results of various extrapolation methods differ, the results of four methods are plotted in Fig. 2.4. The magnetogram data is from DeRosa et al. (2015) and the extrapolation results can be downloaded from `http://dx.doi.org/10.7910/DVN/7ZGD9P`. The first row of Fig. 2.4 shows the results of the optimization method and the magnetofrictional method, respectively. The second row shows the results of the XTRAPOL code and the FEMQ code. The starting points for the field lines are in all plots chosen equal, to make a comparison possible. For details about the numerical implementation of the methods we refer to DeRosa et al. (2015).

Figure 2.4 shows that there exist qualitative differences between the field lines obtained with the different methods. Although these differences seem to be small, DeRosa et al. (2015) showed that there are significant quantitative differences when comparing physical quantities like magnetic field energy and helicity. As already mentioned at the start of Section 2.4.2, these differences may be, at least partly, attributed to the different ways of treating the boundary conditions. Apart from this, there are other differences between the methods that may introduce variations. For example, in contrary to the optimization method and the magnetofrictional method, the Grad-Rubin method provides at every iteration a magnetic field that satisfies the solenoidal conditions. As a result, the resulting magnetic field configuration given by the optimization method and the magnetofrictional method are expected to have a larger divergence than the magnetic field obtained from the Grad-Rubin methods.

2.5 Boundary Conditions

The extrapolation methods discussed above are all based on the assumption that the input vector magnetogram is force-free. However, typically only detailed observations of the photospheric magnetic field are available (see Section 1.3), where the force-free approximation is not valid. In Metcalf et al. (1995) it is estimated that the force-free approximation becomes valid at roughly 400 km above the photosphere.

The non-force-freeness of magnetograms can strongly affect the solution obtained from the different extrapolation methods (see Metcalf et al. 2008). One way to resolve this problem is by transforming the photospheric magnetogram into a force-free chromospheric magnetogram. These two magnetograms should be very similar since there is only a thin separation ($\sim$ 400 km) between the photosphere and the start of the force-free region. The chromospheric magnetogram needs to be smoother, since a large part of the magnetic field lines originating from the photosphere extent only a few hundreds of meters above the photosphere, before returning back to the photosphere. The remaining magnetic flux rapidly expands to larger distances (see e.g., Close et al. 2002). For these reasons, it is expected that a chromospheric magnetogram can be obtained from the photospheric magnetogram without performing major modifications. Furthermore, one should also take into account that the photospheric magnetograms contain noise, especially the horizontal components of the magnetic field. Therefore, modifying the magnetogram is justified if the changes that are made smaller or of the size of the errors in the measurements.

Transforming a photospheric magnetogram into a chromospheric magnetogram is generally referred to as *preprocessing*, and was for the first time introduced by Wiegelmann et al. (2006). The preprocessing method described in Wiegelmann et al. (2006) used however a somewhat ad-hoc smoothing to model the expansion of the magnetic field from the photosphere to the chromosphere. In Jiang & Feng (2014), the authors describe a preprocessing method with a more physically justified smoothing procedure. In the next section we introduce a new preprocessing method, which is similar to the preprocessing method of Jiang & Feng (2014).

2.5.1 Preprocessing

The preprocessing technique is based on considering the necessary conditions that are fulfilled by a force-free field. These conditions express that the volume integrals of the total Lorentz force and torque should be zero:

$$\int_\Omega \mathbf{j} \times \mathbf{B} dV = \int_\Omega \mathbf{r} \times (\mathbf{j} \times \mathbf{B}) dV = 0. \tag{2.64}$$

By expressing these equations in terms of the magnetic stress tensor $\mathbf{T}_{ij} = -\frac{\mathbf{B}^2}{2\mu_0}\delta_{ij} + \frac{1}{\mu_0}B_iB_j$, and by using Gauss's Theorem to convert the volume integrals into surface integrals, it was shown in Aly (1989) that a force-free field needs to fulfil the following conditions:

$$\begin{aligned}
F_x &= -\frac{1}{\mu_0}\int_{\partial\Omega} B_xB_z dxdy = 0, && (2.65)\\
F_y &= -\frac{1}{\mu_0}\int_{\partial\Omega} B_yB_z dxdy = 0, && (2.66)\\
F_z &= \frac{1}{2\mu_0}\int_{\partial\Omega} B_x^2 + B_y^2 - B_z^2 dxdy = 0 && (2.67)\\
\tau_x &= \frac{1}{2\mu_0}\int_{\partial\Omega} x(B_x^2 + B_y^2 - B_z^2) dxdy = 0 && (2.68)\\
\tau_y &= -\frac{1}{2\mu_0}\int_{\partial\Omega} y(B_x^2 + B_y^2 - B_z^2) dxdy = 0 && (2.69)\\
\tau_z &= \frac{1}{\mu_0}\int_{\partial\Omega} (yB_xB_z - xB_yB_z) dxdy = 0. && (2.70)
\end{aligned}$$

The first two equations express the that the total force $\mathbf{F}$ on the boundary $\partial\Omega$ vanishes. The last three equations express that the total torque τ on the boundary vanishes. Remark that these equations are a necessary but not a sufficient condition for a magnetic field to be force-free. In addition, the integration in these equations has to be carried out over a closed surface $\partial\Omega$. However, in practice the integration is limited to the bottom magnetogram, since the magnetic field on the side and top boundaries of a computational box is in general not known. When the magnetogram spans a solar active region, this approximation can be justified by choosing a computational box that is large enough such that the magnetic field at the side and top boundaries is close to potential. In the following, $\partial\Omega$ will always refer to the bottom boundary of the computational domain.

Following Jiang & Feng (2014), we split up the magnetic field in a potential part $\mathbf{B}_0$ and a non-potential part $\mathbf{B}_1$. Here the potential part is calculated using the normal component of the magnetogram. This means that

$$\mathbf{B}|_{\partial\Omega} = \mathbf{B}_0|_{\partial\Omega} + \mathbf{B}_1|_{\partial\Omega} = (B_{0x} + B_{1x}, B_{0y} + B_{1y}, B_{0z})|_{\partial\Omega}. \tag{2.71}$$

The first step in the preprocessing procedure is to replace $\mathbf{B}_0|_{\partial\Omega}$ by its value at a height of $\sim 400\text{km}$ above the photosphere. This step can be understood as an attempt to model the smoother chromospheric field given the photospheric one. In the remainder of this section we use $\mathbf{B}$ to denote the magnetic field adapted by the preprocessing method, and $\mathbf{B}_{\text{obs}}$ to denote the magnetic field of the original magnetogram.

The second step towards achieving the force-free magnetogram requires the reformulation of Eqs. (2.65)–(2.70) by using the fact that the potential field $\mathbf{B}_0$ satisfies the equalities identically:

$$\begin{aligned}
F_x &= -\frac{1}{\mu_0}\int_{\partial\Omega} B_{1x}B_{0z} dxdy = 0, && (2.72)\\
F_y &= -\frac{1}{\mu_0}\int_{\partial\Omega} B_{1y}B_{0z} dxdy = 0, && (2.73)\\
F_z &= \frac{1}{2\mu_0}\int_{\partial\Omega} B_{1x}^2 + B_{1y}^2 + 2(B_{0x}B_{1x} + B_{0y}B_{1y}) dxdy = 0 && (2.74)\\
\tau_x &= \frac{1}{2\mu_0}\int_{\partial\Omega} x(B_{1x}^2 + B_{1y}^2 + 2(B_{0x}B_{1x} + B_{0y}B_{1y})) dxdy = 0 && (2.75)\\
\tau_y &= -\frac{1}{2\mu_0}\int_{\partial\Omega} y(B_{1x}^2 + B_{1y}^2 + 2(B_{0x}B_{1x} + B_{0y}B_{1y})) dxdy = 0 && (2.76)\\
\tau_z &= \frac{1}{\mu_0}\int_{\partial\Omega} (yB_{1x}B_{0z} - xB_{1y}B_{0z}) dxdy = 0. && (2.77)
\end{aligned}$$

Since the photospheric magnetogram is in general not force-free, these conditions will not be satisfied. To check how good or bad the raw magnetogram data fulfils conditions (2.72)–(2.77), the following functionals are computed:

$$L_1 = L_{11}^2 + L_{12}^2 + L_{13}^2, \quad L_2 = L_{21}^2 + L_{22}^2 + L_{23}^2, \tag{2.78}$$

where[5]

$$\begin{aligned}
L_{11} &= -\frac{1}{\mu_0} \sum_p \left[B_{1x} B_{0z}\right] \Delta x \Delta y, & (2.79)\\
L_{12} &= -\frac{1}{\mu_0} \sum_p \left[B_{1y} B_{0z}\right] \Delta x \Delta y, & (2.80)\\
L_{13} &= \frac{1}{2\mu_0} \sum_p \left[B_{1x}^2 + B_{1y}^2 + 2(B_{0x}B_{1x} + B_{0y}B_{1y})\right] \Delta x \Delta y & (2.81)\\
L_{21} &= \frac{1}{2\mu_0} \sum_p \left[x(B_{1x}^2 + B_{1y}^2 + 2(B_{0x}B_{1x} + B_{0y}B_{1y}))\right] \Delta x \Delta y & (2.82)\\
L_{22} &= -\frac{1}{2\mu_0} \sum_p \left[y(B_{1x}^2 + B_{1y}^2 + 2(B_{0x}B_{1x} + B_{0y}B_{1y}))\right] \Delta x \Delta y & (2.83)\\
L_{23} &= \frac{1}{\mu_0} \sum_p \left[(yB_{1x}B_{0z} - xB_{1y}B_{0z})\right] \Delta x \Delta y. & (2.84)
\end{aligned}$$

In these expressions, $\sum_p$ denotes a summation over all the grid points p of the bottom boundary, and Δx and Δy are the distances between two adjacent grid points in the x and y direction. Remark that these equations are the discrete versions of Eqs. (2.72)–(2.77). A preprocessing method aims at minimizing L_1 and L_2 by varying the magnetic field components B_{1x} and B_{1y} at each point p of the bottom boundary. However, in minimizing these quantities, the magnetic field should not be allowed to vary too much. As already mentioned above, it would be desirable that the magnetic field is only modified inside or close to the error margins of the data. This means that the following expression should remain small enough

$$L_3 = \frac{1}{2\mu_0} \sum_p \left[(B_{1x} - B_{1x,\mathrm{obs}})^2 + (B_{1y} - B_{1y,\mathrm{obs}})^2\right] \Delta x \Delta y, \tag{2.85}$$

with $\mathbf{B}_{\mathbf{1},\mathrm{obs}}$ the non-potential part of the magnetic field of the original vector magnetogram. Remark that L_3 can be considered as an area integrated magnetic energy deviation. Finally, the chromospheric force-free magnetogram is expected to be smoother than the photospheric magnetogram. Part of this smoothing was already achieved by changing the photospheric $\mathbf{B}_0$ to its value at a distance of $\sim 400\mathrm{km}$ above the photosphere. Additional smoothing can be achieved by minimizing

$$L_4 = \sum_p \left[(\Delta B_x)^2 + (\Delta B_y)^2\right] \Delta x \Delta y, \tag{2.86}$$

where Δ is the 2D-Laplace operator, usually a five-point stencil:

$$\Delta B_{i,j} = B_{i+1,j} + B_{i-1,j} + B_{i,j+1} + B_{i,j-1} - 4B_{i,j},$$

with $p = (i, j)$ a pixel in the grid.

---

[5] Remark that the preprocessing methods developped by Wiegelmann et al. (2006) and Jiang & Feng (2014) do not contain the factors "$\frac{1}{2}$" in the expressions for L_{13}, L_{21} and L_{22}. However, Eqs. (2.72)–(2.77) illustrate that these factors should be included if every force and torque component is equally weighted.

Putting everything together, the preprocessing method tries to minimize a functional of the form

$$L = \frac{\mu_1}{N1}L_1 + \frac{\mu_2}{N_2}L_2 + \frac{\mu_3}{N_3}L_3 + \frac{\mu_4}{N_4}L_4, \tag{2.87}$$

where the μ_i represent different weights and the N_i are some normalisation constants, needed to make the constituents of Eq. (2.87) dimensionally consistent. Appropriate values for these normalization constants are found by realizing that numerical discretization errors inhibit a perfectly force-free field. Therefore, the magnetic field should not be expected to satisfy Eqs. (2.65)–(2.70) more accurately than the numerical computed potential field, and hence N_1 and N_2 are chosen as

$$\begin{aligned} N_1 &= \frac{1}{\mu_0^2}\left(\sum_p \left[B_{0x}B_{0z}\right]\Delta x\Delta y\right)^2 + \frac{1}{\mu_0^2}\left(\sum_p \left[B_{0y}B_{0z}\right]\Delta x\Delta y\right)^2 \\ &\quad + \frac{1}{4\mu_0^2}\left(\sum_p \left[B_{0x}^2 + B_{0y}^2 - B_{0z}^2\right]\Delta x\Delta y\right)^2 \\ N_2 &= \frac{1}{4\mu_0^2}\left(\sum_p \left[x(B_{0x}^2 + B_{0y}^2 - B_{0z}^2)\right]\Delta x\Delta y\right)^2 + \frac{1}{4\mu_0^2}\left(\sum_p \left[y(B_{0x}^2 + B_{0y}^2 - B_{0z}^2)\right]\Delta x\Delta y\right)^2 \\ &\quad + \frac{1}{\mu_0^2}\left(\sum_p \left[(yB_{0x}B_{0z} - xB_{0y}B_{0z})\right]\Delta x\Delta y\right)^2 . \end{aligned}$$

The smoothness of the potential field at a distance of $\sim$ 400km can be used as a reference for the smoothness of the non-potential part. Therefore we choose

$$N_4 = \sum_p \left[(\Delta B_{0z})^2\right]\Delta x\Delta y.$$

In this expression we use only B_{0z}, since the smoothness of B_{0z} should be of the same order as the smoothness of B_{0x} and B_{0y}. This seems reasonable since the smoothness is not expected to have a directional preference. Since we used the potential field to define N_1, N_2, and N_4, a logical choice for N_3 is then

$$N_3 = \frac{1}{2\mu_0}\sum_p \left[\mathbf{B}_{0,\mathrm{obs}}^2\right]\Delta x\Delta y.$$

The weighting factors μ_1 an μ_2 in Eq. (2.87) are normally chosen equal to unity, since there is no reason why the torque component would need a different weight than the force component. The optimal choice of μ_3 and μ_4 depends on the magnetogram under consideration. Often they are chosen equal to or smaller than μ_1 and μ_2 to give greater weight to the force-free conditions (2.65)–(2.70). Moreover, μ_3 has to be chosen sufficiently large to ensure that L_3 remains smaller than $\sum_p \mathbf{B}_{\mathrm{noise}}^2$. For real data, this latter quantity is not exactly known and has thus to be estimated.

Since $L(B_x, B_y, B_z)$ is an explicit functional of the magnetic field components, it can be minimized by solving

$$\nabla_{\mathbf{B}} L(B_x, B_y, B_z) = 0. \tag{2.88}$$

This can be realized by performing an iterative scheme of the form

$$\mathbf{B}^{(i+1)} = \mathbf{B}^{(i)} - \lambda^{(i)}\nabla_{\mathbf{B}} L\left(\mathbf{B}^{(i)}\right), \tag{2.89}$$

where λ defines the step size. This iterative scheme corresponds to the method of steepest descent. The parameter λ can be chosen to optimize the decrease in L (see Jiang & Feng 2014):

$$\lambda^{(i)} = \arg\min L\left[\mathbf{B}^{(i)} - \lambda\nabla_{\mathbf{B}} L\left(\mathbf{B}^{(i)}\right)\right]. \tag{2.90}$$

Alternatively, one can estimate the step size by requiring that the functional should decrease each iteration step. If the functional indeed decreases, one can increase the step size for the next iteration, to accelerate the process. In contrast, if the functional increase during an iteration step, one should repeat this iteration step with a smaller step size, until the functional decrease.

The force-freeness and the torque-freeness of the resulting magnetogram can be quantified by the following metrics:

$$\epsilon_{\text{force}} = \frac{1}{\mu_0 P}\left(\left|\sum_p B_x B_z\right| + \left|\sum_p B_y B_z\right| + \frac{1}{2}\left|\sum_p B_x^2 + B_y^2 - B_z^2\right|\right) \tag{2.91}$$

$$\epsilon_{\text{torque}} = \frac{1}{\mu_0 R_\odot P}\left(\frac{1}{2}\left|\sum_p x(B_x^2 + B_y^2 - B_z^2)\right| + \frac{1}{2}\left|\sum_p y(B_x^2 + B_y^2 - B_z^2)\right| + \left|\sum_p yB_zB_x - xB_yB_z\right|\right), \tag{2.92}$$

with $R_\odot$ the solar radius and P the integrated magnetic pressure given by

$$P = \frac{1}{2\mu_0}\sum_p \mathbf{B}^2 2\mu_0.$$

A force-free magnetogram should satisfy $\epsilon_{\text{force}} \ll 1$ and $\epsilon_{\text{torque}} \ll 1$. The smoothness of the magnetic field can be measured by

$$\mathbf{S} = \frac{1}{N_4}\sum_p (\Delta\mathbf{B})^2 \Delta x \Delta y. \tag{2.93}$$

2.5.2 Example

In this section we will use the bottom boundary of the Low&Lou (LL) semi-analytical solar active region model to demonstrate the preprocessing procedure. To do this, we solve Eq. (2.32) in a cubic volume containing 100^3 pixels. The relevant parameters are $n = 1$, $\ell = 0.3$, $\Phi = \pi/4$, and $a^2 = 0.425$, up to the accuracy of discretization. Since the LL equilibrium is a solution of the force-free equations, it will evidently satisfy conditions (2.65)–(2.70). To imitate a magnetogram obtained from solar observations, we therefore add noise to the LL magnetogram. In Section 1.3, we saw that the measurement error in the transversal component of the magnetic field scales as the square root of photon noise which is of the order of a few tens of Gauss (Wiegelmann et al. 2006). Therefore we choose a noise model of the form

$$\delta B_i = c_i\sqrt{B_i}. \tag{2.94}$$

For the transverse components B_x and B_y, we choose the c_i as a random number between -5 and 5. The line-of-sight component B_z can be measured more precisely, such that the error in the current measurements is only a few G. Therefore we chose c_z as a random number between -0.25 and 0.25. The weighting parameters μ_i in Eq. (2.87) are chosen equal to $\mu_1 = \mu_2 = 1$, $\mu_3 = 10^{-4}$, and $\mu_4 = 1$. This combination of weighting parameters has proven to give good results in Jiang & Feng (2014).

The result is illustrated in Fig. 2.5. The first column shows the LL equilibrium magnetogram, the second row shows the magnetogram with added noise and the last row shows the preprocessed magnetogram. From Table 2.1 it is clear that both the force and torque metric are strongly reduced by the preprocessing method. In addition, the preprocessing method decreases the smoothing parameters S_x and S_y with three orders of magnitude. This smoothing can be seen in Fig. 2.5 since the fine structures present in the magnetograms of the second column are smoothed away by the preprocessing procedure. As already explained at the start of Section 2.5, this smoothness is indeed desirable for a chromospheric magnetogram. At the same time however, one should be careful that the smoothing does not erase too

Metrics	Magnetogram with noise	Preprocessed magnetogram
ϵ_{force}	1.0×10^{-1}	1.7×10^{-3}
ϵ_{torque}	2.0×10^{-4}	6.8×10^{-5}
S_x	1.1×10^{2}	6.2×10^{-1}
S_y	1.1×10^{2}	3.7×10^{-1}
S_z	1.0	1.0

Table 2.1: ϵ_{force}, ϵ_{torque} and $\mathbf{S}$for the magnetogram with added noise and for the preprocessed magnetogram

much details of the original magnetogram. Hence, the parameter μ_4 has to be treated with care when preprocessing real data.

2.6 Beyond Force-Free Fields

The problems with forced magnetograms, as discussed in the previous section, illustrate that the force-free approximation is not valid in the lower corona. This raises the question whether it is possible to go beyond the force-free approximation, and also consider a pressure gradient and gravity. Remark that if this is indeed possible, the preprocessing method would become redundant.

If the plasma flows are still ignored, a non force-free field is described by the equation of magnetohydrostatic equilibrium (see also Eq. (2.4))

$$-\nabla p + \mathbf{j} \times \mathbf{B} + \rho \mathbf{g} = \mathbf{0}.$$

To solve this equation, the prescription of the pressure and the density on the boundaries is required. However, in contrast to the magnetic field, the photospheric density and pressure are (presently) hard to obtain observationally. In Gilchrist & Wheatland (2013), the Grad-Rubin method has been generalized to solve Eq. (2.4) under the additional assumption of zero gravity. In Wiegelmann & Inhester (2003), a generalization of the optimization method is described. At present, the application of these methods is limited due to the lack of good density and pressure measurements. Alternatively, one could try to prescribe a density and pressure profile. For example, exponentially decreasing pressures and density profiles may be a fairly good approximation of the corona. A solution of Eq. (2.4), obtained by a generalized optimization method, can then be used to obtain a force-free chromospheric vector magnetogram.

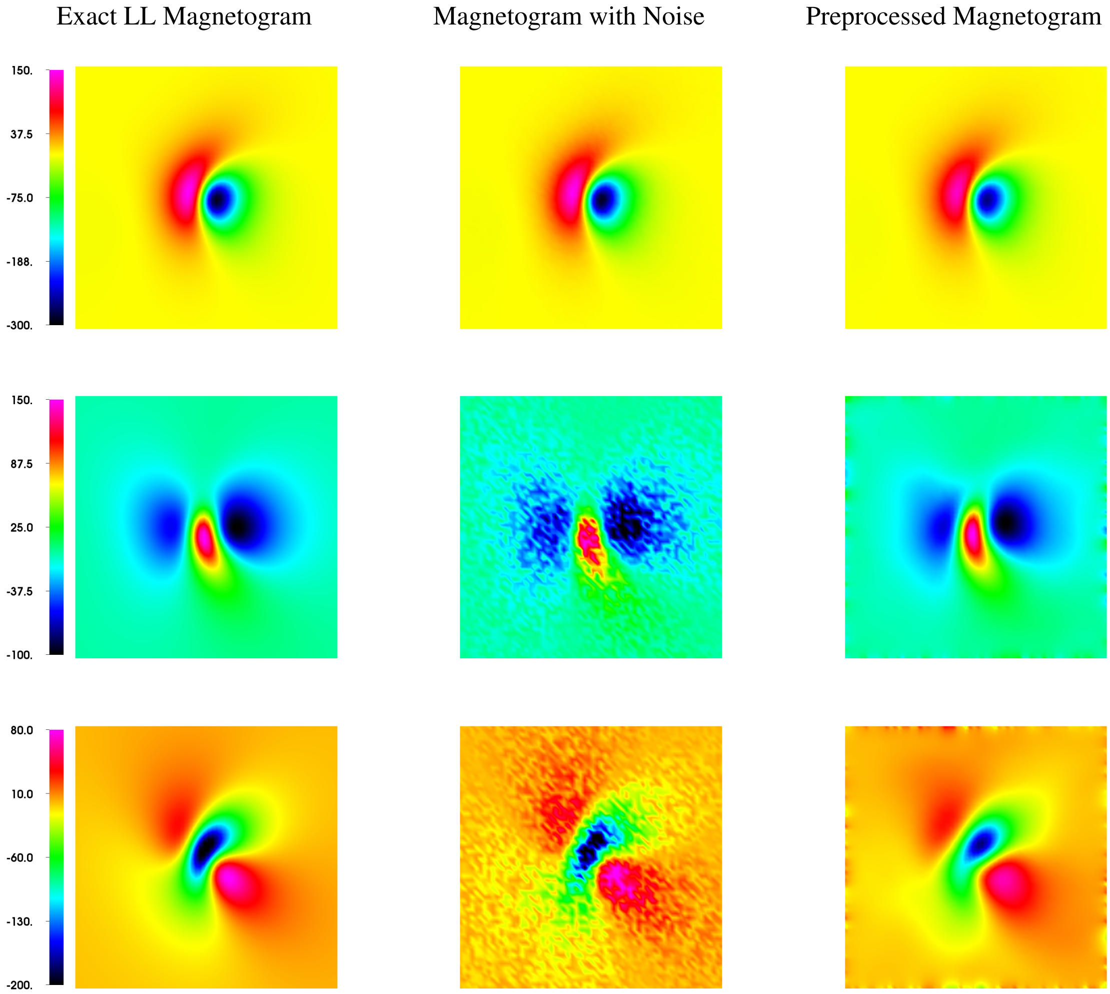

Figure 2.5: The first row shows B_z for the original LL equilibrium, the magnetogram with added noise and the preprocessed magnetogram, respectively. The second and third row show the same but for B_x and B_y, respectively.

Chapter 3

The Optimization Approach

Methods for the extrapolation of the coronal magnetic field try to obtain solutions of a system of partial differential equations starting from appropriate boundary conditions. Apart from solving the equations, the methods also need to be able to handle solar data as boundary conditions. The ability of the numerical scheme to solve the system of differential equations can be tested using semi-analytical solutions. Judging the performance of an extrapolation method using real solar data is harder, since the extrapolated field can not be compared with the unknown exact field.

Section 2.4.2 of the previous chapter, introduced three different extrapolation methods. In this chapter we will take a closer look at one of these methods, namely the optimization method. Section 3.1 provides details about the numerical implementation of our optimization method. Thereafter, in Sections 3.2 and 3.3, the performance of the code is tested by using the semi-analytical nonlinear force-free fields introduced in the previous chapter. In Section 3.4, the optimization method is applied to a real solar magnetogram, and compared to results of other extrapolation methods that used the same magnetograms as boundary data.

3.1 Numerical Implementation

This section discusses the numerical implementation of our optimization code. The mathematical details of the optimization method were already given in Section 2.4.2. We recall the basic steps of the method:

1. Compute the potential field from the normal magnetic component of the magnetogram, and set the initial magnetic field $\mathbf{B}^{(0)}$ equal to this potential field.
2. Replace the transverse field components of the initial potential field $\mathbf{B}^{(0)}$ at the photospheric boundary by the transverse field components of the magnetogram. The magnetic field at the lower boundary is thus equal to the (preprocessed) vector magnetogram.
3. Minimize the functional L (see Eq. (2.40)) by evolving the magnetic field as Eq. (2.48):

$$\frac{\partial \mathbf{B}}{\partial t} = \mu \mathbf{F}_{\mathrm{opt}}.$$

While doing so, the magnetic field is kept constant on the boundaries of the computational box.

In our code we split the magnetic field $\mathbf{B}$ into a potential part $\mathbf{B}_0$ and a non-potential part $\mathbf{B}_1$, i.e,

$$\mathbf{B} = \mathbf{B}_0 + \mathbf{B}_1.$$

This allows for a more accurate computation of the non-potential part during the optimization procedure. The potential field $\mathbf{B}_0$ is computed by using the normal component of the magnetogram. Since the magnetogram does not change during the optimization procedure, the potential field $\mathbf{B}_0$ remains fixed. Therefore, we can write Eq. (2.40) as

$$\frac{\partial \mathbf{B}}{\partial t} = \frac{\partial \mathbf{B_1}}{\partial t} = \mu \mathbf{F}_{\mathrm{opt}}.$$

This is implemented in a single-step forward Euler manner:

$$\mathbf{B}_1^{(k+1)} = \mathbf{B}_1^{(k)} + \mathbf{F}_{\mathrm{opt}}^{(k)} \Delta t, \tag{3.1}$$

where $\mathbf{F}_{\mathrm{opt}}^{(k)}$ is computed using $\mathbf{B}_1^{(k)}$ and $\mathbf{B}_0$. Remark that the "temporal" accuracy is of no concern here, since t is just an iterative parameter, and we are only interested in the final field. The step size Δt is varied during the iteration procedure to accelerate the convergence process. When $L(\mathbf{B}^{(k+1)}) \leq L(\mathbf{B}^{(k)})$, the iteration was successful and Δt is multiplied with a factor of 1.01. This is done to accelerate the optimization procedure. On the other hand, if $L(\mathbf{B}^{(k+1)}) > L(\mathbf{B}^{(k)})$, the time step Δt is halved, and the iteration step is repeated. The iteration is continued until the updated magnetic field configuration does not change any more.

Eq (2.44) shows that several spatial derivatives have to be computed in order to obtain the functional $\mathbf{F}_{\mathrm{opt}}$. These spatial derivatives are computed using standard centred fourth order finite differences. The computational grid is assumed to be rectilinear, with each direction having a constant spacing between the grid points. This constant spacing can be different for the different directions. Furthermore, there is also a grid-refinement scheme implemented in the optimization method. This scheme allows applying the optimization procedure on successively finer meshed grids. Each time, the solution obtained on the coarser grid is interpolated to a finer grid, and subsequently used as the initial field of the optimization method on the finer grid. Such a grid-refinement scheme improves the quality of the solution, and decreases the total computation time of the code considerably.

3.2 The Low and Lou Test Cases

Before applying our optimization code to real solar data, we test it using semi-analytical solutions. Obviously, if the the code is unable to extrapolate a smooth analytical test field, then there is little hope that the code will perform well on noisy solar data. In this section the performance of our optimization code will be tested by applying the code to boundary data provided by the Low and Lou (henceforth LL) equilibrium fields (see Section 2.4.1.1). The benefit of using semi-analytical test cases is that the extrapolated magnetic field can be compared qualitatively and quantitatively with the exact LL fields. The LL equilibria have become standard reference cases for testing nonlinear force-free extrapolation codes (see, e.g., Amari et al. 1999; Wheatland et al. 2000; Wiegelmann & Neukirch 2003; Yan & Li 2006; Amari et al. 2006; Inhester & Wiegelmann 2006; Schrijver et al. 2006; Wiegelmann 2007).

Schrijver et al. (2006) considered two specific cases of the LL solutions to test and compare different extrapolation methods. We will run our code using the same test cases and with the same resolution, such that we can compare the results of our optimization code with the results in Schrijver et al. (2006). The test cases are the following:

(I) The first test case uses LL parameters $n = 1$, $a^2 = 0.427$, $l = 0.3$, and $\Phi = \pi/4$. For the meaning of these parameters we refer to Section 2.4.1.1. The calculations will be performed in a cubical box, containing 64^3 pixels and $(x, y, z) \in [-1, 1] \times [-1, 1] \times [0, 2]$. Two sub-cases are considered:

  - Case Ia: the LL equilibrium field is provided on all boundaries of the computational box (same as Case I of Schrijver et al. (2006)).

- Case Ib: the LL equilibrium field is only provided on the lower boundary.

(II) The second test case uses LL parameters $n = 1$, $a^2 = 8.036$, $l = 0.3$, and $\Phi = 4\pi/5$. Like in Case I, the test region, i.e., the region where we will compute different performance metrics (see below), is a cubical box, containing 64^3 pixels and $(x, y, z) \in [-1, 1] \times [-1, 1] \times [0, 2]$. Again two sub-cases are considered:

  - Case IIa: the LL equilibrium field is provided on all boundaries of the computational box.
  - Case IIb: the LL equilibrium field is only provided on the lower boundary (same as Case II of Schrijver et al. (2006)). Following Schrijver et al. (2006), we apply the optimization method in a rectangular computational box of resolution $192 \times 192 \times 64$, and $(x, y, z) \in [-3, 3] \times [-3, 3] \times [0, 2]$. This computational box is centred on the 64^3 test cube.

The exact LL equilibria for Case I and II are plotted in Fig. 3.1. The first row shows the magnetic fields in the complete computational box. The second rows shows the fields in the inner volumes outlined by the cubes in the first row of the figure. Remark that the magnetic field lines of Case I extend to much larger height than those of Case II.

The fields are extrapolated using weighting functions w_f and w_d equal to unity. Only in Section 3.2.4, where the effect of using different weighting functions is tested, we use weighting functions that differ from unity.

3.2.1 Metrics

To quantify the performance of the optimization code, Schrijver et al. (2006) introduced a set of metrics that measure the agreement between the extrapolated field and the model field. The first two metrics measure the directional differences between the extrapolated field $\mathbf{b}$ and the LL equilibrium $\mathbf{B}$. They are given by

$$C_{\text{vec}} = \frac{\sum_i \mathbf{B}_i \cdot \mathbf{b}_i}{(\sum_i |\mathbf{B}_i|^2 \sum_i |\mathbf{b}_i|^2)^{1/2}}, \qquad C_{\text{CS}} = \frac{1}{M} \sum_i \frac{\mathbf{B}_i \cdot \mathbf{b}_i}{|\mathbf{B}_i||\mathbf{b}_i|}, \tag{3.2}$$

where $\sum_i$ denotes the summation over all the grid points i, and M is the total number of points. Remark that both metrics equal unity when the vector fields are identical, equal zero when the vector fields are orthogonal, and are negative when the vector fields are anti-parallel.

The next two metrics contain information about the agreement between the vector fields, both in direction and magnitude. They are given by

$$E_n = \frac{\sum_i |\mathbf{b_i} - \mathbf{B_i}|}{\sum_i |\mathbf{B_i}|}, \qquad E_m = \frac{1}{M} \sum_i \frac{|\mathbf{b}_i - \mathbf{B}_i|}{|\mathbf{B}_i|}. \tag{3.3}$$

In contrast with the first two metrics, the metrics E_n and E_m equal zero when the vector fields are identical. Therefore, to make the comparison between the metrics easier, we consider instead $E'_n = 1 - E_n$ and $E'_m = 1 - E_m$. Apart from the differences in direction and magnitude, we are also interested in the differences between the energy content of the vector fields. Therefore, we introduce the following metrics

$$\epsilon = \frac{\sum_i |\mathbf{b}_i|^2}{\sum_i |\mathbf{B}_i|^2}, \qquad \epsilon_p = \frac{\sum_i |\mathbf{b}_i|^2}{\sum_i |\mathbf{B}_{p,i}|^2}, \tag{3.4}$$

where $\mathbf{B}_p$ is the potential field computed from the normal magnetic component of the lower boundary. Remark that, whereas the metrics C_{vec}, C_{CS}, E'_n and E'_m measure local differences between the vector fields, the energy metrics give a measure of global differences.

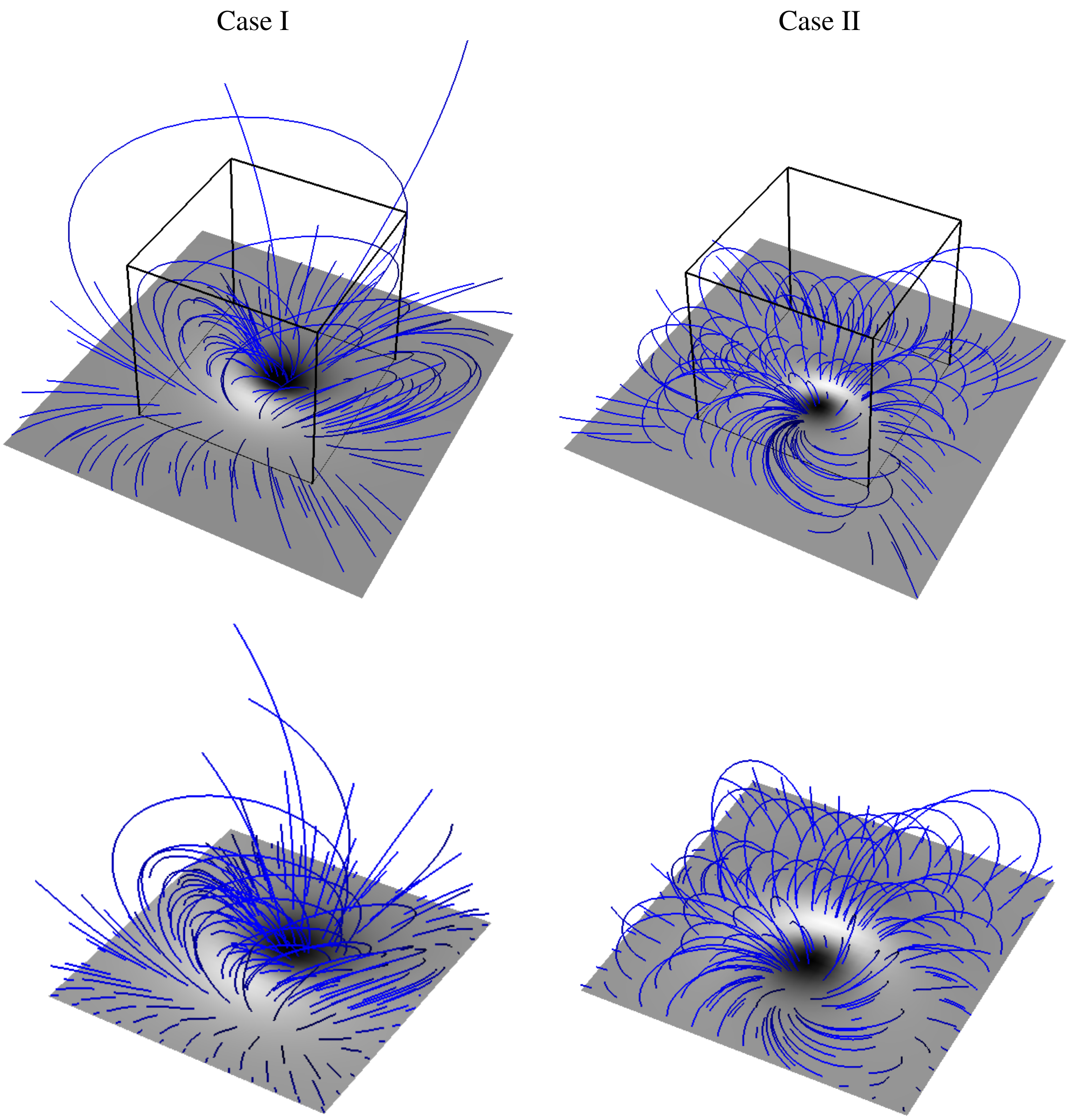

Case I

Case II

Figure 3.1: LL magnetic fields for Case I and Case II. The grey scale is proportional to the vertical magnetic field component, with positive (negative) values corresponding to a white (black) colour. The first column shows the exact LL field for Case I, whereas the the second column shows the magnetic field of Case II. The second row gives a close-up of the black boxes outlined in the first row.

To measure the force-freeness of the solution, we introduce the following metric (see, e.g., Wheatland et al. 2000):

$$\mathrm{CW}\sin\theta = \frac{\sum_i |\mathbf{j}_i||\sin\theta_i|}{\sum_i |\mathbf{j}_i|}, \tag{3.5}$$

where

$$|\sin\theta_i| = \frac{|\mathbf{j}_i \times \mathbf{b}_i|}{|\mathbf{j}_i||\mathbf{b}_i|}. \tag{3.6}$$

This metric gives the current weighted average of the sine of the angle between the magnetic field and the current density. For a perfect force-free field, the current is parallel to the magnetic field and hence this metric becomes zero. Remark that from the different metrics introduced in this section, CW $\sin\theta$ is the only one that can be computed when the exact magnetic field is not known, as in the case when using real solar data.

3.2.2 Case I

Figure 3.2 compares the exact LL equilibrium with the computed field for Case Ia and Case Ib. Figure 3.3 zooms in on the inner volume of 32^3 pixels. For Case Ia, a visual inspection of Figs. 3.2 and 3.3 reveals that the extrapolated magnetic field is very similar to the LL equilibrium. This is also quantitatively confirmed by considering the values of the metrics given in Table 3.1. Remark that the metrics for the inner box are slightly worse than the metrics for the full domain. This can be explained by remarking that the LL magnetic field of Case Ia deviates stronger from the initial potential field at the center of the box than in the outer regions.

Test Case Ia was also used in Schrijver et al. (2006) to examine the performance of different extrapolation methods. Comparing their results with our results reveals that our optimization code has better values for all metrics than the extrapolation methods discussed in Schrijver et al. (2006). This is true both for the full domain and in the inner box of 32^3 pixels.

For Case Ib, the LL equilibrium was only specified on the lower boundary. This means that the magnetic field on the side and top boundaries remains equal to the potential field during the optimization procedure. In other words, these boundaries have the wrong boundary conditions and therefore, it is not surprising that the values of the metrics of Case Ib are lower than those of Case Ia. Remark however that the metrics of the Case Ib field still performs significantly better than the potential field. Figure 3.2 clearly shows that the extrapolated field of Case Ib deviates more from the exact LL field than for Case Ia. Moreover, remark that for Case Ib, the metrics of the inner 32^3 pixel volumes are all better than the metrics of the complete volume. A visual inspection of Figs. 3.2 and 3.3 indeed shows that the magnetic field is much better reproduced in the inner volume. This is because the inner volume is further away from the side and top boundaries. For Case Ia, there was not such a difference between the complete domain and the inner box, since the correct boundaries were provided on all sides of the computational box. This difference between Case Ia and Case Ib illustrates that the boundary conditions can strongly influence the final extrapolated field.

3.2.3 Case II

The extrapolated fields of Case II are shown in Figs. 3.4 and 3.5. The values for the performance metrics are given in Table 3.2. Similar conclusions as for Case I can be drawn. A qualitative inspection of Figs. 3.4 and 3.5 illustrate that the computed field is similar to the LL model field. Looking at the metrics in Table 3.2, we see that the metrics of Case II are relatively good, yet not as good as the metrics for Case I. Especially the metrics E'_m and C_{CS} are considerably better in Case I than in Case II. These differences

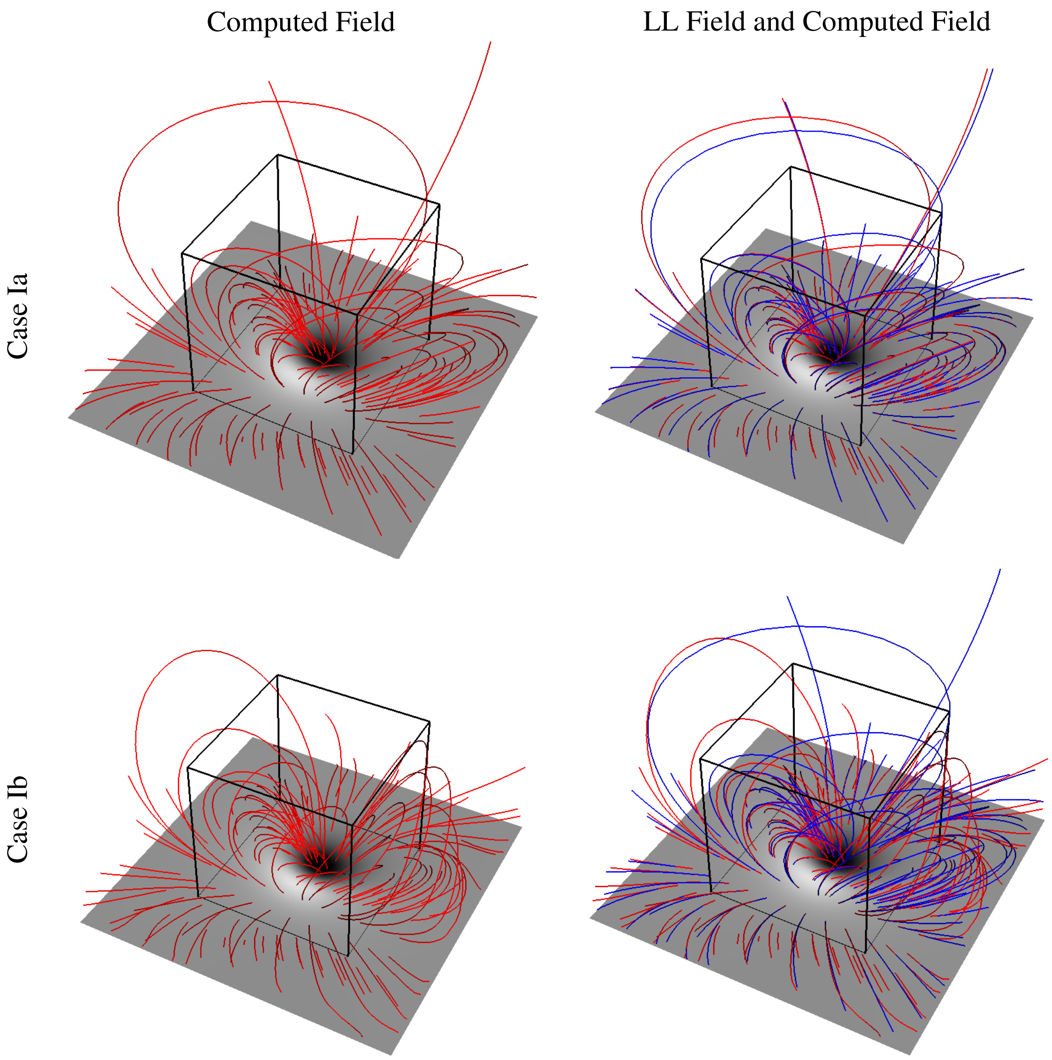

Figure 3.2: Magnetic fields for Case I. The grey scale is proportional to the vertical magnetic field component, with positive (negative) values corresponding to a white (black) colour. The left column shows the computed field. The right column shows the exact LL field (blue) and the computed field (red) together. The first row shows Case Ia, while the second row shows Case Ib.

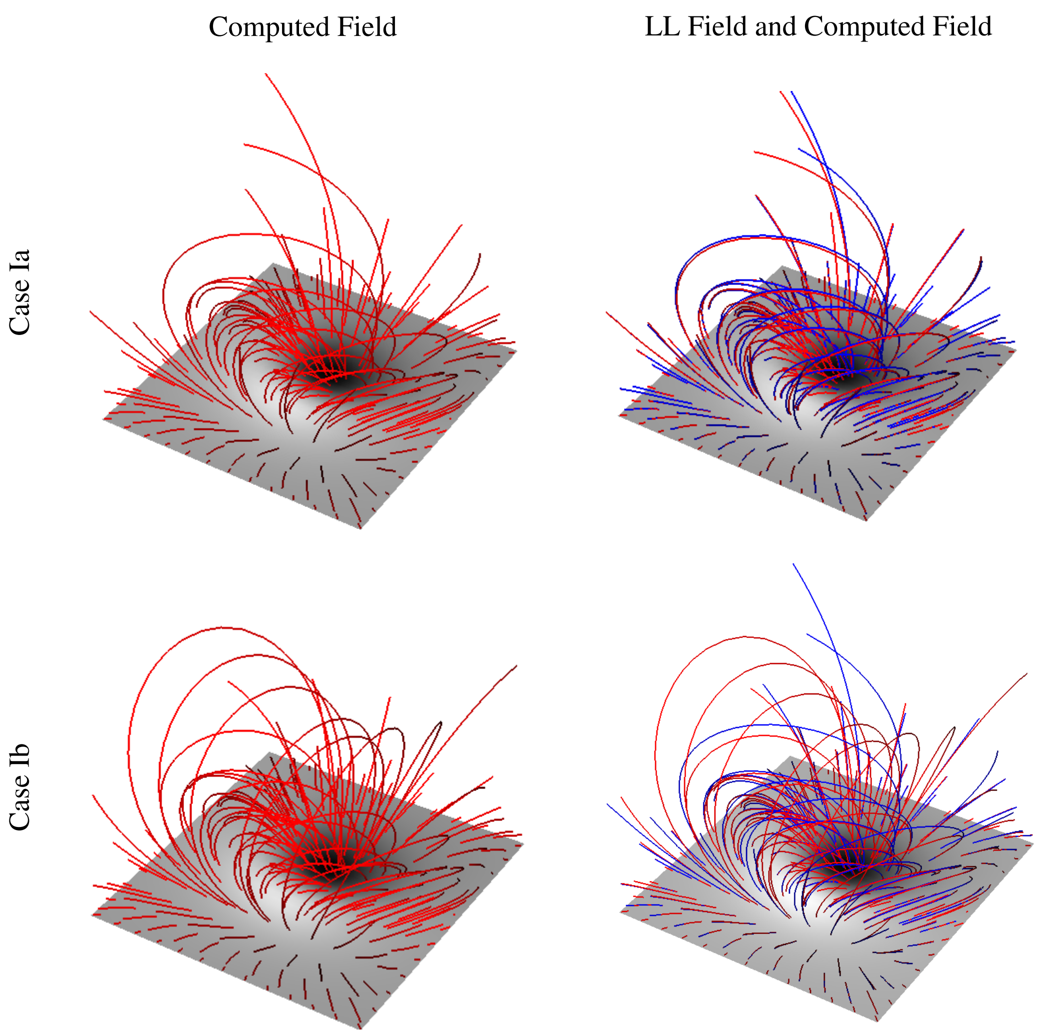

Figure 3.3: Same as in Fig. 3.2, but for the cubes outlined in Fig. 3.2.

Model	C_{vec}	C_{CS}	E'_n	E'_m	ϵ	ϵ_p
Complete volume of 64^3 pixels.						
LL equilibrium	1	1	1	1	1	1.29
Case Ia	1	1	0.99	0.98	1	1.3
Case Ib	0.99	0.81	0.74	0.43	0.99	1.28
Potential field	0.85	0.81	0.44	0.35	0.77	1.0
Inner volume of 32^3 pixels.						
LL equilibrium	1	1	1	1	1	1.24
Case Ia	1	1	0.98	0.96	1.01	1.25
Case Ib	1	0.81	0.84	0.48	1.01	1.26
Potential field	0.86	0.87	0.48	0.39	0.80	1.0

Table 3.1: Metrics for Case I.

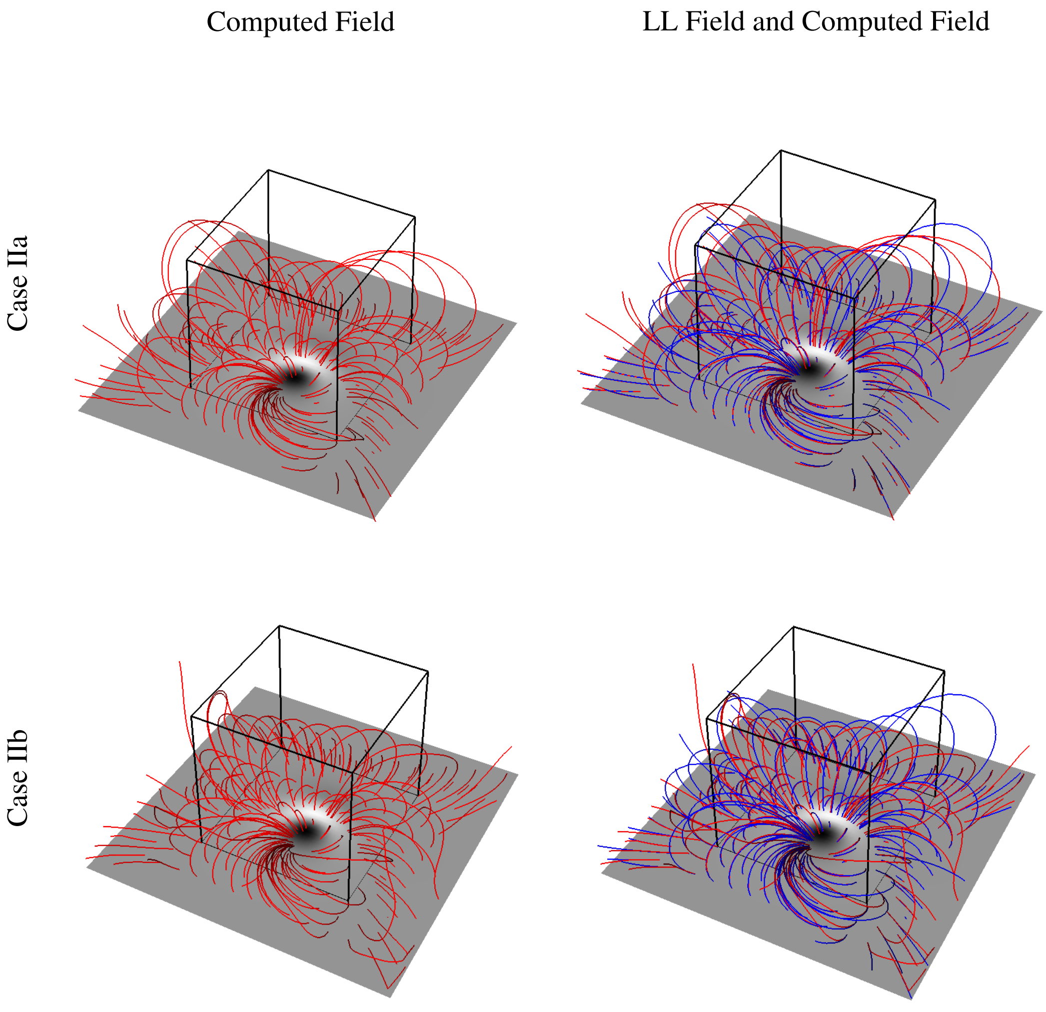

Figure 3.4: Analogous to Fig. 3.2, but for Case II.

between Case I and Case II are possibly caused by the differences in the way the strength of the magnetic field decreases with height. The strength of the magnetic field decreases much faster with height for the Case II magnetic field than for the Case I magnetic field. For Case II, the weak magnetic field in the upper regions of the computational box leads to strong deviations between the computed field and the exact LL field. This also explains why C_{vec} and E_n' are much closer to unity than the corresponding C_{CS} and E_m'. From their definition (see Section 3.2.1), we see that E_n and C_{vec} give more weight to regions with a stronger field. Consequently, these measures are less affected by deviations in regions where the field is weak.

Remark that for both Case IIa and Case IIb, the metrics of the inner 32^3 volume are much better than the metrics of the complete box. For Case IIb, this is partly a consequence of specifying only the LL equilibrium on the lower boundary. A similar observation was made for Case Ib. However, in contrast to Case IIa, Case Ia did not show this feature. The much better performance of Case II in the smaller box can be attributed to strong deviations in the upper regions of the simulated region. These weak field regions are mainly situated above the inner test volume. Again, this illustrates that the performance of the optimization code decreases for weaker magnetic fields.

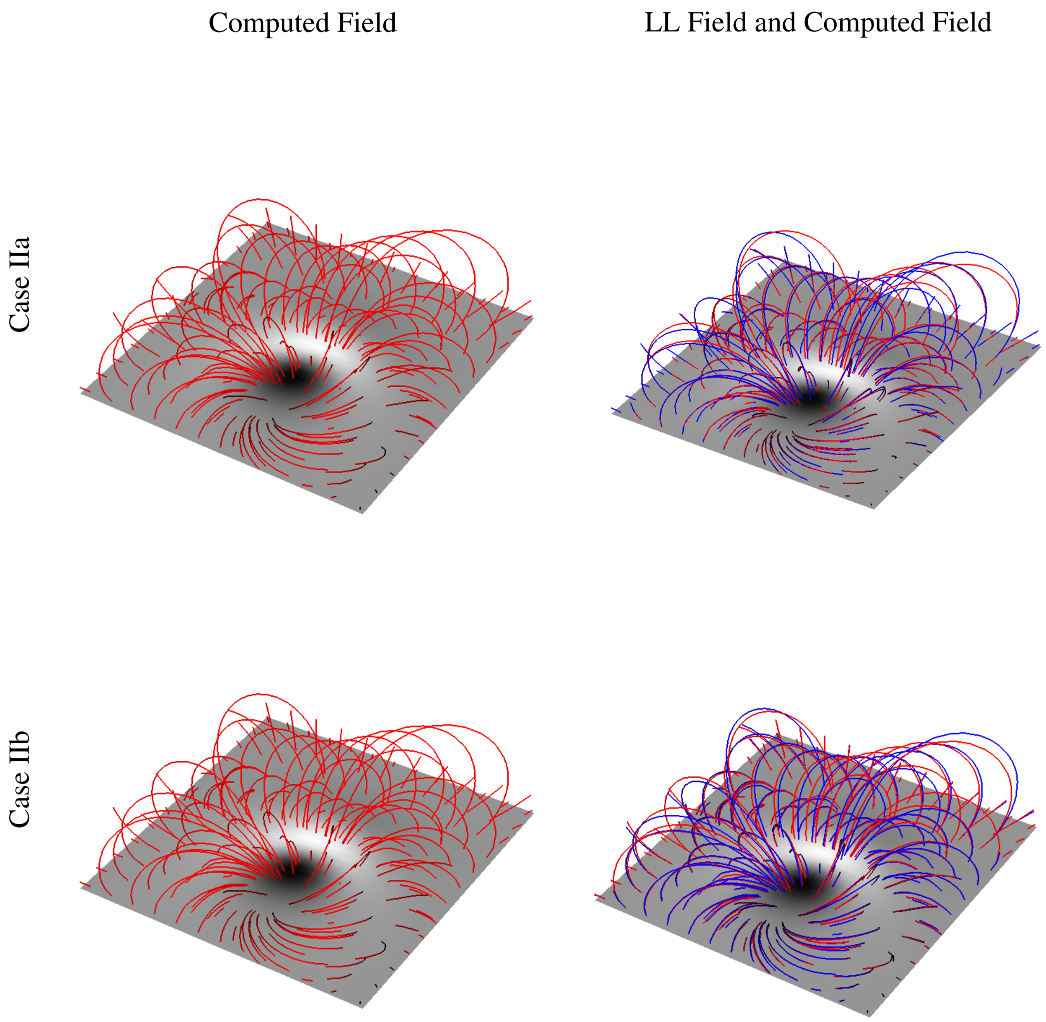

Figure 3.5: Details of the boxes outlined in Fig. 3.4.

Model	C_{vec}	C_{CS}	E'_n	E'_m	ϵ	ϵ_p
Complete volume of 64^3 pixels.						
LL equilibrium	1	1	1	1	1	1.10
Case IIa	1	0.81	0.94	0.53	1.02	1.13
Case IIb	1	0.65	0.90	−0.42	1.02	1.13
Potential field	0.92	0.35	0.47	-0.63	0.91	1
Inner volume of 32^3 pixels.						
LL equilibrium	1	1	1	1	1	1. 10
Case IIa	1	0.96	0.95	0.69	1.02	1.13
Case IIb	1	0.68	0.95	0.21	1.02	1.13
Potential field	0.92	0.66	0.57	0.30	0.91	1

Table 3.2: Metrics for Case II.

w_f	w_d	C_{vec}	C_{CS}	E'_n	E'_m	ϵ	$\text{CW}\sin\theta$	$\frac{L_d}{w_d}\times 10^{-14}$	$\frac{L_f}{w_f}\times 10^{-14}$	$\left(\frac{L_f}{w_f}+\frac{L_d}{w_d}\right)\times 10^{-14}$
1	0	0.99	0.89	0.76	0.52	0.99	0.099	21.4	1.46	122.8
1	0.1	0.99	0.87	0.77	0.50	1.01	0.08	4.41	1.17	5.58
1	0.5	0.99	0.85	0.75	0.46	0.99	0.11	2.50	1.46	3.96
1	1	0.99	0.82	0.73	0.44	0.99	0.13	2.12	1.73	3.85
1	1.5	0.99	0.80	0.71	0.42	1.00	0.15	1.98	1.95	3.92
1	2	0.99	0.79	0.70	0.41	0.99	0.15	1.90	2.10	4
1	10	0.98	0.73	0.65	0.35	1.00	0.21	1.69	3.16	4.85
0	1	0.98	0.75	0.63	0.37	0.95	0.29	1.66	4.64	6.30

Table 3.3: Metrics using different weights for Case Ib

3.2.4 Effect of the Weighting Functions

In this section, we take a closer look at the effect of the weighting functions w_f and w_d in Eq. (2.40). To do this, we run the optimization code several times for test Case Ib, while using each time a different pair of weighting functions. The results are quantified using the same metrics as before. In addition to these metrics, we also look at the values of L_f/w_f, L_d/w_d and $L_f/w_f + L_d/w_d$ (see Eqs. (2.40) and (2.41)). We recall that L_f/w_f gives a measure of the total force present in the computational volume, whereas L_d/w_d gives a measure of the integrated divergence of the magnetic field.

The results are given in Table 3.3. As expected, we see that if only the Lorentz-force is minimized, i.e., when $w_f = 1$ and $w_d = 0$, the lowest values of L_f/w_f and $\text{CW}\sin\theta$ are attained. However, this choice of weighting functions gives the highest value for L_d/w_d.[1] Increasing w_d relatively to w_f results in increasing values of $\text{CW}\sin\theta$ and L_f/w_f, and decreasing values of L_d/w_d, again as expected. Looking at the values of $\left(\frac{L_f}{w_f}+\frac{L_d}{w_d}\right)$, we see that the lowest value is obtained for $w_f = w_d = 1$. Therefore, one could select $w_f = w_d = 1$ as the optimal choice of weighting functions. However, the metrics C_{vec}, C_{CS}, E'_n, E'_m and ϵ tell a different story. Inspecting their values reveals that the extreme case $w_f = 1$ and $w_d = 0$ gives the best metric values. However, for this case the metric L_d/w_d is an order of magnitude larger than for the other cases, indicating the presence of a relatively large divergence. Maybe more interestingly, compared to the the $w_f = w_d = 1$ case, we see that case $w_f = 1$ and $w_d = 0.1$ has a L_d/w_d value of the same order of magnitude and improves some metrics up to 6%. This indicates that L_f/w_f and L_d/w_d may not be the best indicators for goodness of the extrapolation

3.2.5 Effect of Preprocessing

Preprocessing was introduced in Section 2.5.1. We recall that it is a method developed for removing forces present in photospheric magnetograms. In this section, we will investigate the performance of the optimization code when using preprocessed data. This is done by adding first artificial noise to the lower boundary of the LL equilibrium field. The noise model we use is the same as the one introduced in Section 2.5.2, when we illustrated the preprocessing method. We recall that the noise is chosen

---

[1] Remark that we do not divide by zero here since L_d also contains the w_d term.

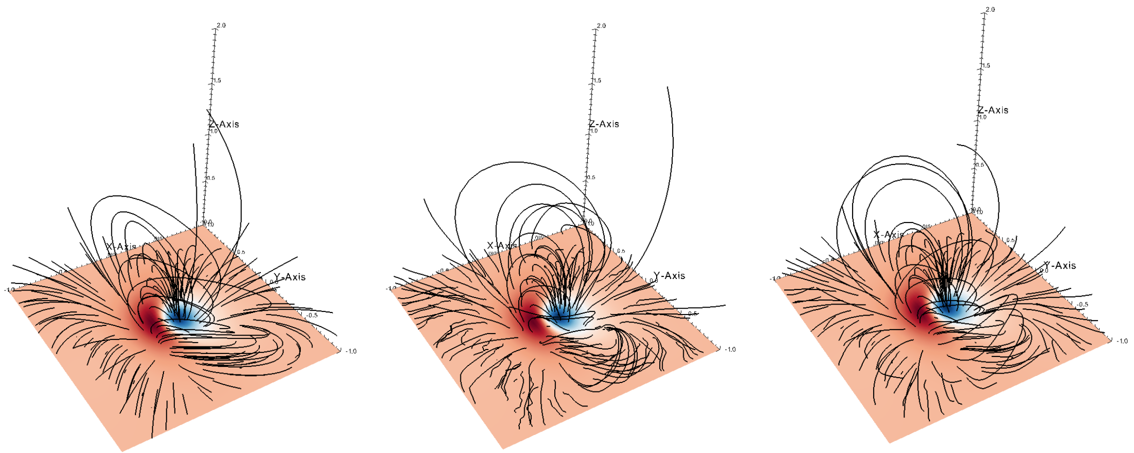

(a) **(b)** **(c)**

Figure 3.6: The left figure gives the exact LL magnetic field. The middle figure shows the reconstructed field using the noisy data without preprocessing. The right figure shows the reconstructed field using the preprocessed noisy data. The color-code is proportional to B_z.

Metrics	Magnetogram with noise	Preprocessed magnetogram
ϵ_{force}	1.4×10^{-1}	7.2×10^{-3}
ϵ_{torque}	2.7×10^{-4}	4.9×10^{-5}

Table 3.4: ϵ_{force} and ϵ_{torque} for the magnetogram with added noise and for the preprocessed magnetogram

proportional to the square root of the magnetic field, to imitate a real magnetogram. Here we extend this noise model by rotating the transverse magnetic field over an angle of 180° in a set of randomly selected points of the magnetogram. The total number of these points covers 5% of the complete magnetogram. In this ways, we imitate the 180° ambiguity (see Section 1.3).

As LL test case, we consider Case Ib of previous sections. The preprocessing method is performed using $\mu_1 = \mu_2 = 1$, $\mu_3 = 10^{-4}$, and $\mu_4 = 1$. For this choice of parameters, we still have that L_3 (see Eq (2.85)) is smaller than $\sum_p \mathbf{B}^2_{\text{noise}}$, indicating that the magnetic field is altered without exceeding the noise level. Table 3.4 gives the force and torque measures ϵ_{force} and ϵ_{torque} (see Eq. (2.91)) for the noisy and the preprocessed magnetogram. We see that the integrated force is lowered by two orders of magnitude and the integrated torque by one order of magnitude. The preprocessed magnetogram fits the force-free conditions thus substantially better.

Panel (a) of Fig 3.6 shows the original LL solution. Panel (b) shows the nonlinear force-free reconstruction using the magnetogram with added noise, without any preprocessing. In panel (c), the magnetic field extrapolated from a preprocessed magnetogram is shown. It can be seen that the preprocessed magnetogram reproduces a much smoother magnetic field, which is in better agreement with the exact LL model. This qualitative visual inspection is confirmed quantitatively by inspecting the values of the metrics given in Table 3.5. All the metrics of the preprocessed magnetogram are at least as good as the magnetogram that was not preprocessed. In addition, remark that the metrics of the extrapolation using the preprocessed magnetogram are close to the metrics of the extrapolation using the exact LL magnetogram. Preprocessing has thus a positive effect on the performance of the optimization code.

Model	C_{vec}	C_{CS}	E'_n	E'_m	ϵ	ϵ_p
Complete volume of 64^3 pixels.						
LL equilibrium	1	1	1	1	1	1.10
Using exact magnetogram	0.99	0.81	0.74	0.43	0.99	1.28
Using noisy magnetogram	0.97	0.81	0.65	0.42	1.02	1.33
Preprocessed noisy magnetogram	0.99	0.81	0.71	0.45	1.013	1.32

Table 3.5: Metrics for Case Ib, using a magnetogram with added noise.

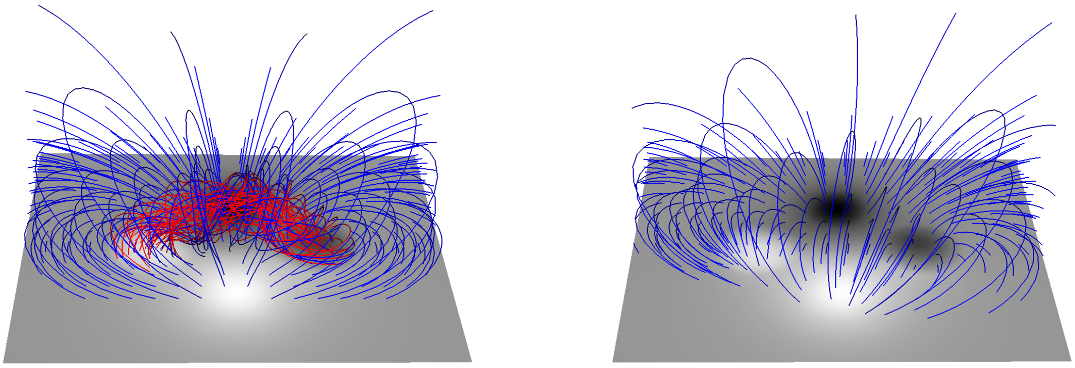

Figure 3.7: Left: Titov-Démoulin Flux Rope model. The magnetic field of the flux-rope is coloured red. Right: Potential field computed from the B_z component of the Titov-Démoulin model. The grey-scale gives gives B_z, with black (white) for negative (positive) values of B_z.

3.3 The Titov-Démoulin Flux Rope Test Cases

In this section, we will use the Titov-Démoulin (henceforth TD) flux-rope model (see Section 2.4.1.2) to test the optimization code. Using a magnetic field that contains a flux-rope as test case is for several reasons interesting. First of all, it is believed that magnetic flux-ropes are often present in active solar regions. These flux-ropes are expected to play an important role in the launch of coronal mass ejections (see Section 1.2.3). Therefore it is desirable that a model of the coronal magnetic field is able to reproduce a magnetic flux-rope configuration. Such a magnetic topology was not present in the LL equilibria, which makes the TD model a complementary test case. Moreover, for the LL test case, the corresponding potential field had a magnetic topology similar to the exact LL field. This is not the case for a flux-rope configuration, since the corresponding potential field does not contain a flux-rope. This clear difference between the flux-rope model and the potential field is illustrated in Fig. 3.7.

It is important to realise that the TD flux-rope model is only approximately force-free. Therefore the optimization method cannot be expected to reproduce the exact magnetic topology of the model. It is expected that in the solar corona, a magnetic configuration like the TD flux-rope model would rapidly relax to a force-free equilibrium. Since the optimization method searches for a force-free topology, it can be expected that the optimization code will rather converge to the relaxed force-free equilibrium instead of the exact TD flux-rope model.

As test cases, we use the two different flux-rope models that where developed by Titov et al. (2014) and discussed in Section 2.4.1.2. Following Titov et al. (2014), the model parameters are chosen equal to $d = 0.83\mathrm{Mm}$ $L = 1.25\mathrm{Mm}$, $R = 1.83\mathrm{Mm}$, $a = 0.75\mathrm{Mm}$, and $q = 10^{14}\mathrm{C}$, corresponding to a stable flux-rope configuration. For the meaning of these parameters, we refer to Section 2.4.1.2. The two models that we consider differ from each other in the way the current is distributed in the flux-rope. For Case I the flux rope has a parabolic current density profile, obtaining its maximal value at the center of the rope. For test Case II the current is localized in a thin layer at the outer boundary of the rope. For both test cases a computational box of size $[-3, 3] \times [-4, 4] \times [0, 4]$ with a resolution of 64^3 pixels is used. Moreover, for each test case we apply the optimization code once with the exact TD model imposed on all six boundaries, denoted by Case Ia and Case IIa, and once with the exact TD model only imposed on the lower boundary, denoted by Case Ib and Case IIb. For both Case I and Case II, we also apply the optimization code using the exact TD model field as initial field. This should produce a relaxed TD field, i.e., a TD model that has evolved towards a more force-free equilibrium.

The fields are extrapolated using weighting function w_f and w_d equal to unity. Only in Section 3.3.3, where the effect of using different weighting functions is tested, we use weighting functions that differ from unity. To quantify the performance of the optimization method we use the same metrics as we used for the LL test case in Section 3.2.

3.3.1 Test Case I: a Flux Rope with a Parabolic Current Distribution

The results of test Case I are illustrated in Fig 3.8. From this figure it is clear that the optimization method is able to reproduce a flux-rope configuration, starting from an initial potential field that has no flux-rope topology. The second row of Fig 3.8 shows a side view and a cross section along the magnetic flux-rope of the relaxed field. Comparing with the exact TD model, which is plotted in the first row of the figure, we see that the cross-section of the relaxed field has a more elongated shape. The elongated shape is actually what one expects in a force-free equilibrium, since the strength of the ambient bipolar field decreases with height. A consequence of this decreasing strength is that the upper part of the flux-rope feels less resistance against expansion than the lower part of the flux-rope. Remark that the side views of the flux-ropes of the exact model and the relaxed fields look similar, yet the relaxed field has a slightly broader current density distribution at the upper parts of the rope. Similar to the elongated shape, this can also be attributed to the decrease in strength of the ambient magnetic field. Titov et al. (2014) used the ideal MHD equations to relax the exact TD model to a force-free state. In doing so, the authors obtained a similar teardrop shape (see their Fig. 3). Based on a visual comparison, we can thus conclude that a relaxation using the optimization code and a relaxation using ideal MHD equations lead to similar results.

The last two rows of Fig 3.8 show that the flux-ropes of Cases Ia and Ib have a tear drop shape similar to the relaxed TD field. As already explained above, this is what can be expected since the exact TD model is not completely force-free. Remark that the cross sections of the reproduced fields are somewhat more compact than the cross sections of the relaxed field. Likewise, the side views reveal that the reconstructed flux-ropes lay somewhat lower than the relaxed flux-rope.

The first part of Table 3.6 gives the values for the different metrics with respect to the exact TD model. As expected, the values for Case Ia are slightly better than those of Case Ib. In addition, both cases perform much better than the potential field. This is not surprising since the potential field misses the flux-rope configuration. Moreover, remark that both Cases Ia and Ib have a CW $\sin\theta$ which is lower than the one of the exact TD model. This indicates that the current is better aligned with the magnetic field in the computed fields than in the exact TD model.

As already explained above, the extrapolated fields are expected to be more similar to the relaxed state of the TD model field. Therefore it is interesting to compute the metrics for the extrapolated fields with respect to the relaxed TD model instead of the exact TD model. These metrics are given in the second part of Table 3.6. We find that the values of the metrics with respect to the relaxed TD model are indeed

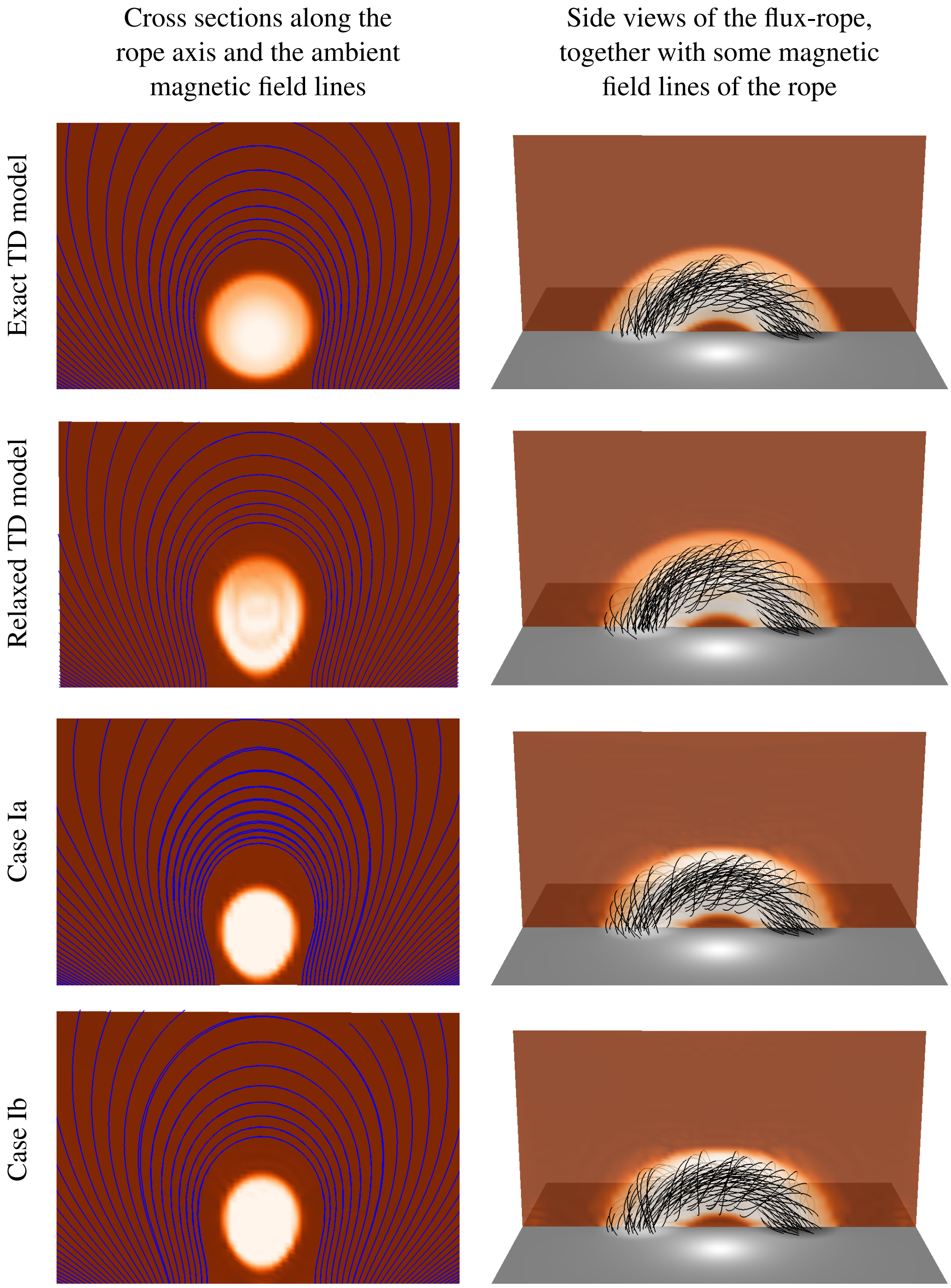

Figure 3.8: The grey scale is proportional to B_z, with white (black) corresponding to positive (negative) values of B_z. The orange colour-scale represents the magnitude of the current density. Both colour scales are in all the figures identical. The left column shows a cross section along the rope axis and the ambient magnetic field lines. The right column shows a side view of the flux-rope, together with some magnetic field lines of the rope. The first row is the exact TD model, the second row is the relaxed model, the third row is Case Ia, and the last row is Case Ib.

Model	C_{vec}	C_{CS}	E'_n	E'_m	ϵ	ϵ_p	$\text{CW}\sin\theta$
Metrics with respect to the exact TD model							
Exact TD model	1	1	1	1	1	2.05	0.11
Relaxed Field	0.99	1	0.91	0.94	1.06	2.19	0.05
Case Ia	0.99	1	0.94	0.95	1.04	2.13	0.05
Case Ib	0.99	0.99	0.87	0.77	0.97	2.00	0.16
Potential field	0.67	0.93	0.45	0.53	0.47	1.0	
Metrics with respect to the relaxed TD model							
Case Ia	0.99	1	0.95	0.97	0.97	2.13	
Case Ib	0.99	0.99	0.94	0.97	1.04	2.04	
Potential Field	0.67	0.95	0.49	0.69	0.51	1.0	

Table 3.6: Metrics for Case I.

all closer to one than the values of the metrics with respect to the exact TD model. As expected, the fields of Case Ia and Ib are thus more similar to the relaxed field than to the exact TD field.

3.3.2 Test Case II: a Flux Rope with a Hollow Current Distribution

The results of test Case II are illustrated in Fig 3.9. Like as for Case I, the relaxed and extrapolated fields show a much more elongated shape than the exact TD field. In addition, it can be seen from the side views that the relaxed and extrapolated flux-ropes are somewhat higher than the flux-rope of the exact TD model. These observations can again be attributed to the decreasing strength of the surrounding field. Furthermore, remark that the current density of the relaxed and extrapolated fields is broadened and concentrated near the bottom of the flux-rope. Despite this broadening, the side views in Fig 3.9 show that the magnetic field lines remain largely axial.

The values of the metrics are given in Table 3.7. The values of the metrics are slightly lower than those of Case I. This could already be expected since the cross-sections shown in in Fig 3.9 clearly deviate more from the model field than those in Fig 3.8. A possible explanation is that the exact field of Case II contains more force than the Case I field. This is reflected in a higher value of $\text{CW}\sin\theta$ for the Case II model field than for the Case I model field. As a consequence, the relaxed field of Case II will deviate more from the exact TD field than in Case I. Finally, remark that the metrics with respect to the relaxed field are very high for Case II. Even for Case IIb, where only the lower boundary is specified, the metrics deviate at most 0.06 from unity.

3.3.3 Effect of the Weighting Functions

In Section 3.2.4, we investigated the effect of the weighting functions w_f and w_d, using the LL field as test case. In this section we will do the same, but now using test Case Ib of the TD model.

The results are given in Table 3.8. Like for the LL equilibrium, we see that the lowest value of $\left(\frac{L_f}{w_f} + \frac{L_d}{w_d}\right)$ is obtained for $w_f = w_d = 1$. However, inspecting the metrics C_{vec}, C_{CS}, E'_n, E'_m and ϵ, it is seen that

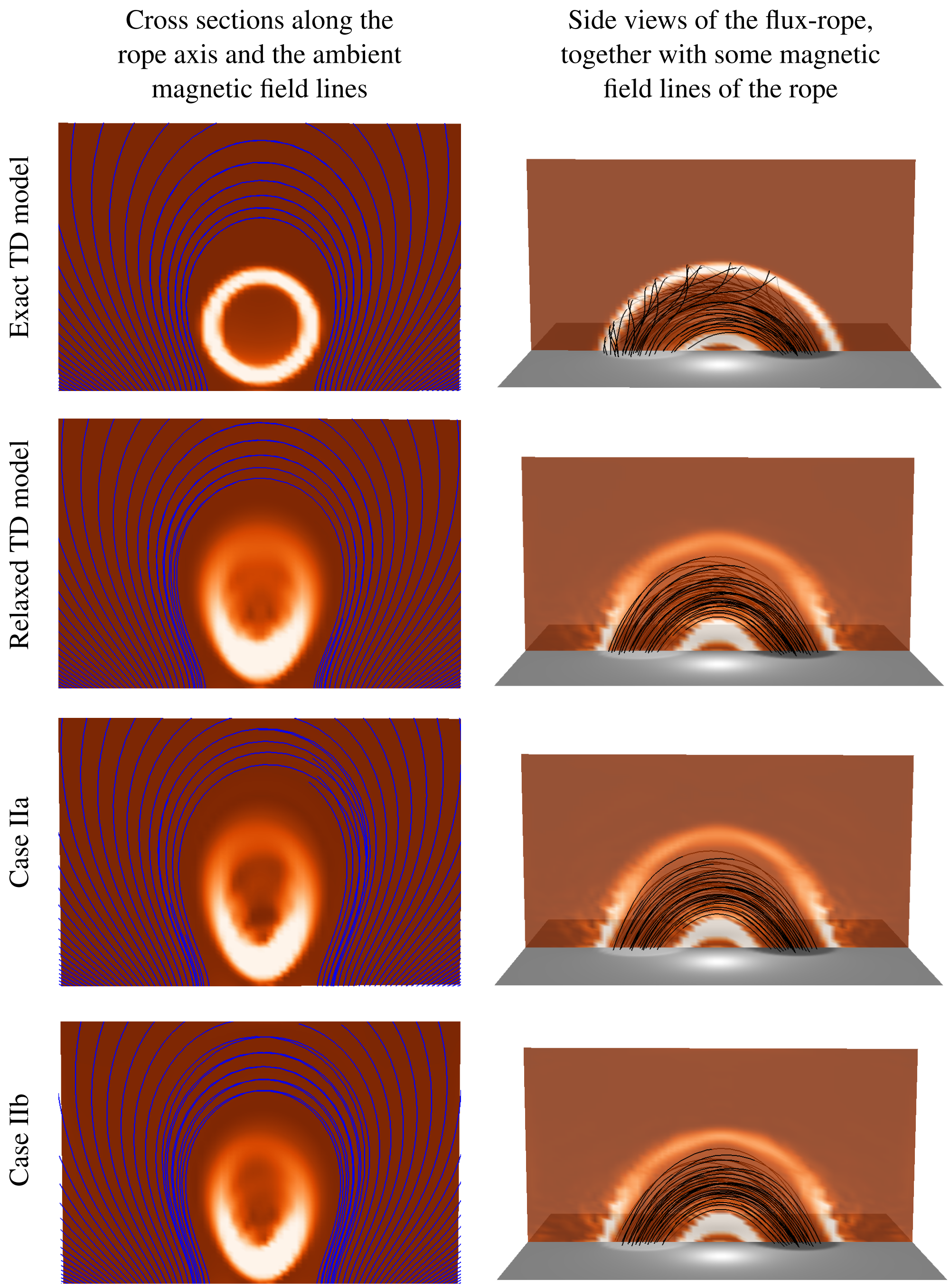

Figure 3.9: Analogous to Fig. 3.8 for Case II

Model	C_{vec}	C_{CS}	E'_n	E'_m	ϵ	ϵ_p	CW $\sin\theta$
Metrics with respect to the exact TD model							
Exact TD model	1	1	1	1	1	2.05	0.23
Relaxed Field	0.96	0.99	0.85	0.89	1.09	2.23	0.11
Case IIa	0.96	0.99	0.84	0.89	1.08	2.21	0.11
Case IIb	0.96	0.97	0.80	0.74	0.99	2.02	0.20
Potential field	0.67	0.90	0.40	0.46	0.49	1.0	
Metrics with respect to the relaxed TD model							
Case IIa	1	1	0.97	0.97	0.97	0.99	
Case IIb	0.99	0.98	0.86	0.74	0.91	2.02	
Potential Field	0.63	0.88	0.37	0.43	0.45	1	

Table 3.7: Metrics for Case II.

the best results are obtained for $w_f = 1$ and $w_d = 2$, although the differences are small. Remark that this is different from the LL test case (see Table 3.3), where the best metrics were obtained for $w_f = 1$ and $w_d = 0$. The force present in the exact TD field can explain why the TD test case attains its best metrics when $w_f < w_d$. By assigning a non-zero value to w_f, the optimization code will also try to minimize the force present in the exact model, such that the computed field will deviate more from the exact TD model. The difference with the LL test case illustrates that the optimal choice of weights depends on the specific magnetic field under consideration. However, in both cases we find that the results for $w_f = w_d = 1$ perform well.

3.4 Reconstruction of Active Region 10978

In previous sections we tested the performance of the optimization code using semi-analytical solutions of the force-free equations. In this section, we will go one step further and apply the optimization code to real solar data. We will use a vector magnetogram of NOAA[2] Active Region 10972 on 13 December 2007. This AR was scanned from 12:18 UT untill 13:41 UT by the Solar Optical Telescope Spectro-Polarimeter (SOT-SP) on board of the Hinode spacecraft. Less than three hours before this scan, at 09:39 UT, this AR produced a C4.5 flare. In addition, the AR produced a C1.0 flare less than one hour after the scan. In total, the National Geophysical Data centre GOES counted about 30 soft X-ray flares originating from this region. These flares indicate the presence of non-potential magnetic fields. This AR was selected because it was also used by DeRosa et al. (2015) to investigate nonlinear force-free extrapolation methods. This provides the opportunity to compare the results obtained by DeRosa et al. (2015) with our results.

Observations of the AR are shown in Fig. 3.10. As can be seen in panel (a), the AR is rather isolated and located close to the disk center, minimizing projection effects. The white boxes in panel (a) and (b) outline the scan area of Hinode/SOT-SP. It can be seen that most of the magnetic flux is situated inside this region. Remark however that it would be preferable to have a magnetogram encompassing an area larger than the AR. This would allow the non-potential magnetic field to be concentrated near the

---

[2] National Oceanic and Atmospheric Administration

w_f	w_d	C_{vec}	C_{CS}	E'_n	E'_m	ϵ	$\text{CW}\sin\theta$	$\frac{L_d}{w_d} \times 10^{-16}$	$\frac{L_f}{w_f} \times 10^{-16}$	$\left(\frac{L_f}{w_f} + \frac{L_d}{w_d}\right) \times 10^{-16}$
1	0	0.88	0.94	0.60	0.58	0.62	0.062	404	4.94	408.94
1	0.1	0.92	0.96	0.64	0.60	0.60	0.22	18	2.7	20.7
1	0.5	0.99	0.99	0.87	0.78	0.97	0.14	0.75	0.89	1.64
1	1	0.99	0.99	0.86	0.77	0.97	0.16	0.47	1.11	1.58
1	1.5	0.99	0.99	0.86	0.77	0.97	0.17	0.35	1.28	1.63
1	2	0.99	0.99	0.88	0.79	1.0	0.18	0.28	1.31	1.59
1	10	0.98	0.98	0.83	0.77	0.93	0.24	0.16	3.57	3.73

Table 3.8: Metrics for the TD model, using different weights.

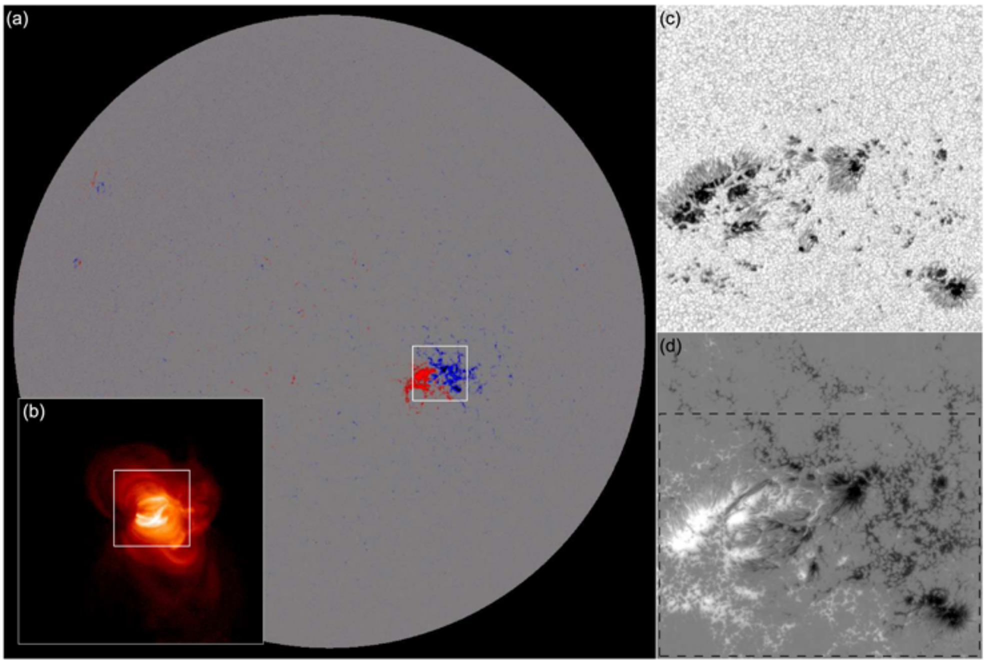

Figure 3.10: (a) SOHO/MDI full-disk magnetogram of Active Region 10972 on 13 December 2007 at 12:46 UT. (b) Hinode/XRT images of the AR, using a logarithmic scaling. (c) Continuum intensity measured by Hinode/SOT of the region outlined by the white box in panels (a) and (b). (c) Longitudinal magnetic field obtained from the Hinode/SOT polarization spectra. Figure from DeRosa et al. (2015).

center of the box, such that the field near the boundaries is close to potential. The optimization method would greatly benefit from such measurements since the method keeps the side and top boundaries of the computational box fixed and equal to the potential field. Remark that keeping a potential field fixed on the side and top boundaries means that the optimization method does not allow any current to leave the computational volume, except at the bottom boundary. An additional drawback is that not many loops can be clearly distinguished on the image taken by the X-Ray Telescope (XRT) on board of Hinode (see panel (b) of Fig 3.10). This makes it difficult to estimate the goodness of the extrapolated magnetic field.

The SOT-SP has a field of view of about $164'' \times 164''$, which is sampled over 1024^2 pixels. Each pixel correspond thus with a $0.16'' \times 0.16''$ region. The entire region corresponds to an area of about 168×10^{12} m^2. Performing a nonlinear extrapolation method using a computational box of about $\sim 1024^3$ pixels is a challenge, even for modern computers. Using a grid of size $\sim 1024^3$, where each grid point contains a three-dimensional vector of single-precision floating-point numbers, requires about 12GiB of byte-addressable computer memory. Most extrapolation methods require the simultaneous storage of several of these four-dimensional arrays, resulting in memory problems on most computers. A second problem is the time needed for the computations. If N^3 denotes the number of grid points, then a run of an extrapolation method takes a time that scales in the best case as N^4 (Wheatland 2007).

Here we circumvent these memory and time problems by using a magnetogram that is calculated from a polarization spectra rebinned by a factor of six in each dimension. Following DeRosa et al. (2015), we additionally neglect the northernmost 25% of the SOT field of view. The effect of using rebinned data on the nonlinear force-free extrapolation methods was investigated by DeRosa et al. (2015). They found that the large-scale magnetic and current density structures are retained in the lower resolution data, yet the structures on scales comparable or equal to the resolution limit are lost. In addition, it was found that when the extrapolation methods are applied on high resolution data, they provide magnetic fields that are more force-free and divergence-free.

3.4.1 Metrics

The performance of the optimization code, can no longer be quantified using the metrics introduced in Section 3.2.1. The reason is that these metrics require knowledge about the exact magnetic field. Only the metrics CW $\sin\theta$ and ϵ_p do not require the true magnetic field and can thus still be used. Here we introduce some additional metrics that are often used to evaluate the computed magnetic field. The first one was introduced in Malanushenko et al. (2014) and is given by

$$\xi = \frac{1}{N} \sum_i \frac{|\mathbf{F}_\mathrm{L}|_i}{|\mathbf{F}_\mathrm{mp}|_i + |\mathbf{F}_\mathrm{mt}|_i}, \tag{3.7}$$

where $\sum_i$ denotes a summation over all pixels, N the total number of points, $\mathbf{F}_\mathrm{L}$ the Lorentz force, $\mathbf{F}_\mathrm{mp}$ the magnetic pressure force, i.e., $-\frac{1}{2\mu_0}\nabla_\perp B^2$, and $\mathbf{F}_\mathrm{mt}$ the magnetic tension force, i.e., $\frac{1}{\mu_0}B^2\frac{d\hat{\boldsymbol{b}}}{db}$, with $\mathbf{B} = B\hat{\boldsymbol{b}}$ and b the distance along the magnetic field. Since $\mathbf{F}_\mathrm{L} = \mathbf{F}_\mathrm{mt} + \mathbf{F}_\mathrm{mp}$, we have that $0 \leq \xi \leq 1$. Like CW $\sin\theta$, the measure ξ is used for estimating how force-free a magnetic field is. If $\xi \approx 1$, the magnetic field contains substantial Lorentz-force, whereas a vanishing ξ corresponds to a force-free configuration.

Next, we introduce a metric that measures the divergence of the magnetic field. It was first used by Wheatland et al. (2000) and is defined as

$$\langle |f| \rangle = \frac{1}{N} \sum_i \frac{|(\nabla \cdot \mathbf{B})_i| \Delta x}{6|\mathbf{B}|_i}, \tag{3.8}$$

where Δx is the grid spacing. For a perfectly divergence-free magnetic field, the metric $\langle|f|\rangle$ is equal to zero.

Finally, we introduce two metrics that probe the force-freeness of the magnetic field as a function of height. The first metric provides for each height z the average angle between the magnetic field and the current density, .i.e.,

$$\langle\theta\rangle(z) = \frac{1}{N}\sum_p \arcsin\left(\frac{|\mathbf{j}_p \times \mathbf{b}_p|}{|\mathbf{j}_p||\mathbf{b}_p|}\right), \tag{3.9}$$

where $\sum_p$ denotes a summation over all pixels at height z, and N is the total number of pixels at height z. The second metric provides for each height z a current weighted average angle between the magnetic field and the current density.i.e.,

$$\langle\theta_J\rangle(z) = \arcsin\left(\frac{\sum_p |\mathbf{j}_p||\sin\theta_p|}{\sum_p |\mathbf{j}_p|}\right), \tag{3.10}$$

where

$$|\sin\theta_p| = \frac{|\mathbf{j}_p \times \mathbf{b}_i|}{|\mathbf{j}_p||\mathbf{b}_p|}. \tag{3.11}$$

Remark that this metric is similar to the CW $\sin\theta$ introduced in Eq. (3.5). For a perfect force-free field, both $\langle\theta\rangle(z)$ and $\langle\theta_J\rangle(z)$ become zero at all heights z.

3.4.2 Results

Since the vector magnetogram is not completely force-free, we will run two different tests. For test Case I, we apply the optimization method to the original vector magnetogram. For test Case II we first preprocess the magnetogram, using parameters $\mu_1 = \mu_2 = 1$, $\mu_3 = 10^{-4}$ and $\mu_4 = 1$, and subsequently apply the optimization method. For details about the preprocessing method we refer to Section 2.5.1. In addition, the test cases are further extended by performing the optimization code several times, where each run uses different weights w_f and w_d.

The computed magnetic fields are shown in the first row of Fig. 3.11. Remark that, in contrast to the semi-analytical fields discussed in the previous sections, we obviously do not have the exact magnetic field to check our solution with. The second row of Fig. 3.11 gives a contour map of the force-free parameter α. It can be seen that α is highly variable, switching sign in several regions. This illustrates that a linear force-free field would probably be a poor approximation of the exact magnetic field. The last row of Fig. 3.11 shows the magnitude of the total current density, integrated vertically through the computational box. These figures show that the AR contains some strong localized current densities, and hence illustrate the necessity of nonlinear force-free extrapolations. In addition, the figures reveal that there are strong current densities located close to the side boundaries of the computational volume. This suggests that there may exist current flows across the boundaries of the computational domain. However, since the optimization code does not allow any currents to leave, these current flows are not treated well. therefore, one should question the correctness of the obtained current distribution.

To compare our results with the results of DeRosa et al. (2015), we plot in the left column of Fig. 3.12 the magnetic fields obtained by DeRosa et al. (2015), using four different extrapolation methods. These methods include an optimization method, a magnetofrictional method and two different implementations of the Grad-Rubin method. For the Grad-Rubin methods, DeRosa et al. (2015) used the XTRAPOL and the FEMQ codes (see Section 2.4.2.3). For details about the numerical implementations of the different methods, we refer to DeRosa et al. (2015) and reference therein. The extrapolated fields in the left column of Fig. 3.12, reveal that there are some differences between the magnetic fields obtained with the different extrapolation methods. The overall topology of the fields is however similar. Moreover, remark that the magnetic fields obtained with our implementation of the optimization method (see first row of Fig. 3.11) have a similar morphology.

For additional comparison, we computed for each field of DeRosa et al. (2015) the total current density, integrated vertically through the models. These integrated current distributions are shown in the right column of Fig. 3.12. They reveal that there are some major differences between the various extrapolation methods. In particular, the fields calculated with the Grad-Rubin methods contain significantly less current than the fields calculated with the optimization method and the magnetofrictional method. Remark that, although the magnitudes of the currents strongly differ, the overall shape of the different current densities shows resemblance.

The integrated current density of our Case I field (see Fig. 3.11) shows most resemblance with the integrated current density of the magnetofrictional method, shown in the second row two of Fig. 3.12. In contrast, the integrated current density of our Case II field shows clear resemblance with the integrated current density shown in the first row of Fig. 3.12. This is not surprising, since this current density was also obtained from an optimization approach that uses a preprocessed magnetogram. Remark however that the currents of our Case II field are, at most locations, slightly weaker than the currents obtained from the optimization method of DeRosa et al. (2015). Recall from Section 3.1 that our optimization code splits the magnetic field into a potential and non-potential part, to allow for a more accurate computation of the non-potential part. Since the optimization method used by DeRosa et al. (2015) does not perform such a splitting, one can speculate that this causes, at least partly, the observed differences between the results of the two optimization codes.

Table 3.9 provides the values of the different metrics for our Case I and II fields. The table also gives the total energy E and the energy relative to the potential field energy, ϵ_p (see Eq. (3.4)). Remark that $\epsilon_p < 1$ for the magnetic field of Case I with $w_d = w_f = 1$. At first, this may seem to violate the potential minimum-energy theorem introduced in Section 2.2.1. However, this theorem only applies for perfectly solenoidal magnetic fields. Therefore, if the computed field contains a non-vanishing divergence, the minimum energy theorem can be violated. The fact that ϵ_p is smaller than unity, indicates thus that the optimization method did not succeed to minimize divergence sufficiently. This is also reflected in the relatively high value of the metric f. By increasing the weight w_d of the divergence term in Eq. (2.40), the computed field will become more divergence-free, and is therefore more likely to satisfy the potential minimum-energy theorem. Inspecting the metrics of Case I with $w_d = 5$ and $w_f = 1$, reveals that for this test case the potential energy is indeed smaller than energy of the computed field, i.e., $\epsilon_p > 1$. Remark that the energy of the computed field is still only 2.4% higher than the potential field energy. However, the observations of numerous flares originating from the AR suggest significant deviations from the a potential field configuration. In addition, remark that the extrapolated fields of Case I have a relatively large metric $\mathrm{CW}\sin\theta$. By taking the inverse sine of $\mathrm{CW}\sin\theta$, we obtain an angle of $\sim 30°$, which shows that the currents and the magnetic fields are not well aligned. It can thus be concluded that the reconstructed field of Case I is a rather poor approximations of the real solar field.

In contrast, in Case II all extrapolations have an ϵ_p significantly larger than one. Comparing the different fields of Case II we see that the minimum $\left(\frac{L_f}{w_f} + \frac{L_d}{w_d}\right)$ is obtained when $w_d = w_f = 1$. This is in agreement with the results of Sections 3.2.4 and 3.3.3. We remark that our Case II fields have a total energy content of 1.32×10^{26}J, whereas the field computed by DeRosa et al. (2015) with the optimization method has a total energy of 1.43×10^{26}J. In contrast, the fields computed by DeRosa et al. (2015) with the Grad-Rubin methods have an energy content of $\sim 1.27 \times 10^{26}$J. Solely based on the energetics, we can thus say that our Case II fields are more similar to the fields computed by DeRosa et al. (2015) with the Grad-Rubin method than with optimization method. This may be a consequence of the splitting of the magnetic field in a potential and non-potential part in our implementation of the optimization code.

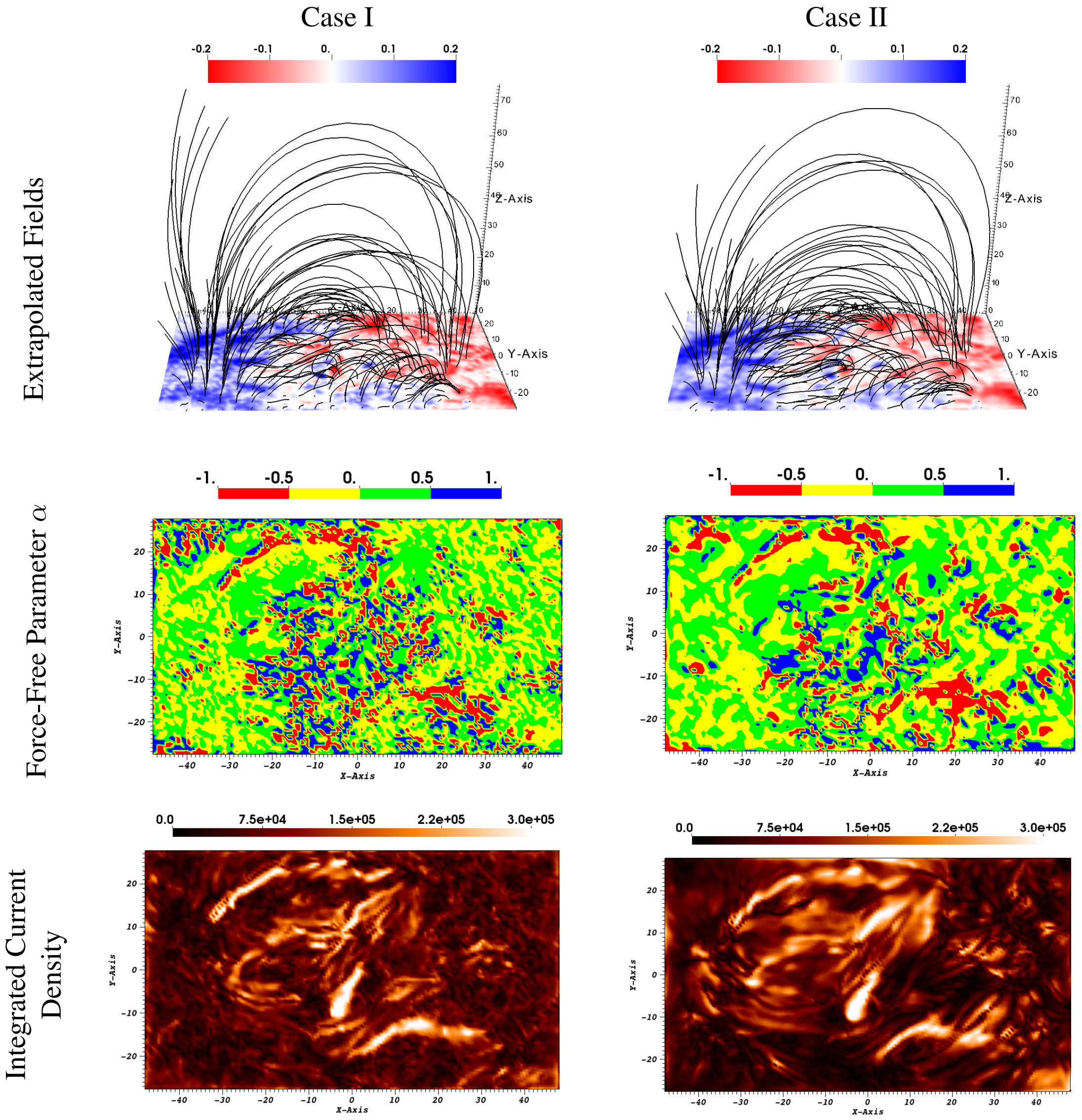

Figure 3.11: The first row shows the computed magnetic field lines. The blue-red colour scale gives B_z in tesla. The second row gives α (m^{-1}). The last row gives the vertically integrateded magnitude of the current density, in $\mathrm{A/Mm}$. The x, y and z axis are in Mm.

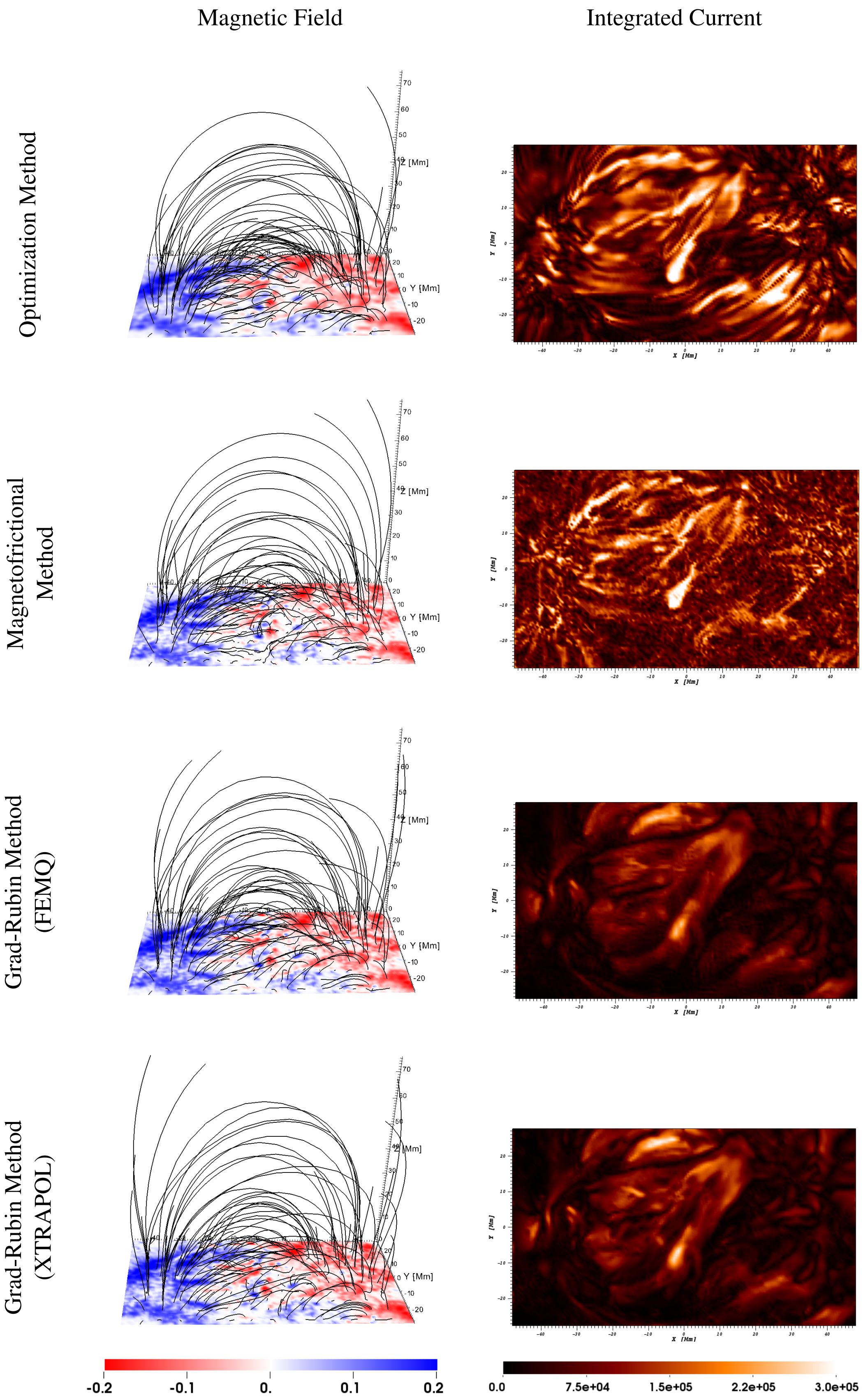

Figure 3.12: The left column shows the magnetic fields obtained in DeRosa et al. (2015), using the extrapolation methods indicated at the left side of the figures. The blue-red colour scale gives B_z in T. The right column shows the vertically integrateded magnitude of the current density, in $\mathrm{A/Mm}$. The colour scale are identical to the ones used in Fig. 3.11.

w_f	w_d	$E[10^{26}\text{J}]$	ϵ_p	$\text{CW}\sin\theta$	$\langle\lvert f\rvert\rangle \times 10^8$	ξ	$\frac{L_d}{w_d} \times 10^{-12}$	$\frac{L_f}{w_f} \times 10^{-12}$	$\left(\frac{L_f}{w_f} + \frac{L_d}{w_d}\right) \times 10^{-12}$
Case I									
1	1	1.043	0.93	0.49	4.8	0.091	3.93	3.04	6.97
1	5	1.127	1.024	0.5	3.13	0.19	3.61	3.40	7.01
Case II									
1	0.1	1.32	1.20	0.24	4.6	0.24	2.5	0.8	3.3
1	0.5	1.33	1.21	0.21	2.8	0.15	1.6	0.94	2.54
1	1	1.32	1.20	0.23	2.3	0.13	1.4	1.0	2.4
1	1.5	1.32	1.19	0.25	2.2	0.14	1.3	1.16	2.46
1	2	1.32	1.19	0.23	2.1	0.14	1.3	1.2	2.5

Table 3.9: Metrics calculated for extrapolations of AR 10978.

Remark that the computed magnetic fields of our Case II all have a magnetic energy content that is about 20% larger than the energy of the potential field. This may be a fairly good estimate of the relative energy content of the true magnetic field. However, considering all uncertainties concerning the boundary data, the true magnetic energy may still deviate significantly from the obtained 20%.

Figure 3.13 shows the average angles $\langle\theta\rangle$ and $\langle\theta_J\rangle$ (see Eqs. (3.9) and (3.10)) for Case II. The figure reveals that the magnetic field and the current density are considerably better aligned at low altitudes than at high altitudes. This illustrates that the performance of the optimization code strongly depends on the strength of the magnetic field and current density. For regions with a weak magnetic field and current density, the optimization code produces a magnetic field that is much less aligned with the current density than for regions with a strong magnetic field and current density. A similar result was obtained when discussing the Low&Lou models in Section 3.2.3. Moreover, this also explains why $\langle\theta\rangle$ is everywhere larger than $\langle\theta_J\rangle$, since the latter gives more weight to regions with stronger currents and magnetic field.

Better results would be obtained if we would have a larger vector magnetogram, such that the entire magnetic flux of the AR is covered. As already mentioned above, the magnetic field at the boundaries of a magnetogram covering the whole AR will be more potential, which is beneficial for the performance of the optimization method. This was illustrated in Section 3.2 by calculating the metrics of the computed LL equilibria for the whole domain and for an inner box. However, there are no larger vector magnetograms available that cover the AR, yet there are line-of-sight magnetograms covering the whole Sun. One could thus extend the vector magnetogram by using these line-of-sight magnetograms. In these extended zones one can choose the horizontal magnetic components equal to the horizontal magnetic components of either the potential field or a linear force-free field. By extending the boundary data in this way, one moves the boundaries of the computational box further away from the AR of interest, which increases the performance of the optimization method. The drawback is that one has to assume a horizontal magnetic component, which will reduce the performance of the optimization method. Whether the net result of such an extension will improve the results has to the best of my knowledge not yet been investigated. Remark that such an approach is only relevant when one wants to study ARs from before 2010. For ARs that appeared on the Sun later than 2010, one can use vector magnetograms of the complete solar disk measured by the Helioseismic and Magnetic Imager (HMI) on board the Solar Dynamic Observatory (SDO).

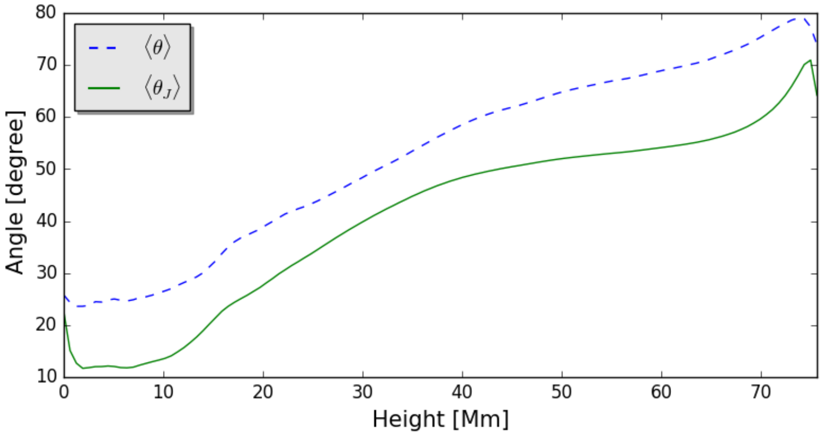

Figure 3.13: The blue dashed curve shows the average angle betweent the magnetic field and the current as a function of height. The solid green curve show the average current weighted angle as a function of height.

3.5 Summary and Conclusions

In this chapter, we tested an implementation of the optimization approach. This was done with the help of semi-analytical reference fields and real solar measurements. For the test cases using the semi-analytical fields, the performance of the method was determined qualitatively, by comparing the magnetic field lines with the exact model, and quantitatively, by using different metrics that measure the agreement between the extrapolated and model field.

We used two different Low&Lou (LL) fields to test the performance of the optimization code. For both cases, the extrapolated fields agree relatively well with the exact LL model fields. The results were even better when considering a smaller box, centred in the full computational domain. For test Case I, this increase in performance could solely be attributed to the remoteness of the boundaries of the computational box. For test Case II, we noted that the reason for the increase of performance in the smaller box was twofold. One reason was, like for the first LL field, the remoteness of the boundary conditions. The other reason is that the optimization code seems to perform best in regions where the magnetic field and the currents are strong.

One should be careful when drawing conclusions from the good results obtained when using the LL fields as test cases. Whereas these results are definitely encouraging, one can argue that the LL fields may not be the most challenging tests for the optimization method. The LL fields are very smooth, and their magnetic field topology is similar to the potential field computed from the lower boundary. Therefore it should not be surprising that the optimization code delivers good results. On the other hand, a code that does not succeed with the LL model will probably also not work well for real solar data.

The TD test cases illustrated that the optimization method is able to reconstruct a flux-rope topology, starting from a potential field that does not contain any flux-rope. Although the metrics of the extrapolated fields are relatively high, we noted that there are some clear differences in Fig. 3.8 and Fig. 3.9 between the model field and the computed fields. However, these differences are probably mostly caused by the fact that the TD model fields are not perfectly force-free. In addition, the way the current is distributed also seems to affect the optimization code, since the first TD test case delivered higher values for the metrics than the second TD test case. This can be attributed to the fact that the first TD model is more force-free than the second one.

We remark that for both the LL fields and the TD fields, the optimization code accurately reproduces the ratio of the total energy over the potential energy. This is important since it allows to determine the free energy, which is the energy that drives eruptive events in the solar corona.

The effect of using different weighting functions in Eq. (2.40) was tested for both the LL and the TD test cases. For both test cases, we obtained a different choice for the optimal weighting functions. The LL test case benefited most from giving a larger weight to the force component of Eq. (2.40). In contrast, the TD test case gave the best results when the divergence term of Eq. (2.40) was weighted more. This illustrates that the optimal choice of the weighting functions is dependent on the specific magnetic field under consideration. This makes it difficult to obtain an optimal choice of weighting functions for real solar data, in which case the exact field is unknown. Remark however that for both the LL and TD test cases, an equal weight for the divergence and the force term in Eq. (2.40) led to results that were close to the optimal. This suggests that it is safe to use equal weights when applying the optimization code to real solar data.

The extrapolation of a magnetogram of AR 10978 illustrated that preprocessing the magnetogram may significantly alter the results. This is due to the fact that the photospheric environment is not a force-free regime. Using the original magnetogram, we found that the ratio of the energies of the extrapolated field and the potential field was smaller than one. This is in contradiction with the potential minimum energy theorem, stating that a potential field is the magnetic field configuration with the lowest energy. This contradiction can be attributed to the presence of a substantial amount of divergence in the extrapolated field. When using a larger value for weight w_d, we obtained that the divergence is minimized enough to satisfy the potential minimum energy theorem. Moreover, the extrapolation using a preprocessed field gave also an energy ratio larger than one, i.e., a ratio that is physically possible. However, since the preprocessing method makes many approximations, it is questionable whether this energy ratio is close to the true value.

Like for the analytical test cases, we found that the performance of the optimization method strongly worsen with increasing altitude. This is probably due to the weak magnetic field and electric currents in these regions. To check whether the extrapolated field is a good reproduction of the exact solar magnetic field, it would be interesting to have coronal images that can be used to identify several coronal loops. The importance of a comparison between observations and the computed field has been stressed in many studies (see, e.g., Schrijver et al. 2008; De Rosa et al. 2009; DeRosa et al. 2015).

Chapter 4

Evolution of a Solar Active Region

The coronal magnetic field is the driving force behind extreme solar activity, which mostly originates from solar active regions (ARs). As discussed in Section 1.2.3.2, ARs are characterised by a strong and highly dynamic magnetic field. In these regions, substantial flux emergence, shearing motions and reconnection processes often cause the magnetic field to deviate strongly from a potential magnetic field. Eventually, the magnetic field may become unstable, leading to transient eruptive events like coronal mass ejections (CMEs) and flares. The energy driving these eruptions originates from the available free magnetic energy, such that the magnetic field after the eruption is reconfigured to a more potential state. It is believed that the topology of the magnetic field almost solely determines whether a CME and/or a flare occurs. Therefore, knowledge about the AR magnetic field and its evolution is of utmost importance if one wants to understand solar activity.

The magnetic field of ARs can be studied using nonlinear force-free extrapolation methods, like the ones discussed in Section 2.4.2. Such methods have already been applied to several ARs with varying success (see, e.g., Thalmann & Wiegelmann 2008; Schrijver et al. 2008; De Rosa et al. 2009; Sun et al. 2012; DeRosa et al. 2015). These attempts have illustrated that the different methods often produce results that differ from each other in many aspects. Most of these differences are believed to be a consequence of the different treatments of the boundary conditions in these methods. These boundary conditions are derived from photospheric magnetic field measurements, and, as discussed in Section 2.5.1, they are subject to many uncertainties. These uncertainties not only include measurement noise, but also the non-force-free nature of the photospheric magnetic field. The inconsistencies between the various models show the importance of metrics that are able to quantify the similarities and differences between the extrapolated fields and the real solar magnetic field. In addition, extreme ultraviolet images (EUV) can be used to compare the extrapolated field and EUV outlined loop trajectories of the AR. If the topology of the extrapolated magnetic fields corresponds well with those loops, and if the extrapolated field is in addition consistent with both the force-free and divergence-free conditions, the field can be used to probe physical quantities of the AR. Examples include connectivities, current densities, magnetic energy, and helicity.

Recall that the currently existing extrapolation methods assume a quasi-static configuration, i.e., plasma flows are neglected. As discussed in the beginning of Chapter 2, this approximation is justified by considering that for a coronal structure of length scale ~ 100 Mm, the characteristic Alfvén transit time is only a few minutes. Therefore, the evolution of the magnetic field of ARs be studied by using a series of successive static extrapolations. By comparing an extrapolation made just before a CME or flare with an extrapolation directly after, one can hope to obtain knowledge about the actual event. For example, changes in the magnetic topology may indicate the occurrence of magnetic reconnection processes. Apart from that, one can try to deduce the energetics of the CME or flare by looking for changes in the free

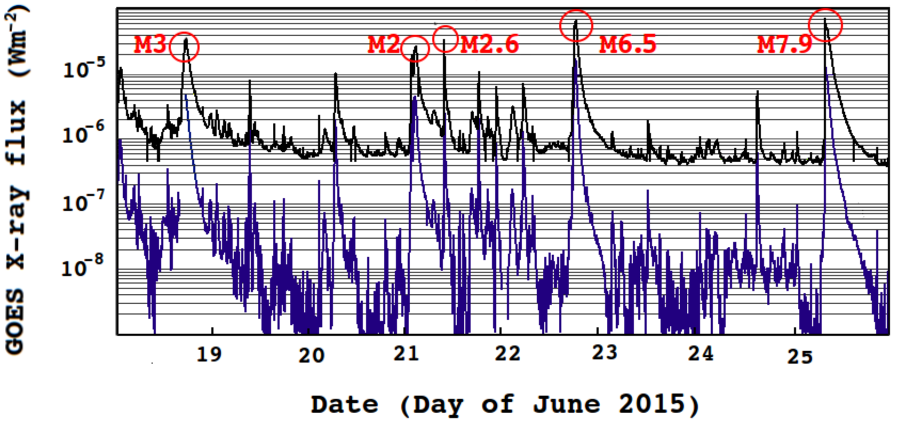

Figure 4.1: Time profile of the X-ray flux measured by the GOES satellite from 18 June to 25 June 2015. The black curve corresponds to the 1–8 Å bandpass and the blue curve corresponds to the 0.5–4.0 Å bandpass. The M-class flares discussed in the text are indicated with red circles.

energy of the magnetic field. In principle, all of this is possible, but whether it is in practice possible with current existing methods is not clear and is part the topic of this chapter.

In this chapter, we use the optimization method to investigate the evolution of the magnetic field of NOAA AR 12371 during a period of seven days, from 19 June 2015 to 25 June 2015 . As detailed in Section 4.1, the AR showed significant activity during this time period. The extrapolations are performed using a series of vector magnetograms from the Helioseismic and Magnetic Imager (HMI) on board the Solar Dynamic Observatory (SDO). To study the evolution of the AR, a sequence of magnetograms spaced six hours apart in time were chosen. Section 4.2 describes the preparation of the series of vector magnetograms, and discusses the observed properties of the magnetic field. Next, in Section 4.3, we discuss the extrapolated fields, including an analysis of the force-freeness and divergence-freeness of the fields (Section 4.3.1), and we use EUV images taken by the Atmospheric Imaging Assembly (AIA) on board SDO to compare the extrapolated field with observed loops. Sections 4.3.2 and 4.3.3 study the evolution of the morphology of the magnetic field of the AR, while in Section 4.4, the energy distribution of the magnetic field is discussed. A summary and conclusions are provided in Section 4.6.

4.1 Observations of AR 12371

AR 12371 first appeared on the East limb of the Sun on 16 June 2015. Eleven days later, on 27 June, the AR reached the West limb and moved out of our field of view. The left column of Fig. 4.2 illustrates the location of the AR on the solar limb. Shown are magnetograms of the full solar disk on 19, 22, and 25 June. The AR is indicated with a red box.

Several flares and CMEs originated from the AR 12371 between 18 June and 25 June. The CMEs described in the following were identified using the CACTUS catalogue (Robbrecht et al. 2009), whereas the flares were identified using the Hinode Flare Catalog[1], which is maintained by ISAS/JAXA and Solar-Terrestrial Environment Laboratory, Nagoya University. Figure 4.1 shows the X-ray flux measured by the GOES satellite from 18–25 June, 2015. Indicated on this figure are five M-class flares which are discussed in the following.

---

[1] `http://st4a.stelab.nagoya-u.ac.jp/hinode_flare/`

On 18 June a first CME occured at 17:36 UT, and was accompanied by an M3.0 class flare. This flare was visible as a two-ribbon flare on 171 Å images taken by AIA. The CME was observed as a halo-CME by the Large Angle and Spectrometric Coronagraph (LASCO) on board Solar and Heliospheric Observatory (SOHO).

On 21 June, an M2.0 class flare and an M2.6 class flare were observed at 01:02 UT and 02:06 UT, respectively. Shortly after these flares, at 02:36 UT, another halo CME erupted from AR 12371. Some hours later, at 09:45 UT and 18:20UT, two other flares, i.e., an M3.8 and an M1.1 class flare were observed. These four flares are all clearly visible in SDO AIA 171 Å, 193 Å, and 131 Å (see also panel (a) of Fig. 4.7). During these events, the AR was located close to the disk center. When the CME reached Earth on 22 July at 18:00 UT, it caused a huge magnetic storm.

A third halo CME erupted from AR 12371 on 22 June at 18:36UT. This CME was associated with a bright M6.5 class flare. The brightening of the flare is clearly visible in the EUV imagery of AIA 193 Å, 171 Å, 211 Å, 304 Å and 131 Å (see panel (b) of Fig 4.7). The flares and CME caused a significant solar energetic particle event at Earth and, when the CME reached Earth on 24 June at 13:00 UT, it caused a relatively short geomagnetic storm.

A fourth CME originated from AR 12371 on 25 June, at 08:48 UT. At this time the AR was approaching the West solar limb and as a consequence the CME was observed as a partial halo CME by LASCO. This CME was associated with a bright M7.9 class flare (see panel (c) of Fig 4.7). The flare is again clearly visible in the AIA imagery, at the wavelengths 193 Å, 171 Å, 211 Å, 304 Å, and 131 Å, and occurred less than 30 minutes before the CME that erupted at 08:48 UT.

4.2 Vector Magnetogram Data for AR 12371

The magnetograms that we use as boundary data for our extrapolations are measured by the HMI instrument on board SDO. This instrument measures the photospheric magnetic field of the full solar disk, by using six polarizations states of the Fe I absorption line at 6137 Å . Line-of-sight magnetograms are available with a cadence of 45s, whereas full-disk vector magnetograms are provided every 720s (twelve minutes). The vector magnetograms are obtained by inverting the IQUV Stokes parameters, assuming a Milne-Eddington atmosphere when solving the radiative transport equations. This is done by using the Very Fast Inversion of the Stokes Vector code as described by Borrero et al. (2011).

An area encompassing NOAA AR 12371 is selected from the full-disk vector magnetograms. The enclosement is tracked according to the rotation of the Sun so that the AR remains well within the window during it's evolution across the disk. The vector magnetic field is then projected to a local Cartesian system with the origin at the center of the window using a Cylindrical Equal Area projection. A final step in constructing the magnetogram sequence is to perform a temporal regularization of the magnetograms similar to Welsch et al. (2013). This is done in order to remove spurious flips of the horizontal field that arise as a result of errors inherent in the disambiguation procedure when applied to separate magnetograms. This step greatly enhances the temporal quality of the data set. Note that this temporal regularisation is performed using the full-cadence data-set of HMI.

In strong field regions, the 180° azimuth ambiguity is resolved with the Minimum Energy code (see Leka et al. (2009) for details), whereas in in weak field regions, the 180° azimuth ambiguity is resolved with the potential field acute angle method (see Hoeksema et al. (2014) for details).

The HMI instrument has an optical resolution of $0.91''$ and a pixels size of $0.5''$. For our computations, we bin the data to about $2''$ pixel^{-1}, and adopt a computational domain of $300 \times 170 \times 150\ \mathrm{Mm}^3$, corresponding to a grid of $191 \times 126 \times 102$ pixels. We preprocess the magnetograms to obtain chromospheric force-free magnetograms (see Section 2.5.1). This is done assuming that the chromosphere is at a height

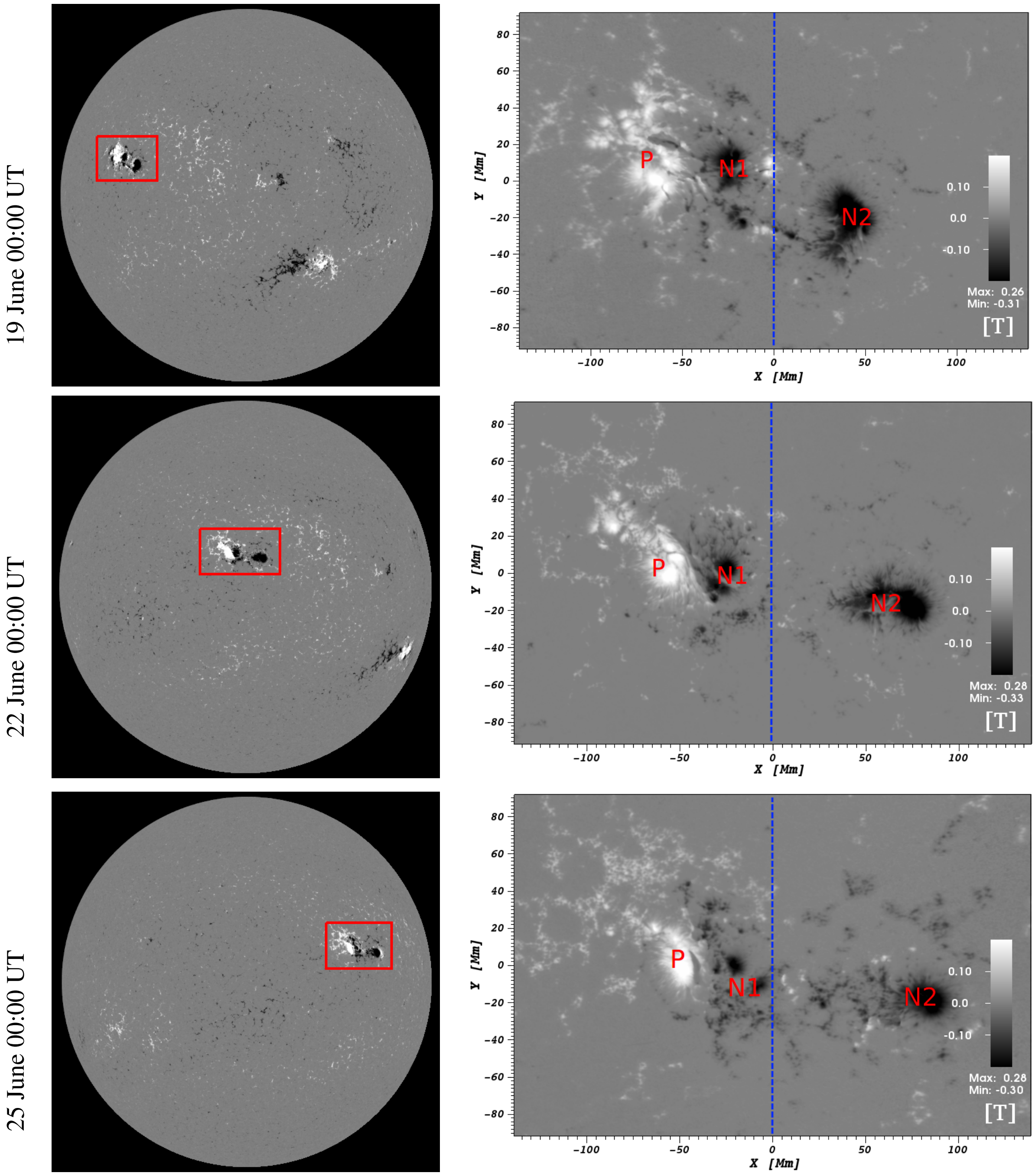

Figure 4.2: Line of sight component of the HMI vector magnetograms on 19 June 2015 at 00:00 UT, 22 June 2015 at 00:00 UT, and 25 June 2015 at 06:00 UT respectively. The red box indicated the location of AR 12371.

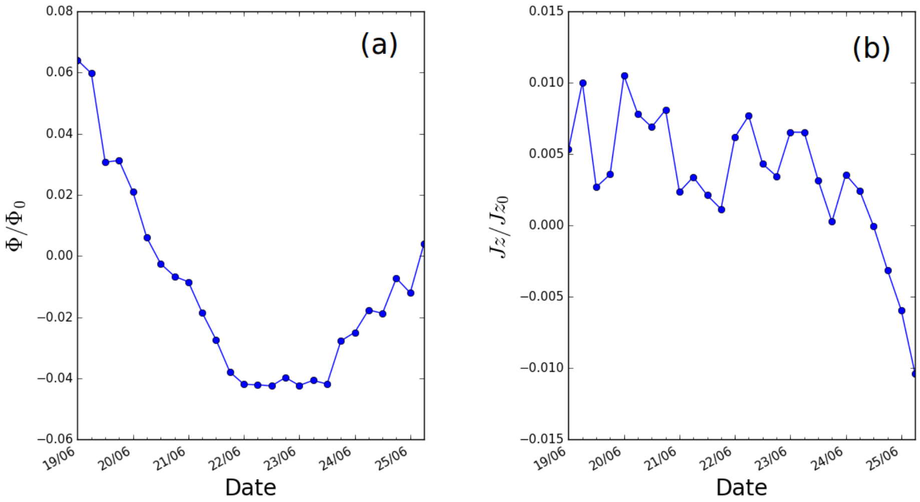

Figure 4.3: (a) Ratio of the net to the unsigned flux. (b) Ratio of the net to the unsigned current.

of 400 km above the photosphere, and by using the preprocessing parameters $\mu_1 = \mu_2 = \mu_4 = 1$ and $\mu_3 = 10^{-4}$.

In total, 26 magnetograms of NOAA AR 12371 are considered, with a cadence of 6 hours. The first magnetogram corresponds to 19 June 2015 at 00:00 UT, and the last magnetogram corresponds to 25 June 2015 at 06:00 UT. During this time period, AR 12371 rotates from the East limb to the West limb of the Sun, while remaining at locations sufficiently far from the limb (see Fig 4.2). This is necessary because close to the limb the quality of the magnetogram data quickly degrades. This is because the AR is viewed at a considerable angle, leading to a substantial loss in resolution. The right column of Fig. 4.2 gives three snapshots of the vertical magnetic field in the domain used to perform our extrapolations. When studying the evolution of the AR, we will often consider the right and the left side of the magnetograms separately, for convenience of exposition. This is indicated by the blue dashed line in Fig 4.2. Remark that, since the rotation of the Sun is removed from the magnetograms, the separation between left and right is well defined as a function of time. The reason to look at both sides separately is because most of the EUV activity occurs on the left part of the AR. In addition, it allows us to investigate the evolution and interaction between both parts more closely. Figure 4.2 reveals that the AR consists of three major magnetic polarity regions. At the left side, there is a major region with a positive magnetic polarity. This region is indicated with the letter P. In the middle and at the right side of the AR, there are two major regions with negative polarity, denoted by N1 and N2, respectively.

The left column of Fig. 4.2 shows that AR 12371 is largely isolated from other ARs, such that it is expected to be flux-balanced to large extend, i.e., not many magnetic field lines connect the AR with external regions. The flux-balance is illustrated in panel (a) of Fig. 4.3, which shows the ratio of the net flux Φ to the unsigned flux Φ_0, i.e.,

$$\frac{\Phi}{\Phi_0} = \frac{\sum_p B_z}{\sum_p |B_z|},$$

where $\sum_p$ denotes a summation over all pixels of the magnetogram used for the extrapolation (see Fig. 4.2). The figure reveals that the net flux is at most $\sim 6\%$ of total the unsigned flux. The small value of Φ/Φ_0, indicates that most of the magnetic field lines originating from the magnetogram return to the magnetogram. Panel (b) of Fig. 4.3 shows the ratio of the net vertical current J_z to the unsigned vertical current J_{z0}, i.e.,

$$\frac{J_z}{J_{z0}} = \frac{\sum_p j_z}{\sum_p |j_z|},$$

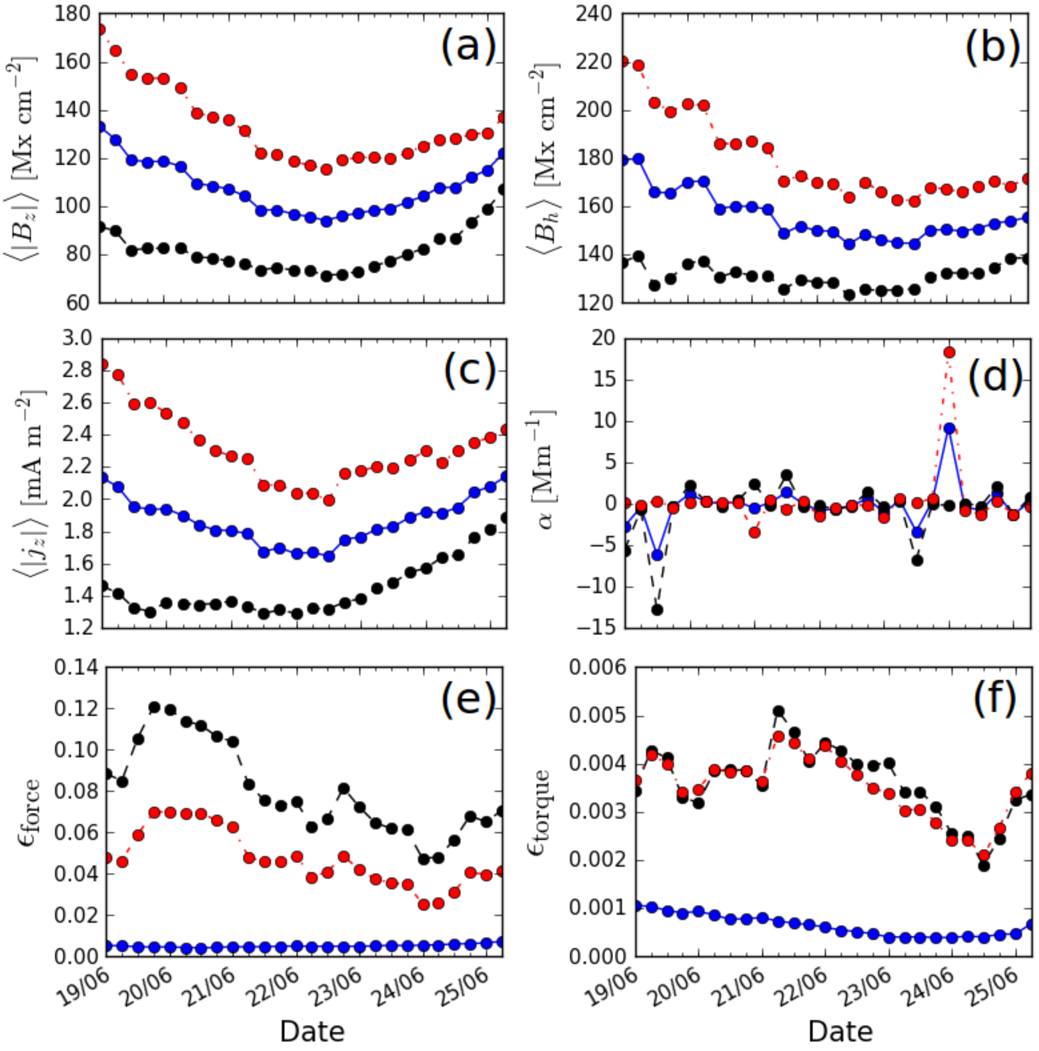

Figure 4.4: For all plots, the red curve corresponds to the left part, the black curve to the right part, and the blue curve to the entire magnetogram. (a) The average unsigned vertical magnetic component. (b) The average magnitude of the horizontal flux. (c) The average unsigned vertical current density. (d) The average force-free parameter. (e) The force metric $\epsilon_{\rm force}$. (d) The torque metric $\epsilon_{\rm torque}$.

where $\sum_p$ again denotes a summation over all pixels of the magnetogram. The small value of J_z/J_{z0}, indicates that most of the current leaving the magnetogram, returns somewhere else to the magnetogram. This means that most current is confined to the magnetogram and the regions above it, and only a little current is flowing from or towards regions located outside the magnetogram. This is important since the optimization method, as implemented in this work, keeps a potential field fixed at the side and top boundaries of the computational box. Since a potential field has zero current, the optimization method does not allow any current to leave the computational box.

Panel (a) of Fig. 4.4 shows the evolution of the average unsigned vertical magnetic flux $\langle|B_z|\rangle$, for the left part, the right part, and the entire magnetogram. Likewise, panel (b) gives the evolution of the average horizontal flux $\langle B_h\rangle$, where

$$B_h = \sqrt{B_x^2 + B_y^2}.$$

Remark that most of the flux is concentrated in the right part of the magnetogram. In addition, we see that from 19 to 23 June, both the vertical and horizontal magnetic flux show a decreasing trend. Moreover, panels (a) and (b) of Fig. 4.4 reveal that the strongest decrease of flux is situated in the left part of the magnetogram, i.e., the part that contains polarity regions P and N1. The magnetogram evolution, shows that polarity regions P and N1 interact strongly with each other. It is therefore likely that the interaction between these opposite polarities induces magnetic cancellation (Martin et al. 1985). The mechanism that drives this cancellation will be discussed in Section 4.3.3, when discussing the magnetic topology of the extrapolated fields.

Panel (c) shows the evolution of the average unsigned vertical current density. Remark that this figure is very similar to panel (a), which follows from the fact that for a force-free field $\mu_0 j_z = \alpha B_z$. Note that the vertical current density j_z is computed from the derivatives of the horizontal magnetic field components. Recall from Section 1.3 that these horizontal magnetic components are subjected to significant noise, such that the obtained values for j_z should be treated with caution. A similar remark can be made about the force-free parameter α, since it is computed as the ratio of $\mu_0 j_z$ to B_z. The average value of the force-free parameter α of the magnetogram is shown in panel (d) of Fig. 4.4. The figure shows that there are some clear spikes in the evolution of the parameter. However, most of the time $\langle\alpha\rangle$ has a value between -1 and $1\ \mathrm{Mm}^{-1}$. This is reflected in the median value of $\langle|\alpha|\rangle$, which equals $0.57\ \mathrm{Mm}^{-1}$.

The last row of Fig 4.4 shows the force and torque metrics $\epsilon_{\mathrm{force}}$ and $\epsilon_{\mathrm{torque}}$. These metrics were introduced in Eq. (2.91), and provide a measurement of the force and torque present in the magnetogram, respectively. Their values are low since the magnetogram was preprocessed. Moreover, panel (f) shows that both sides of the magnetogram have similar integrated torque values. However, from panel (e) we can see that the right part of the magnetogram contains twice as much force as the left part of the magnetogram. We can thus expect that the optimization code will perform better on the left part of the magnetogram than on the right part. This needs to be kept in mind when analysing the extrapolated fields.

4.3 Extrapolated Magnetic Field

4.3.1 Extrapolation Metrics

This section presents an analysis of the performance of the optimization code in producing force-free and divergence-free magnetic fields from the given set of magnetograms. To quantify how force-free the extrapolated fields are, we use the $\mathrm{CW}\sin\theta$ metric, which was introduced in Eq. (3.5). Recall that this metric gives the current weighted angle between the magnetic field $\mathbf{B}$ and the current density $\mathbf{j}$, such that it vanishes for a perfectly force-free field. Panel (a) of Fig 4.5 shows this metric for the different set of computed extrapolations. The average value of $\mathrm{CW}\sin\theta$ during the whole period and for the whole magnetogram is 0.36, which corresponds to an angle of $\sim 20^\circ$. Panel (a) also reveals that the left part is considerably more force-free than the right part. Over the whole period, the left part has an an average $\mathrm{CW}\sin\theta$ value of 0.3, whereas the right part has an average $\mathrm{CW}\sin\theta$ of 0.46. These values correspond respectively to angles of $\sim 17^\circ$ and $\sim 47^\circ$. The higher force-freeness of the left part can be attributed to the smaller amount of force present in the left part of the magnetogram (see above). Recall that for the semi-analytical test cases discussed in Chapter 3, we obtained values of $\mathrm{CW}\sin\theta$ between 0.10 and 0.20 (see Tables 3.3,3.6 and 3.7). These values corresponded to angles between 5.7° and 11°. This shows that the performance of the optimization method in the left part of computational volume is slightly worse than the results obtained for the semi-analytical test cases. Since the optimization code was able to reproduce the semi-analytical fields well, one can thus expect that the magnetic field obtained in the left part will be a fairly good approximation of the real magnetic field. In contrast, the $\sim 47^\circ$ angle obtained in the right part of computational volume indicates that the optimization method did not succeed well in finding a force-free configuration. Therefore, it is expected that the magnetic field in the right part of the

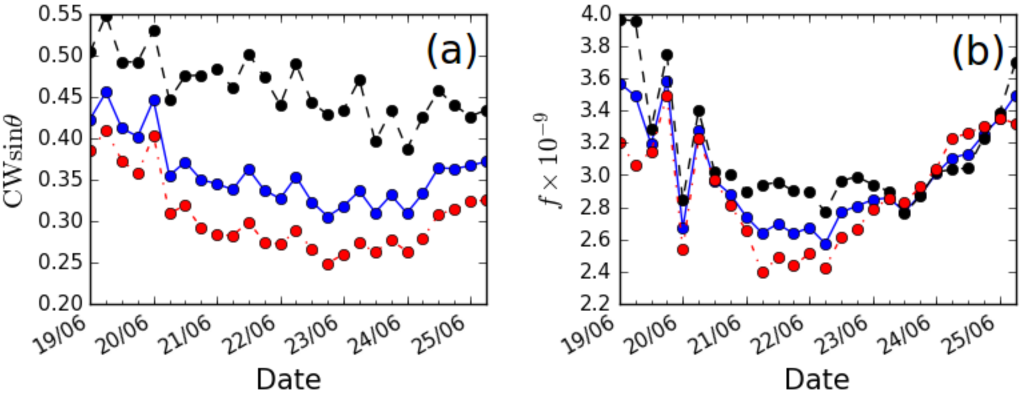

Figure 4.5: (a) The force-free metric $\mathrm{CW}\sin\theta$. (b) The divergence metric f. In both panels (a) and (b), the black curve refers to the right part of the computational box, the red curve to the left part of the computational box, and the blue curve to the entire computational box.

volume will be a rather poor approximation of the real solar field.

Since physical magnetic fields are solenoidal, we also quantify how divergence-free the extrapolated fields are. This is done using the f-metric introduced in Eq. (3.8). Similar conclusions as for the $\mathrm{CW}\sin\theta$ metric can be made. For the dates before 24 June, the extrapolation method produces a magnetic field that is more divergence-free in the left part of the magnetogram than in the right part. The difference is especially notable for the eight extrapolations on 21 and 22 June. Thereafter, the left part has a slightly higher value of f, although the difference between the two sides remains small.

When using estimates of physical quantities that rely on the extrapolated fields, it should be kept in mind that the the right part of the magnetogram is less force-free and divergence-free than in the left part. In addition, remark that the worse performance in the right part is surprising, since EUV images reveal that all flares and CMEs originate from the left part of the magnetogram, and therefore the left part is expected to deviate more from a potential field configuration. However, the right part of the magnetogram contains weaker magnetic fields and currents than the left part. In Chapter 3 we saw that the optimization code performs better in regions with strong currents and magnetic fields. This may, at least partly, explain the better results obtained in the left part than in the right part of the magnetogram.

4.3.2 Global Evolution of the Magnetic Field

Figure 4.6 shows four snapshots of the evolution of the AR. The snapshots were taken at 06:00 UT on June 19, 21, 12 and 25, respectively. The left column shows AIA 171 Å observations of the AR, whereas the right column shows the corresponding reconstructions by means of our optimization code. The colours of the field lines are proportional to the current density along the magnetic field lines. Green and cyan colours correspond to low currents, whereas colours like blue and purple represent stronger currents. The regions that contain strong localized currents indicate a non-potential magnetic field.

The EUV radiation emitted by the hot coronal plasma reveals signatures of the magnetic topology of the AR. This can be compared with the magnetic field lines of the extrapolations. Remark however that not all the magnetic field lines are outlined on the EUV images. The field lines will only be visible if the plasma along these lines has a sufficiently high density and temperature. In addition, there is a strong line of sight effect since coronal EUV lines are optically thin lines. Moreover, since we do not have images of the AR taken from another angle, we are limited to the 2D top-views shown in Figure 4.6 to evaluate the magnetic structure. The AR also does not stay at the centre of the solar limb, such that the

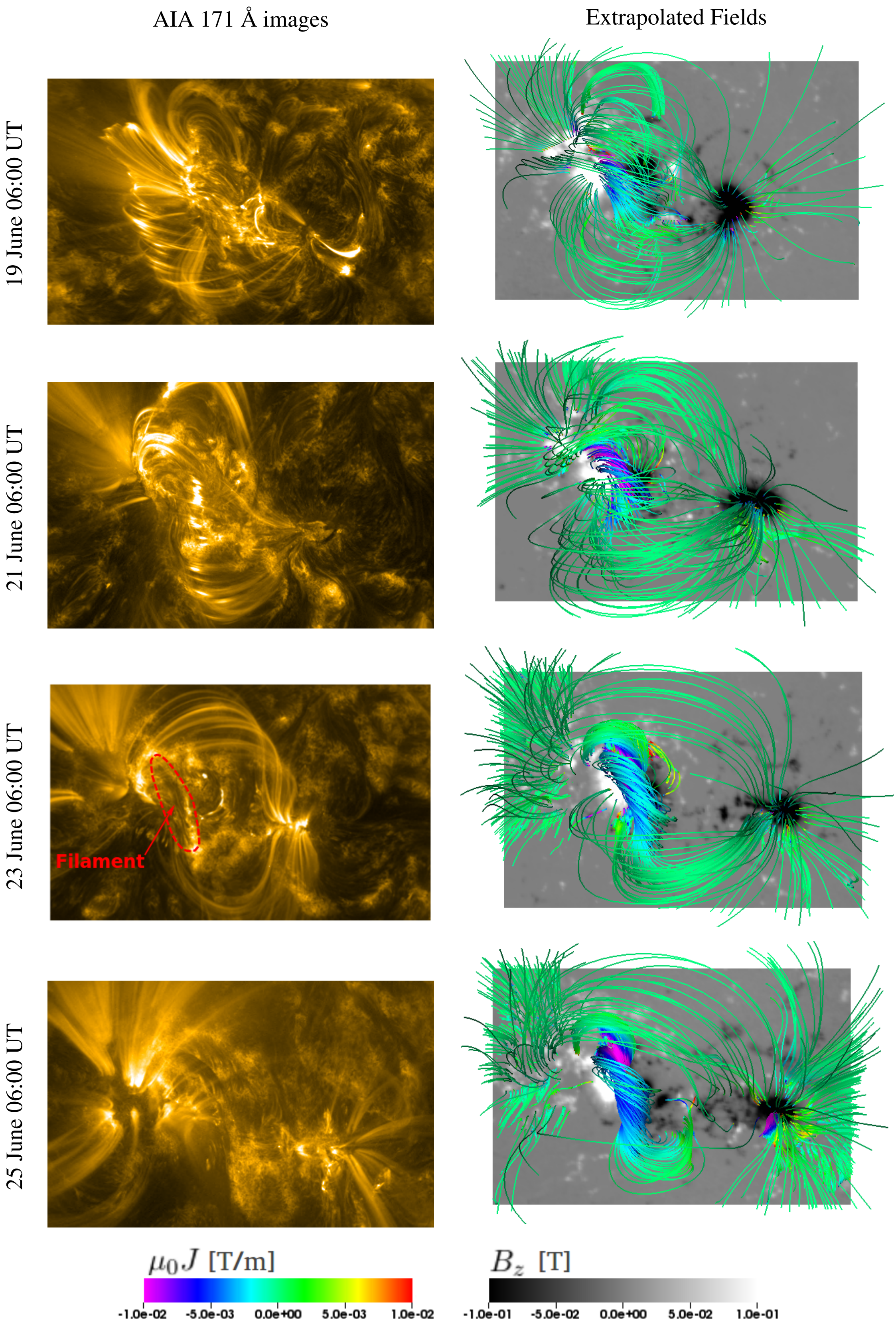

Figure 4.6: AIA 171 Å images of the AR and the corresponding reconstructed magnetic field. The different rows correspond respectively to 19 June 06:00 UT, 21 June 06:00 UT, 23 June 06:00 UT, and 25 June 06:00 UT. The grey-scale is proportional to the vertical magnetic field, whereas the “rainbow” colour scale is proportional to the current density along the magnetic field lines.

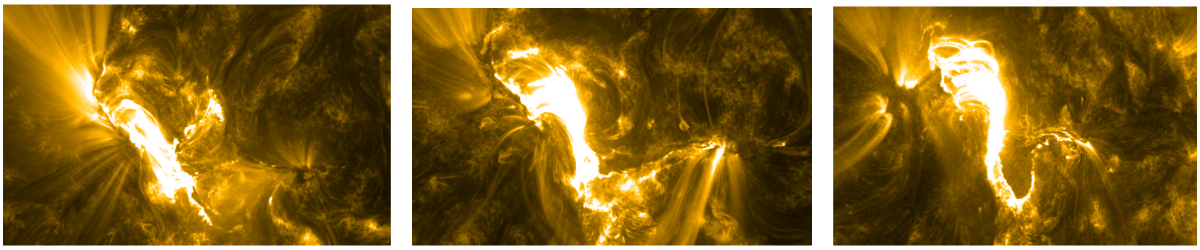

(a) 21 June, 02:50 UT **(b)** 22 June, 18:35UT **(c)** 25 June, 08:35 UT

Figure 4.7: AIA 171Å images of the AR during the three M-class flares.

EUV images are subject to varying projection effects. Consequently, it is often difficult to compare the EUV images with the extrapolations.

Figure 4.6 reveals that the regions that show large loops in the EUV images often also have similar large loops in the extrapolations. Moreover, the upward field lines in the upper left corner of the EUV images are also present in the magnetic field extrapolations. At first sight, a major difference between the EUV images and the extrapolated fields seems to be the blue flux-rope structure that is present in the extrapolations. However, a closer inspection of the EUV images reveals the presence of a dark filament-like structure on the location where the extrapolations show a flux-rope. In Fig. 4.6, this filament is clearly visible on the image of 23 June. In addition, when looking at EUV images taken during the transient eruptive events discussed in Section 4.1, the flux-rope structure becomes visible as a very bright structure. This is illustrated in Fig. 4.7, which shows the AR during the flares occurring at the major events on 21 June at 02:50 UT, on 22 June at 18:35 UT, and on 25 June at 08:35 UT. We see that there is a clear similarity between the brightened structures on the three images of Fig 4.7 and the flux-rope structure in the last three extrapolations of Fig. 4.6. A possible explanation for the brightening of the filament could be that the eruptions injects hot plasma into the flux-rope. In the next section, we will discuss the evolution and topology of the flux-rope in more detail.

4.3.3 Evolution of the Flux-Rope

In this section, we study the evolution of the flux-rope structure in more detail. The different panels of Fig 4.8 show the flux-rope at 00:00 UT on 19, 20, 21, 22, 23, 24, and 25 June. Panel (a) shows that on 19 June the magnetic field has a topology of a sheared arcade rather than a flux-rope topology. During the next days, the shear increases and the arcade structure gradually evolves into the flux-rope structure showed in panel (f) and (g) of Fig. 4.8. Although the flux-rope can thus be better described as a tangled arcade during the first days of the extrapolations, we will for simplicity often refer to it as a flux-rope in the following.

Figure 4.9 shows the magnitude of the current density $\mathbf{j}$ in a vertical plane, cutting the flux-rope halfway. In addition, some projected magnetic field lines are drawn. The left panel corresponds to 19 June and shows that the sheared arcade present at that time contains some strong current densities, up to a height of $\sim$ 25 Mm. The right panel corresponds to 25 June. This panel shows clear signatures of helical magnetic field lines, rotating around an axis at about 14 Mm altitude. In addition, we see that the flux-rope contains a relatively strong current density compared to the surroundings.

The observed flux-rope formation process is in agreement with the theoretical model developed by van Ballegooijen & Martens (1989). This model is illustrated in Fig. 4.10 and goes as follows. At the start, a more or less potential field arcade connects two regions of opposite magnetic polarity. Next, differences in the velocities of the plasma flows (i.e., shear flows) of both polarity regions transform the potential field into a sheared arcade. This is illustrated in panels (b) and (c) of Fig. 4.10. The shear flows cause

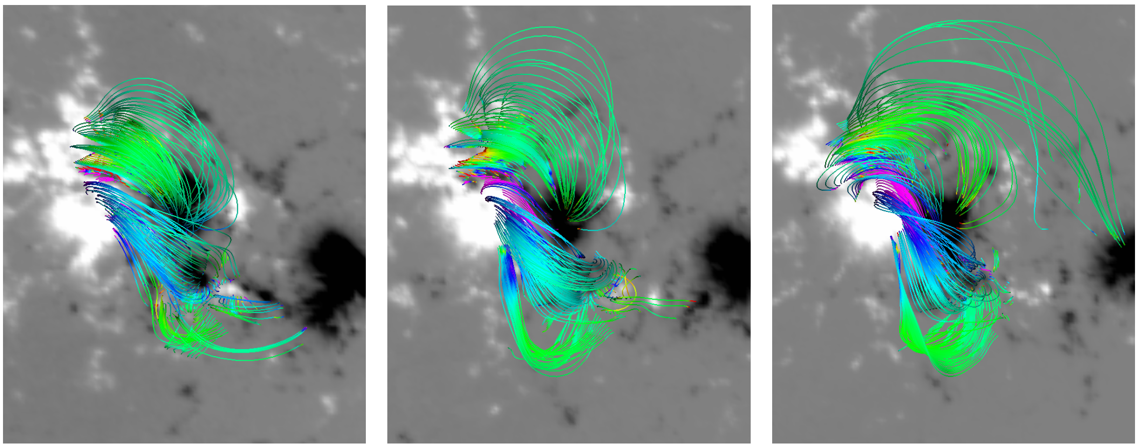

(a) 19 June, 00:00 UT **(b)** 20 June, 00:00 UT **(c)** 21 June, 00:00 UT

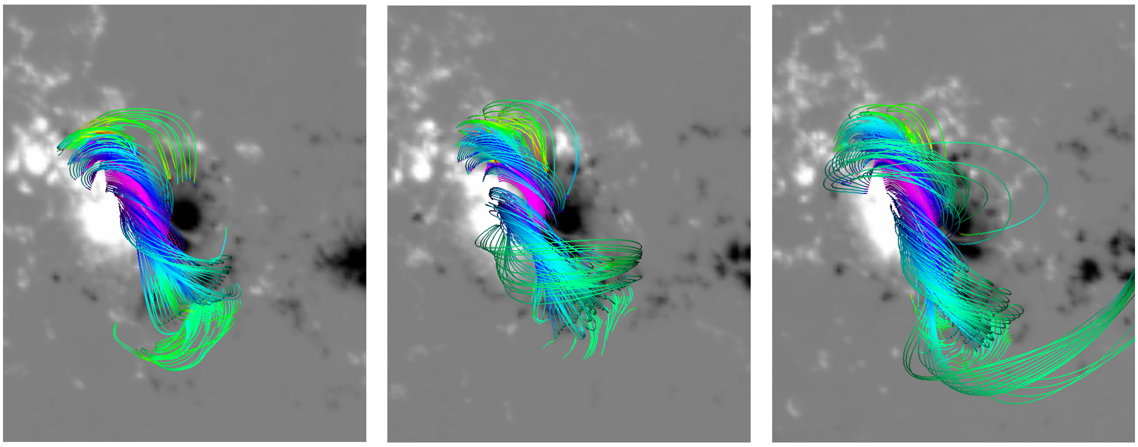

(d) 22 June, 00:00 UT **(e)** 23 June, 00:00 UT **(f)** 24 June, 00:00 UT

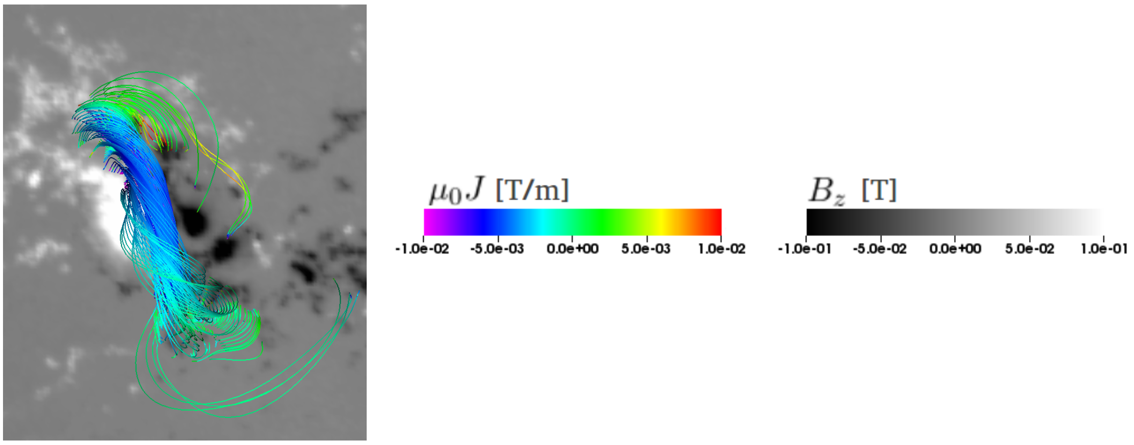

(g) 25 June, 00:00 UT

Figure 4.8: Snapshots of the arcade/flux-rope structure. The grey-scale is proportional to the vertical magnetic field, whereas the "rainbow" colour scale is proportional to the current density along the magnetic field lines.

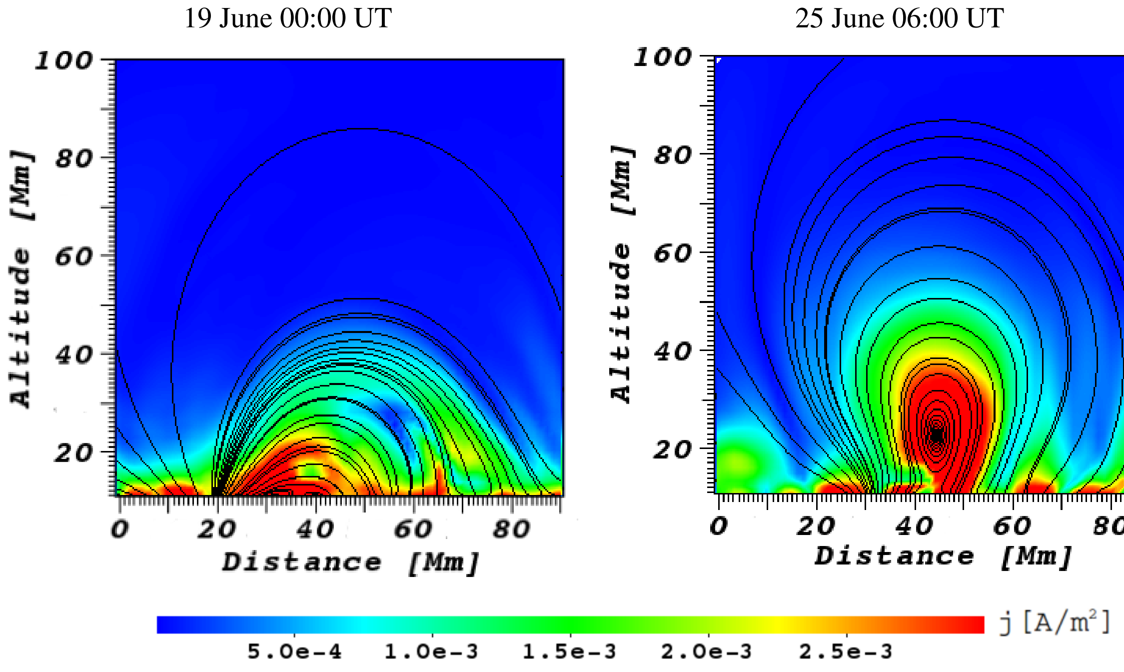

Figure 4.9: Cross-sections of the arcade/flux-rope structure for 19 (left) and 25 (right) June. The color scale gives the magnitude of the current density **j**. The black lines are magnetic field lines projected on the cross-section.

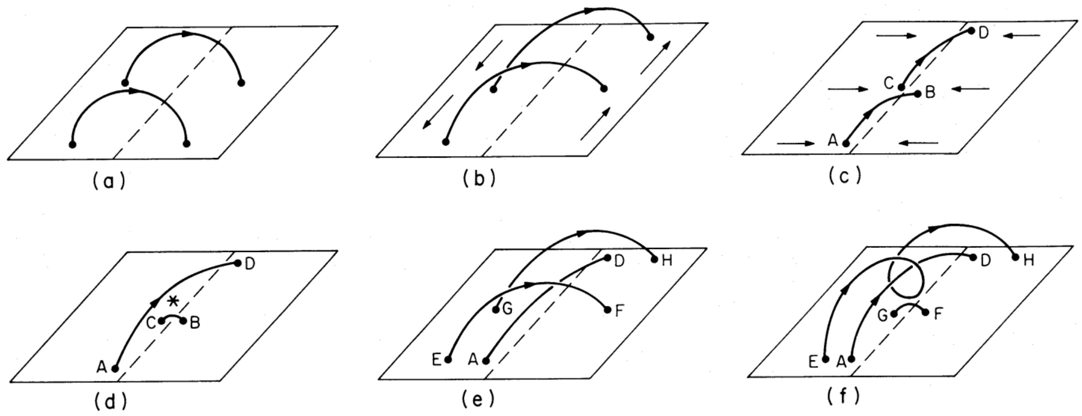

Figure 4.10: Panels (a) to (c) illustrate how a coronal arcade connecting opposite magnetic polarities transforms in a sheared arcade. Panel (c) shows how reconnection results in a long loop, labelled AD, and a short potential loop, labelled CB, which submerges. Panels (e) and (f) show how overlying loops repeat the process, eventually producing the helical field line topology of a flux-rope. Image from van Ballegooijen & Martens (1989).

the magnetic field lines to be more aligned with the neutral line separating the two opposite polarities. In addition, the shearing motions bring the footpoints of the magnetic field lines on opposite polarities closer together. This is illustrated in panel (c) of Fig. 4.10, where footpoints B and C are close to each other. Eventually, the converging opposite polarity fragments will reconnect, producing a long field line nearly parallel to the neutral line and a smaller loop that is more or less potential, i.e., it is orthogonal to the neutral line. This is illustrated in panel (d) of Fig. 4.10, where the asterisk denotes the reconnection site. The magnetic tension force at the zenith of a magnetic loop equals $B^2/(4\pi R)$, with R the local curvature radius. This inverse proportionality to the curvature radius causes a strong tension force in the small loop, and as a consequence, it will be pulled down beneath the photosphere. Remark that these reconnection processes and the subsequently submergence of the smaller magnetic loops will decrease the magnetic flux at the photosphere. Therefore, these reconnection processes are called flux cancellation episodes. In a next step, other field lines, whose footpoints were initially further away from the neutral line, evolve trough the same process. The result is the helical field structure of a flux-rope, as illustrated in panel (f) of Fig. 4.10.

The magnetic field evolution shown in Fig. 4.8 indeed shows how a sheared arcade evolves into a flux-rope structure. In addition, the extrapolations show the presence of enhanced current densities in the flux-rope region, which is typical for reconnection sites (Priest & Forbes 2006). The helical field structure predicted by the model (see panel (f) of Fig. 4.10) is also clearly present in the extrapolated fields, as shown in the right panel of Fig. 4.9. Moreover, remark that panels (a) and (b) of Fig. 4.4 show a decreasing magnetic flux, especially in the left side of the magnetogram. Since the flux-rope is located above the left side of magnetogram, this decrease in flux can thus be explained as a consequence of the submergence of small reconnected loops.

On 25 June, at 06:00 UT, the total unsigned flux of the left side of the magnetogram is $\approx 1.7 \times 10^{21}$ Mx. This is 0.5×10^{21} Mx less than the peak value of $\approx 2.2 \times 10^{21}$ Mx reached on 19 June at 00:00 UT. This corresponds to a decrease of $\approx 23\%$ of the absolute flux of the AR on 19 June. If all flux cancellation occurs through the process discussed above, then about 30% of the total flux of the magnetogram is contained in the flux-rope on 25 June. In Bobra et al. (2008) and Su et al. (2009), three ARs containing a flux-rope are studied using a flux-rope insertion method. The authors find that the flux-ropes become unstable if more than $\sim 10\%$ of the unsigned magnetic flux is contained in the flux-rope. The 23% that we obtain is thus well above this limiting value of 10%. However, the value of 23% is derived under the assumption that all the reconnected field lines become part of the flux tube. As argued in Green et al. (2011), this does not need to be the case. In addition, it is expected that the CME eruptions on 21 and 22 June will carry away part of the magnetic flux, and there may be magnetic flux exiting and/or entering the magnetogram window from each side.

From the AIA images, it can be seen that all flares and the CMEs on 18, 21, 22 and 25 June originate from the vicinity of the arcade/flux-rope structure. This supports the idea that a flux-rope is, at least for some CMEs, already present before the actual onset of the eruption. This is in agreement with the observational studies of e.g., Green & Kliem (2014) and Aulanier et al. (2010). In addition, the extrapolations suggest that the flux-rope, or at least part of it, can survive multiple CMEs. In other words, a CME can be caused by a partial eruption of a flux-rope. This supports the observations made in Green & Kliem (2014), where a sigmoid was observed to outlive a CME eruption.

4.3.4 Energies

The flux cancellation model of van Ballegooijen & Martens (1989) assumes that small loops formed through the reconnection process (see loops CB and GF in Fig. 4.10) are submerged under the photosphere. As argued in the previous section, these small loops are expected to be close to a potential state,

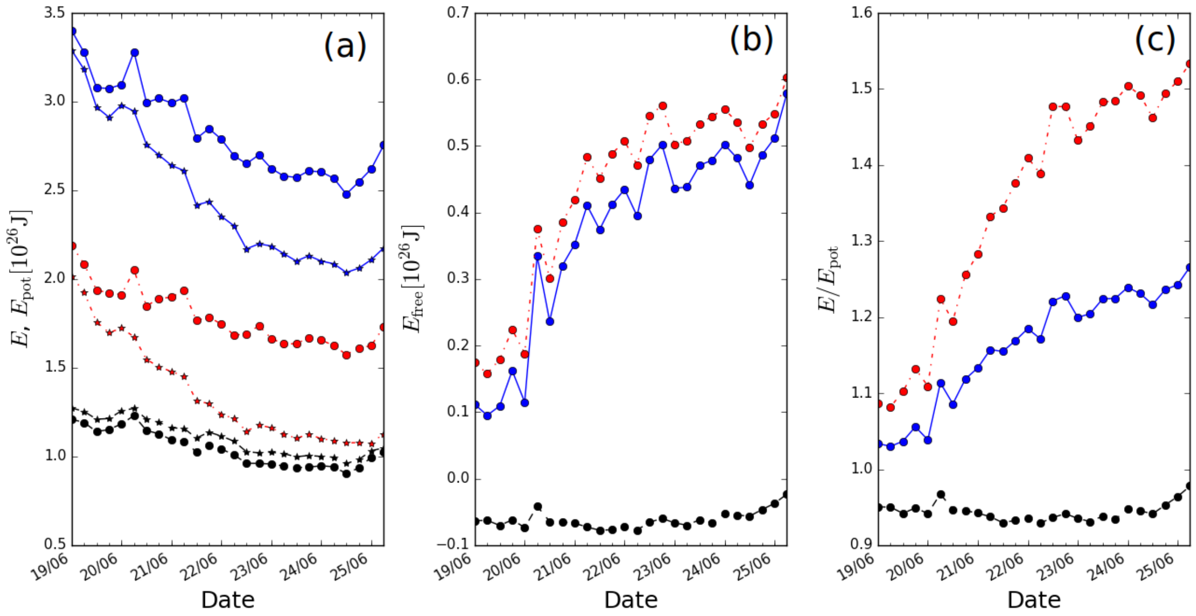

Figure 4.11: (a) The lines with full dots give the total energy. The lines with star symbols give the energy of the potential field. (b) The free magnetic energy. (c) Ratio of the total energy over the energy of the potential field. In each plot, the red dot-dash line represents the left part, the black dashed line the right part, and the blue full line the entire computational volume.

and hence their submergence leaves a more non-potential field behind in the corona. As a consequence, the magnetic free energy (see Eq. (2.12)) is expected to increase.

Figure 4.11 gives the evolution of the energetics of the extrapolated fields. Panel (a) shows the total energy of the magnetic field of the AR, and reveals that the energy is constantly decreasing from 19 to 25 June. In contrast, panel (b) reveals that the free magnetic energy increases over time. Panel (c) shows that the ratio between the total energy and the energy contained in the potential part of the magnetic field steadily increases. The decrease in total energy is thus largely due to a decrease in the energy of the potential part of the magnetic field, which is consistent with the flux cancellation process discussed above.

We remark that Fig. 4.11 reveals that on the right part of the computational box, the potential field seems to have a higher energy than the extrapolated field. This is in contradiction with the potential minimum energy theorem derived in Section 2.2.1. A similar problem was observed with the extrapolations in Section 3.4, where the contradiction with the potential minimum energy theorem could be explained by the fact that the extrapolated field is not perfectly divergence-free, like a real physical magnetic field is. This indicates thus that the reconstruction of the magnetic field in the right part of the computational box, and any numbers derived from it, should be treated with caution. The worse performance of the optimization code in the right part of the magnetogram compared to the left part, was already noted in Section 4.3.1, and can be attributed to the larger force present in the right part of the magnetogram (see Section 4.2). Note however that the energy and the changes in the energy are dominated by the contributions of the left part of the computational box, i.e., the part that contains the flux-rope. The magnetic field in the right part seems to play only a minor role in producing the eruptive phenomena.

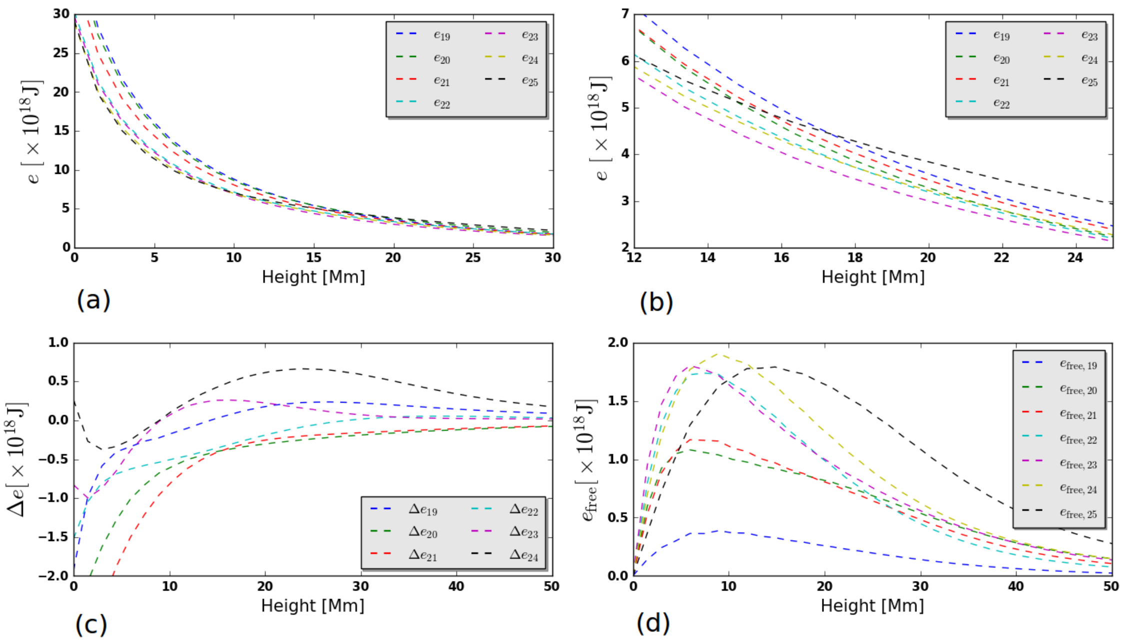

Figure 4.12: (a) Integrated magnetic energy distribution as a function of heigth. The different colours represent the different days, as indicated by the subscribts in the legend of the figure. (b) Same as (a) but zoomed in on the heights where the curves shift from order. (c) The difference in energy density for successive days. (d) The integrated magnetic free energy density as a function of height.

4.4 Energy Distribution of the Magnetic Fields

In this section we investigate how the energy density behaves as a function of height. This is done by integrating for each height z the energy density over a horizontal plane, i.e.,

$$e(z) = \int_S \frac{B^2}{2\mu_0} dxdy, \tag{4.1}$$

with S a horizontal plane at height z. The variable e gives thus the integrated magnetic energy distribution as a function of height above the photosphere.

4.4.1 Long Term Evolution of the Energy Distribution

Panel (a) of Fig 4.12 shows $e(z)$ for the extrapolated fields of 19, 20, 21, 22, 23, 24 and 25 June at 06:00 UT. As expected, the major part of the energy is located close to the photosphere. Moreover, as the AR evolves, we see that the energy stored in the layers just above the photosphere decreases with time. In contrast, panel (b) shows that the order of the curves starts reversing at heights higher than $\sim 12\mathrm{Mm}$. This means thus that the energy content at large altitudes increases over time. This behaviour is more clearly illustrated in panel (c), where we show $\Delta e_i = e_{i+1} - e_i$, where the index i refers to the ith day of June.

The decrease of energy at low altitudes can be attributed to the flux cancellation event occurring at the flux-rope structure (see Section 4.3.3). Similarly, the increasing energy at higher altitudes may be due to the formation of a flux-rope, which causes magnetic flux concentrations and hence a magnetic energy concentration at larger heights. In addition, any expanding motion of the flux-rope will shift some of the energy higher up into the corona. Panel (d) of Fig 4.12 gives the free energy density as function of height, i.e.,

$$e_{\text{free}}(z) = e(z) - e_{\text{pot}}(z),$$

where e_{pot} is the integrated energy density of the potential field. The increase of free magnetic energy over time, as already illustrated in Fig 4.11, is here also clearly visible. In addition, panel (d) also reveals that the entire free energy curves $e_{\text{free}}(z)$ are slightly shifted towards larger heights as the AR evolves. Especially on 25 June, a lot of free energy is shifted toward larger heights compared to the previous days. Recall that we used the extrapolated fields at 06:00 UT of each day to compute these energy distributions. For 25 June, this is only two hours and thirty minutes before the onset of an M7.9 class flare and a CME. The strong increase in free energy at high altitudes may thus be a signature of some pre-eruption mechanism, like an expanding motion and/or the beginning of an instability that eventually leads to the the launch of the CME. We will discuss this in more detail in Section 4.5, where we investigate the stability of the flux-rope.

4.4.2 Evolution of the Energy Distribution During Eruptive Events on 21 and 22 June

Besides the events on 25 June, we recall from Section 4.1 that there was also substantial solar activity on June 21 and 22. On 21 June, two M-class flares were observed, together with a CME that was launched at 02:36 UT. On 22 June, there was a bright M6.5 class flare accompanied by another CME eruption at 18:36 UT. For these dates, we have extrapolations both before and after the eruptive events. Panels (a) and (b) of Fig. 4.13 show the integrated free energy distribution of the extrapolations before and after these events. Remark that for both events, the free energy at low altitudes seems to increase, whereas the free energy at higher altitudes seems to decrease. Panels (c) and (d) of Fig. 4.13 show the difference in the total energy distribution of the extrapolations before and after the events. Both figures show that there is an increase of energy at lower altitudes and a decrease of energy at higher altitudes. This behaviour is more pronounced for the event on 23 June. Remark that this behaviour is different from the long term evolution of the energy distribution of the AR, which instead favours a decrease of energy at low altitudes and an increase of energy at high altitudes (see discussion above, and panel (c) of Fig. 4.11). This suggests that the behaviour of the energy distribution in panels (c) and (d) of Fig. 4.13 is possibly a consequence of the flares and CMEs that occurred on 21 and 22 June.

It is generally accepted that magnetic energy is the main energy source of flares and CMEs. Removal of magnetic energy by these events leads to a decrease in the magnetic pressure gradient, and as a result the magnetic field contracts or “implodes” until it reaches a new balance (Hudson 2000; Hudson et al. 2008). Such an implosion transports magnetic energy towards lower altitudes, resulting in an energy distribution more concentrated just above the photosphere. This scenario is consistent with the data presented in Fig. 4.13 that shows a decrease of magnetic energy at high altitudes and an increase at lower altitudes. Observational evidence for such an implosion of the coronal magnetic field after flares or CMEs can be found in Khan et al. (2006); Liu et al. (2009); Liu & Wang (2010); Liu et al. (2012); Simões et al. (2013); Shen et al. (2014). Our results indicate that nonlinear force-free extrapolations are able to reproduce this phenomenon in terms of variations in the energy distribution.

It would be interesting to estimate how much magnetic energy is put into the flares and CMEs. This can be done by comparing the free magnetic energy before the eruptions with the free magnetic energy after the eruption. The difference between those quantities reveals then how much magnetic energy was used to drive the CME and flares. However, when calculating the total free energy available in the extrapolated magnetic field of 21 June at 06:00 UT, we find that it is $\sim 6 \times 10^{24}$ J higher than the free energy content on 21 June at 00:00 UT. Instead of a decrease, we find thus an increase in free magnetic energy. So it seems that neither the M2.0 and M2.6 class flares nor the CME have any significant impact on the total free energy content of the magnetic field. This may be a result of the six hour time span between our

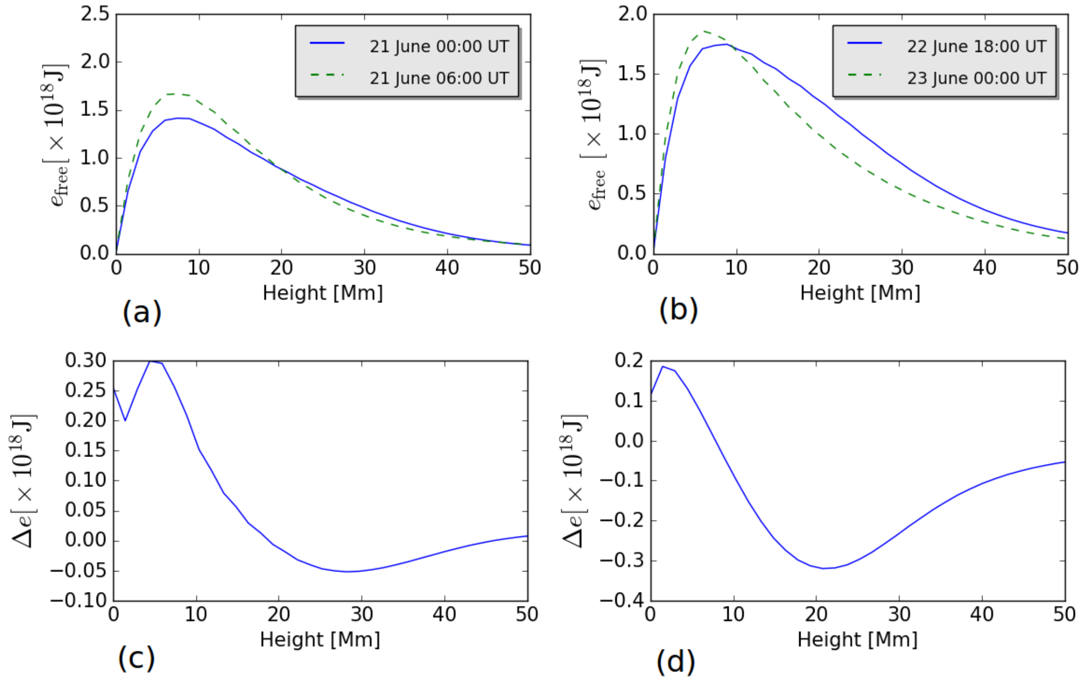

Figure 4.13: Panel (a) and (b) give the integrated free energy distribution for indicated times. Panel (c) gives the difference of the integrated energy densities of 21/06 06:00 UT and 21/06 00:00 UT. Panel (d) gives the difference of the integrated energy densities of 22/06 18:00 UT and 23/06 00:00 UT.

successive extrapolations, i.e., the magnetic free energy decrease due to the CME and flares may simply not have been temporarily resolved.

For the events on 22 June, we find that the total free energy available on 22 June at 18:00 UT is decreased with an amount of $\sim 7 \times 10^{24}$ J compared to 23 June at 00:00 UT. This is sufficient energy to power the M6.5 flare occurring during that period. A typical energy of a moderately large CME is of the order of $\sim 10^{25}$ J (Forbes 2000). A free energy decrease of $\sim 7 \times 10^{24}$ J is thus rather at the low side to power a CME, yet not impossible considering that 10^{25} J is only an order of magnitude estimate. Similar to the 21 June event we remark that there may be processes occurring, like flux cancellation, that constantly increase the available free magnetic energy during the six hour period between successive extrapolations. Therefore one can conclude that the cadence of six hours is probably a too coarse time resolution to demonstrate unambiguously dips in the free energy. We leave it for future work to compare extrapolations of magnetograms measured some minutes before and after the events.

4.5 Torus Instability

In Section 4.3.3 we discussed how a sheared arcade evolved into a flux-rope from 19 to 25 June (see Fig. 4.8). On 25 June at 08:48 UT, a bright flare and a CME are observed erupting from the vicinity of this flux-rope. In this section we investigate whether it is possible that this CME is triggered by a torus instability of the magnetic flux-rope. The torus instability was introduced in Section 2.4.1.2, when discussing the semi-analytical flux-rope model developed by Titov & Démoulin (1999). We recall that the instability occurs when there is a loss in balance between the downward and upward forces acting on the magnetic flux-rope. The upward force on the flux-rope is called the hoop force, and is due to the Lorentz force caused by the current flowing in the flux-rope. The downward stabilizing force is the

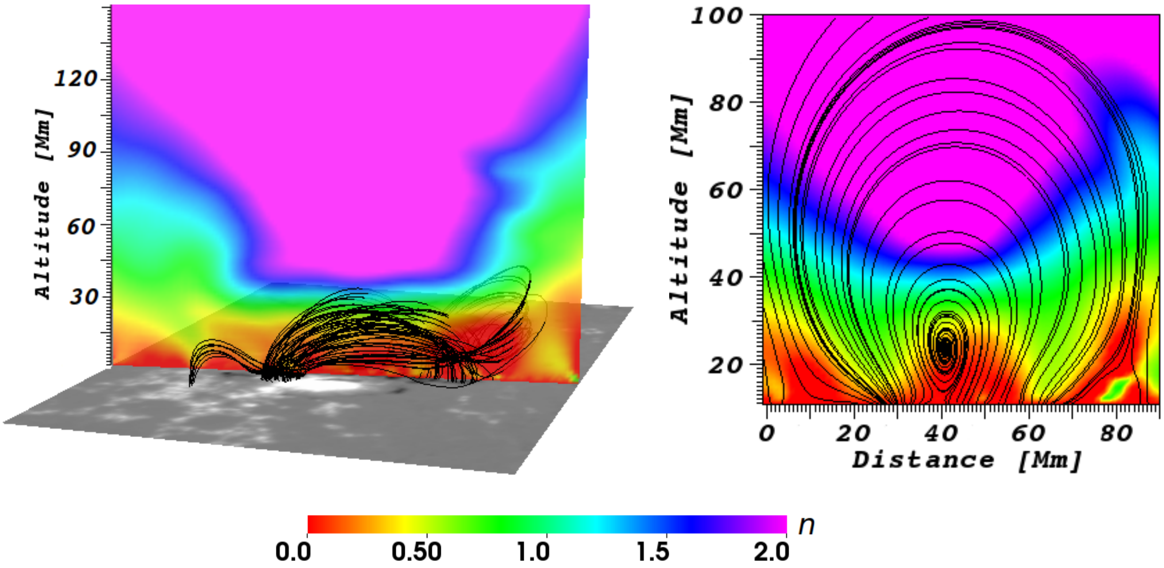

Figure 4.14: The color-code in left panel gives the decay index n in a vertical plane along the flux-rope axis. The right pinel shows the decay index in a vertical plane, orthogonal to the flux-rope axis. The black lines are magnetic field lines. Both figures were calculated from the extrapolation at 06:00 UT on 25 June.

Lorentz force caused by the overlaying magnetic field.

A criteria to determine whether a flux-rope is torus unstable can be found by assuming that the magnitude of the external field decreases with height as a power law, i.e., $B \propto R^{-n}$, where

$$n = -\frac{z}{B}\frac{\partial B}{\partial z}$$

is called the decay index. At the limit of very thin current channels, the flux-rope will be torus unstable if the decay index exceeds the critical value of 1.5 (see Kliem & Török 2006). This criterion was generalized by Démoulin & Aulanier (2010) for current channels with a finite thickness. They found that a flux-rope is torus unstable if the decay index is larger than a value in the range $[1.1, 1.3]$. The exact critical value depends on the shape of the flux-rope.

The left panel of Fig. 4.14 shows the decay index n in a vertical plane along the flux-rope axis, calculated from the extrapolation at 06:00 UT on 25 June, i.e., about three hours before the CME. The right panel of Fig. 4.14 shows also the decay index, yet for a vertical plane orthogonal to the flux-rope axis, and located halfway the flux-rope. The figures illustrate that most of the flux-rope satisfy $n \leq 1$. Therefore, the flux-rope can be considered to be stable against the torus instability. However, the left panel of Fig. 4.14 shows that some of the magnetic field lines at the top of the flux-rope are close to $n = 1.5$. Therefore, if the flux-rope would slightly expand, the upper parts of the flux-rope will reach a region that is unstable against the torus instability. Remark that we found in Section 4.4.1 that the peak in the energy distribution for 25 June is shifted towards higher altitudes compared to the previous days. This may be a signature of an expanding motion of the flux-rope. If such an expanding motion indeed occurs between 06:00 UT and 08:48 UT, the CME of 25 June may be triggered by the torus instability.

4.6 Summary and Conclusions

We studied the evolution of the three-dimensional coronal magnetic field configuration of AR 12371, from 19 June to 25 June 2015. This was done by extrapolating a set of 26 preprocessed magnetograms by means of the optimization method. The obtained magnetic field configurations were compared to EUV images of AIA. We computed the energy distribution of the magnetic field as a function of height, and paid special attention to reconfigurations in the energy distribution due to the flares and CMEs occurring on 21 and 22 June. Finally, we studied the torus instability as a possible trigger mechanism for the CME occuring on 25 June.

The extrapolations show a sheared arcade evolving into a flux-rope structure during the timespan of seven days. Combining this result with the observations of a decreasing photospheric magnetic flux and increasing free magnetic energy, we find strong evidence that a major flux cancellation event according to the model developed by van Ballegooijen & Martens (1989), resulted in the formation of a magnetic flux-rope. In addition, we remark that the observed flares and CMEs, occurring on 21, 22 and 25 June, originate from the location where the extrapolated magnetic fields contain the flux-rope structure. During these flares, the existence of this flux-rope is confirmed as a bright structure visible in AIA EUV images.

The presence of the flux-rope structure during several days suggests that a flux-rope can be present well before the onset of a CME. In addition, the extrapolations suggest that the flux-rope survives the CMEs occurring on 21 and 22 June. This supports the idea that a flux-rope does not need to erupt in its entirety to cause a CME. We would like to remark that this does not need to be in contradiction with the flux-rope structure observed in interplanetary CMEs, since much of the magnetic structure of interplanetary CMEs may be formed through reconnection processes after their launch (Qiu et al. 2007).

We also studied the energy distribution of the extrapolated fields as a function of height. We find that during the long term evolution of the AR, the magnetic energy at low altitudes ($\lesssim 15\mathrm{Mm}$) decreases, whereas the energy at higher altitudes shows an increasing trend. This can be understood as a consequence of the formation of the flux-rope through the flux cancellation mechanism. In addition we found a clear shift of free magnetic energy towards higher altitudes for the magnetic field of 25 June. This may be a signature of an expanding motion of the flux-rope.

A different evolution in the energy distribution is observed when looking at the extrapolations made directly before and after the flares and CMEs occurring on 21 and 22 June. The magnetic energy decreases at high altitudes and increases at low altitudes, resulting in a more compact energy distribution. This is consistent with a magnetic implosion, which happens because of a decrease in magnetic pressure. This decrease of magnetic pressure is a result of the magnetic energy loss during flares and CMEs.

The free energy available in the magnetic field does not decrease when comparing the extrapolations directly before and after the flares and CMEs occurring on 21 June. For the events of 22 June, we find a decreasing free energy, yet this decrease seems rather low to power a large CME. This might be the result of using a too coarse time grid, such that the events are not sufficiently resolved in time. To study the energy lost to flares and CMEs, one should use a much finer time resolution, e.g., the 12 minute cadence of the HMI full-disk vector magnetograms. Even when using such a fine time grid, one should be careful when using absolute values of physical variables obtained from the extrapolations. This is because the extrapolated fields are definitely not a perfect reproduction of the real solar magnetic field. Although the extrapolations discussed in this chapter seem to be in fairly good agreement with the observations, we find that in the right part of the computational volume, the extrapolated field has a lower energy than the potential field. Therefore, absolute values of the energy determined from the extrapolations may differ considerably from the real energy value.

Finally, we studied the stability of the magnetic flux-rope against the torus instability. This was done using the extrapolation of 25 June at 06:00 UT, i.e., about three hours before the CME eruption. Our results showed that at that time the flux-rope was located in a region stable against the torus instability. However, the upper part of the flux-rope was close to the instability zone. Therefore, a small expansion of the flux-rope could make it torus unstable. Since the evolution of the energy distribution suggests such an expanding motion, the torus instability should be regarded as a possible trigger mechanism of the CME on 25 June.

Chapter 5

Concluding Remarks

5.1 Summary and Conclusions

In this master thesis, we studied the three-dimensional structure of solar coronal magnetic fields above active regions (ARs). This was done by modelling the magnetic field as a nonlinear force-free field. The theory of force-free fields was elaborated in Chapter 2. We discussed the limitations of potential and linear force-free modelling of the coronal field, and introduced different methods to obtain a nonlinear force-free field from given boundary conditions. When using real data, these boundary conditions are available in the form of photospheric vector magnetograms. Since the photospheric field is not force-free, the magnetograms have to be preprocessed before they can be used as boundary conditions for the force-free extrapolation methods. Such a preprocessing method is introduced and discussed at the end of Chapter 2.

In Chapter 3, we discussed and tested an implementation of the optimization method. These tests used the semi-analytical nonlinear force-free fields that were introduced in Chapter 2. The performance of our optimization method was determined qualitatively, by comparing field lines of the extrapolated and model field, and quantitatively, by using different metrics that measure the agreement between the extrapolated and model field. We found a good agreement between the extrapolated fields and the semi-analytical models, both in a qualitative and quantitative manner. In addition, the results were better when considering a smaller region, centred in a larger computational box. This increase in performance can be partly attributed to the remoteness of the side and top boundaries of the computational box, since the optimization method, as implemented in this work, does not allow a departure of the magnetic field from a potential state on these boundaries. In addition, the optimization method was observed to perform best in regions where the magnetic field and the current are strong.

The semi-analytical test cases using the Titov & Démoulin (1999) flux-rope model illustrated that the optimization method is able to reconstruct a flux-rope topology, starting from a potential field that does not contain any flux-rope. In addition, the optimization code accurately reproduced the ratio of the total energy over the potential energy for the semi-analytical fields. In the last part of Chapter 3, we used the optimization code to extrapolate the vector magnetogram of NOAA 10978. These extrapolations showed the importance of data preprocessing before applying the optimization code. In addition we found that the performance of the optimization code decreases significantly with altitude above the photosphere. This is because at high altitudes, the magnetic field and the electric current density are considerably weaker than at low altitudes.

In Chapter 4, we studied the evolution of the magnetic field of NOAA AR 12371, from 19 June to 25 June 2015. During this period, the AR showed significant flare activity and three large CMEs were observed. The series of extrapolated fields showed a sheared arcade evolving into a flux-rope structure. Combining this result with the observations of a decreasing photospheric magnetic flux and an increasing free magnetic energy, we find strong evidence that a major flux cancellation event according to the model developed by van Ballegooijen & Martens (1989) resulted in the formation of a magnetic flux-rope. In addition, we remark that the existence of this flux-rope was confirmed as a filament-like structure in AIA EUV images.

Our findings suggest that a flux-rope can be present well before the onset of a CME. In addition, our extrapolations indicate that the flux-rope survives the CMEs occurring on 21 and 22 June. This supports the idea that a flux-rope does not need to erupt in its entirety to cause a CME. Studying the energetics of the magnetic fields before and after the eruptive events on 21 and 22 June, we found that the energy decreases at high altitudes and increases at low altitudes. This is consistent with a magnetic implosion, which happens because magnetic energy lost to flares and CMEs reduces the magnetic pressure such that the field contracts.

By studying the extrapolated fields in the left and the right part of the computational box separately, we found that the performance of the optimization method can show a strong spatial dependence within a single extrapolation. It is likely that this is also the case for other extrapolation methods. Remark that when using space-averaged metrics, a good performance in one part of the computational volume may mask a bad performance in another part of the computational volume. This in turn may lead to erroneous estimates of global variables like the total energy content of the magnetic field. To detect and prevent such errors, we recommend using spatial-dependent metrics in addition to space-averaged metrics before performing any physical analysis of the extrapolated fields.

Finally, we studied the stability of the magnetic flux-rope against the torus instability. This was done using the extrapolation of 25 June at 06:00 UT, i.e., about three hours before a large CME eruption. Our results showed that at that time the flux-rope was located in a region stable against the torus instability. However, the upper part of the flux-rope was located close to the instability zone. Therefore, a small expansion of the flux-rope could make it torus unstable. In the extrapolations of 25 June, there was a clear shift of free energy towards higher altitudes, which may be a signature of an expanding motion of the flux-rope. Therefore the torus instability should be regarded as a possible trigger mechanism of the CME on 25 June.

5.2 Future Prospects

We conclude this thesis by outlining some future possibilities of nonlinear force-free modelling. We start by discussing the research that can directly built onto the results obtained in this thesis.

The study of AR 12371, performed in Chapter 4, can be extended in several ways:

- Using a high time resolution, e.g., the 12 minute cadence of HMI full-disk vector magnetograms, one can investigate the transient eruptive events occurring between 19 June and 25 June in more detail. Such a study would clarify whether the optimization method is able to detect dips in the free magnetic energy that are unambiguously caused by flares or CMEs. If these dips are indeed detected, they may provide useful estimates of the energy content of flares and CMEs. In addition, it allows studying in more detail the reconfiguration of the magnetic topology after transient eruptive events.
- It would be interesting to redo the extrapolations performed in Chapter 4 using the full resolution of the HMI magnetograms. Such a study may reveal the influence of spatial resolution on the optimization method. It can be expected that the resolution-dependent effects are coupled to the complexity of the magnetic field. Therefore it is possible that resolution effects strongly

vary depending on the specific magnetogram under consideration. A practical problem is that the execution time and the memory usage of the extrapolations does not scale well with increasing resolution.

- It would be interesting to reconstruct the magnetic field of the AR, using different extrapolation methods, and subsequently compare the results. From such analyses, one can try to deduce whether there is one method that systematically outperforms the other methods.

Evidently, one should not limit oneself to the study of only one specific AR. It would be interesting to perform analyses similar to the one provided in Chapter 4, for a large set of ARs. A comparison of the differences and similarities between the magnetic field topologies of the different ARs, can provide insights about the features that are crucial for causing transient eruptive events. It could provide us with estimates about what portion of CMEs erupt from a flux-rope configuration, and whether it is common for these flux-ropes to erupt only partially.

When using the optimization method, we found that the results in general deteriorate near the side and top boundaries of the computational domain. This is because in our implementation of the optimization code, the magnetic field on the boundaries is kept fixed and equal to a potential field. This problem can be circumvented by using a large computational domain to compute the fields, yet focusing on a smaller inner volume for physical analysis. Unfortunately, the optimization method turns out to have hight time and memory complexity. An interesting challenge is therefore to extend the optimization code so that it can also alter the magnetic field on the side and top boundaries.

Nonlinear force-free fields can potentially be used in future space weather forecasting operations, as model of the coronal field. This would require fast nonlinear extrapolations of the magnetic field of the full solar disk. However, current nonlinear extrapolation methods are relatively slow, and very demanding in terms of computer memory. In their current form, the extrapolation methods can therefore not be used in space weather forecasts to obtain the global coronal field. It is thus important to develop faster implementations of nonlinear force-free extrapolation methods.

Finally, remark that nonlinear force-free magnetic field models only provide us information about the magnetic field and the electric current, but not about any plasma parameters. A next step is to include coronal plasma, and thus developing a reliable magnetohydrostatic equilibrium model. This is especially crucial for the low and top corona, where the force-free assumption is not satisfied. Future space missions like e.g., Solar Orbiter and Solar Probe Plus, will help to impose additional constraints on the modelling of the solar magnetic field.

Bibliography

Altschuler, M. D. & Newkirk, G. 1969, SoPh, 9, 131

Aly, J. J. 1989, SoPh, 120, 19

Aly, J. J. & Seehafer, N. 1993, SoPh, 144, 243

Amari, T., Boulmezaoud, T. Z., & Aly, J. J. 2006, A&A, 446, 691

Amari, T., Boulmezaoud, T. Z., & Mikic, Z. 1999, A&A, 350, 1051

Aulanier, G., Török, T., Démoulin, P., & DeLuca, E. E. 2010, ApJ, 708, 314

Bineau, M. 1972, Comm. Pure Appl. Math, 25, 77

Bobra, M. G., van Ballegooijen, A. A., & DeLuca, E. E. 2008, ApJ, 672, 1209

Borrero, J. M., Tomczyk, S., Kubo, M., et al. 2011, SoPh, 273, 267

Boulmezaoud, T. Z. & Amari, T. 2000, ZaMP, 51, 942

Charbonneau, P. 2010, LRSP, 7

Chen, P. F. 2011, LRSP, 8

Chiu, Y. T. & Hilton, H. H. 1977, ApJ, 212, 873

Close, R., Parnell, C., Mackay, D., & Priest, E. 2002, SoPh, 212, 251

Committee On The Societal & Economic Impacts Of Severe Space Weather Events. 2008, Severe Space Weather Events–Understanding Societal and Economic Impacts: A Workshop Report, Tech. rep.

De Pontieu, B., Erdélyi, R., & James, S. P. 2004, Natur, 430, 536

de Pontieu, B., McIntosh, S., Hansteen, V. H., et al. 2007, PASJ, 59, S655

De Rosa, M. L., Schrijver, C. J., Barnes, G., et al. 2009, ApJ, 696, 1780

Dedner, A., Kemm, F., Kröner, D., et al. 2002, JCoPh, 175, 645

del Toro Iniesta, J. C. 2007, Introduction to Spectropolarimetry

Démoulin, P. & Aulanier, G. 2010, ApJ, 718, 1388

DeRosa, M. L., Wheatland, M. S., Leka, K. D., et al. 2015, ApJ, 811, 107

Elsworth, Y., Howe, R., Isaak, G. R., et al. 1995, Natur, 376, 669

Forbes, T. G. 2000, JGRA, 105, 23153

Gary, G. A. 2001, SoPh, 203, 71

Gilbert, H. R., Holzer, T. E., Low, B. C., & Burkepile, J. T. 2001, ApJ, 549, 1221

Gilchrist, S. A. & Wheatland, M. S. 2013, SoPh, 282, 283

Green, L. M. & Kliem, B. 2014, in IAU Symposium, Vol. 300, Nature of Prominences and their Role in Space Weather, ed. B. Schmieder, J.-M. Malherbe, & S. T. Wu, 209–214

Green, L. M., Kliem, B., & Wallace, A. J. 2011, A&A, 526, A2

Hoeksema, J. T., Liu, Y., Hayashi, K., et al. 2014, SoPh, 289, 3483

Hood, A. W. & Priest, E. R. 1981, Geophysical and Astrophysical Fluid Dynamics, 17, 297

Hudson, H. S. 2000, ApJ, 531, L75

Hudson, H. S., Fisher, G. H., & Welsch, B. T. 2008, in Astronomical Society of the Pacific Conference Series, Vol. 383, Subsurface and Atmospheric Influences on Solar Activity, ed. R. Howe, R. W. Komm, K. S. Balasubramaniam, & G. J. D. Petrie, 221

Hughes, D. W., Rosner, R., & Weiss, N. O. 2007, The Solar Tachocline (Cambridge University Press)

Inhester, B. & Wiegelmann, T. 2006, SoPh, 235, 201

J.-P. Zahn (auth.), Jean-Pierre Rozelot, C. N. e. 2009, The Rotation of Sun and Stars, 1st edn., Lecture Notes in Physics 765 (Springer-Verlag Berlin Heidelberg)

Jackson, J. D. 1975, Classical electrodynamics

Jiang, C. & Feng, X. 2014, SoPh, 289, 63

Khan, J. I., Fletcher, L., & Nitta, N. V. 2006, A&A, 453, 335

Kliem, B. & Török, T. 2006, PhRvL, 96, 255002

Kosovichev, A. G., Schou, J., Scherrer, P. H., et al. 1997, SoPh, 170, 43

Kramar, M., Inhester, B., & Solanki, S. K. 2006, A&A, 456, 665

Leka, K. D., Barnes, G., Crouch, A. D., et al. 2009, SoPh, 260, 83

Lin, H., Kuhn, J. R., & Coulter, R. 2004, ApJ, 613, L177

Liu, R., Liu, C., Török, T., Wang, Y., & Wang, H. 2012, ApJ, 757, 150

Liu, R. & Wang, H. 2010, ApJ, 714, L41

Liu, R., Wang, H., & Alexander, D. 2009, ApJ, 696, 121

Low, B. C. & Lou, Y. Q. 1990, ApJ, 352, 343

Mackay, D. H., Karpen, J. T., Ballester, J. L., Schmieder, B., & Aulanier, G. 2010, ssr, 151, 333

Malanushenko, A., Schrijver, C. J., DeRosa, M. L., & Wheatland, M. S. 2014, ApJ, 783, 102

Marsh, G. E. 1992, Phys. Rev. A, 45, 7520

Martin, S. F., Livi, S. H. B., & Wang, J. 1985, AuJournalPh, 38, 929

Metcalf, T. R., De Rosa, M. L., Schrijver, C. J., et al. 2008, SoPh, 247, 269

Metcalf, T. R., Jiao, L., McClymont, A. N., Canfield, R. C., & Uitenbroek, H. 1995, ApJ, 439, 474

Metcalf, T. R., Leka, K. D., Barnes, G., et al. 2006, SoPh, 237, 267

Morse, P. M. & Feshbach, H. 1953, Methods of theoretical physics

Nakagawa, Y. & Raadu, M. A. 1972, SoPh, 25, 127

Priest, E. 2014, Magnetohydrodynamics of the Sun, 1st edn. (Cambridge University Press)

Priest, E. & Forbes, T. 2006, Magnetic Reconnection: MHD Theory and Applications (Cambridge University Press)

Pulkkinen, T. 2007, LRSP, 4

Qiu, J., Hu, Q., Howard, T. A., & Yurchyshyn, V. B. 2007, ApJ, 659, 758

Robbrecht, E., Berghmans, D., & Van der Linden, R. A. M. 2009, ApJ, 691, 1222

Rosenthal, C. S., Bogdan, T. J., Carlsson, M., et al. 2002, ApJ, 564, 508

Sakurai, T. 1982, SoPh, 76, 301

Sandman, A. W., Aschwanden, M. J., Derosa, M. L., Wülser, J. P., & Alexander, D. 2009, SoPh, 259, 1

Schmidt, H. U. 1964, NASSP, 50, 107

Schrijver, C. J., De Rosa, M. L., Metcalf, T. R., et al. 2006, SoPh, 235, 161

Schrijver, C. J., De Rosa, M. L., Title, A. M., & Metcalf, T. R. 2005, ApJ, 628, 501

Schrijver, C. J., DeRosa, M. L., Metcalf, T., et al. 2008, ApJ, 675, 1637

Schrijver, C. J., Kauristie, K., Aylward, A. D., et al. 2015, AdSR, 55, 2745

Schwenn, R. 2006, LRSP, 3

Seehafer, N. 1978, SoPh, 58, 215

Semel, M. 1967, AnAp, 30, 513

Shafranov, V. D. 1963, JNuE, 5, 251

Shen, J., Zhou, T., Ji, H., et al. 2014, ApJ, 791, 83

Shibata, K. & Magara, T. 2011, LRSP, 8

Simões, P. J. A., Fletcher, L., Hudson, H. S., & Russell, A. J. B. 2013, ApJ, 777, 152

Singer, H., Heckman, G., & Hirman, J. 2013, Space Weather Forecasting: A Grand Challenge (American Geophysical Union), 23–29

Solanki, S. K. & Hammer, R. 2002, The solar atmosphere, ed. J. A. Bleeker, J. Geiss, & M. C. E. Huber (Kluwer Academic Publishers), 1065

Spiegel, E. A. & Zahn, J.-P. 1992, A&A, 265, 106

Su, Y., van Ballegooijen, A., Lites, B. W., et al. 2009, ApJ, 691, 105

Sun, X., Hoeksema, J. T., Liu, Y., et al. 2012, ApJ, 748, 77

Teuber, D., Tandberg-Hanssen, E., & Hagyard, M. J. 1977, SoPh, 53, 97

Thalmann, J. K. & Wiegelmann, T. 2008, A&A, 484, 495

Titov, V. S. & Démoulin, P. 1999, A&A, 351, 707

Titov, V. S., Török, T., Mikic, Z., & Linker, J. A. 2014, ApJ, 790, 163

Török, T. & Kliem, B. 2004, PADEU, 14, 165

Török, T. & Kliem, B. 2005, ApJ, 630, L97

Török, T., Kliem, B., & Titov, V. S. 2004, A&A, 413, L27

Valori, G., Kliem, B., & Keppens, R. 2005, A&A, 433, 335

van Ballegooijen, A. A. & Martens, P. C. H. 1989, ApJ, 343, 971

Welsch, B. T., Fisher, G. H., & Sun, X. 2013, ApJ, 765, 98

Wheatland, M. S. 2007, SoPh, 245, 251

Wheatland, M. S., Sturrock, P. A., & Roumeliotis, G. 2000, ApJ, 540, 1150

Wiegelmann, T. 2004, SoPh, 219, 87

Wiegelmann, T. 2007, SoPh, 240, 227

Wiegelmann, T. & Inhester, B. 2003, SoPh, 214, 287

Wiegelmann, T., Inhester, B., & Sakurai, T. 2006, SoPh, 233, 215

Wiegelmann, T. & Neukirch, T. 2002, SoPh, 208, 233

Wiegelmann, T. & Neukirch, T. 2003, NPGeo, 10, 313

Wiegelmann, T. & Sakurai, T. 2012, LRSP, 9

Wiegelmann, T., Thalmann, J. K., & Solanki, S. K. 2014, A&ARv, 22, 78

Yan, Y. & Li, Z. 2006, ApJ, 638, 1162

Yang, W. H., Sturrock, P. A., & Antiochos, S. K. 1986, ApJ, 309, 383

Appendix A

Equations Concerning the Optimization Approach

Here we derive Eqs. (2.43) – (2.47). Varying

$$L = L_f + L_d, \tag{A.1}$$

where

$$L_f = \int_V B^2 w_f \boldsymbol{\Omega}_f^2 dV, \qquad L_d = \int_V B^2 w_d \boldsymbol{\Omega}_d^2 dV, \tag{A.2}$$

and

$$\boldsymbol{\Omega}_f = \frac{\mathbf{j}\times\mathbf{B}}{B^2} = \frac{(\nabla\times\mathbf{B})\times\mathbf{B}}{\mu_0 B^2}, \qquad \boldsymbol{\Omega}_d = \frac{(\nabla\cdot\mathbf{B})\mathbf{B}}{\mu_0 B^2}, \tag{A.3}$$

with respect to a iteration parameter t gives

$$\frac{dL}{dt} = \frac{dL_f}{dt} + \frac{dL_d}{dt}$$

We will consider $\frac{dL_f}{dt}$ and $\frac{dL_d}{dt}$ desperately. We start with obtaining an expression for $\frac{dL_f}{dt}$:

$$\begin{aligned}\frac{1}{2}\frac{dL_f}{dt} =& \int_V w_f \boldsymbol{\Omega}_\mathbf{f} \cdot \frac{\partial}{\partial t}\left(\frac{(\nabla\times\mathbf{B})\times\mathbf{B}}{\mu_0}\right) dV \\ & - \int_V w_f \boldsymbol{\Omega}_f^2 \mathbf{B}\cdot\frac{\partial\mathbf{B}}{\partial t} dV\end{aligned} \tag{A.4}$$

We will now rewrite every term in the above equation as a product with $\frac{\partial\mathbf{B}}{\partial t}$. Remark that the second term is already in this form. The first term can be rewritten as

$$\begin{aligned}\frac{1}{2}\frac{dL_f}{dt} =& \int_V \frac{w_f}{\mu_0} \boldsymbol{\Omega}_\mathbf{f} \cdot \left(\left(\nabla\times\frac{\partial\mathbf{B}}{\partial t}\right)\times\mathbf{B}\right) dV \\ & + \int_V \frac{w_f}{\mu_0} \boldsymbol{\Omega}_\mathbf{f} \cdot \left(\nabla\times\mathbf{B}\times\frac{\partial\mathbf{B}}{\partial t}\right) dV \\ & - \int_V w_f \boldsymbol{\Omega}_f^2 \mathbf{B}\cdot\frac{\partial\mathbf{B}}{\partial t} dV\end{aligned} \tag{A.5}$$

Applying the vector identity $\mathbf{a}\cdot(\mathbf{b}\times\mathbf{c}) = \mathbf{b}\cdot(\mathbf{c}\times\mathbf{a}) = \mathbf{c}\cdot(\mathbf{a}\times\mathbf{b})$ to the first and second term gives

$$\begin{aligned}\frac{1}{2}\frac{dL_f}{dt} =& \int_V \frac{w_f}{\mu_0}\left(\nabla \times \frac{\partial \mathbf{B}}{\partial t}\right) \cdot (\mathbf{B} \times \mathbf{\Omega_f})\,dV \\ &+ \int_V \frac{w_f}{\mu_0}\frac{\partial \mathbf{B}}{\partial t} \cdot (\mathbf{\Omega_f} \times (\nabla \times \mathbf{B}))dV \\ &- \int_V w_f \mathbf{\Omega}_f^2 \mathbf{B} \cdot \frac{\partial \mathbf{B}}{\partial t} dV.\end{aligned} \tag{A.6}$$

Remark that the second term is a product with $\frac{\partial \mathbf{B}}{\partial t}$ and has therefore the correct form. The first term needs some extra rewriting. Using the identity $(\nabla \times \mathbf{a}) \cdot \mathbf{b} = \mathbf{a} \cdot (\nabla \times \mathbf{b}) + \nabla \cdot (\mathbf{a} \times \mathbf{b})$, we get

$$\begin{aligned}\frac{1}{2}\frac{dL_f}{dt} =& -\int_V \frac{w_f}{\mu_0}\frac{\partial \mathbf{B}}{\partial t} \cdot (\nabla \times (\mathbf{\Omega_f} \times \mathbf{B}))\,dV \\ &- \int_V \frac{w_f}{\mu_0}\nabla \cdot \left((\mathbf{\Omega_f} \times \mathbf{B}) \times \frac{\partial \mathbf{B}}{\partial t}\right) dV \\ &+ \int_V \frac{w_f}{\mu_0}\frac{\partial \mathbf{B}}{\partial t} \cdot (\mathbf{\Omega_f} \times (\nabla \times \mathbf{B}))dV \\ &- \int_V w_f \mathbf{\Omega}_f^2 \mathbf{B} \cdot \frac{\partial \mathbf{B}}{\partial t} dV.\end{aligned} \tag{A.7}$$

Only the second term is not yet a product of $\frac{\partial \mathbf{B}}{\partial t}$. To proceed, we apply the identity $f\nabla \cdot \mathbf{a} = \nabla \cdot (f\mathbf{a}) - \mathbf{a} \cdot \nabla f$ to this term:

$$\begin{aligned}\frac{1}{2}\frac{dL_f}{dt} =& -\int_V \frac{w_f}{\mu_0}\frac{\partial \mathbf{B}}{\partial t} \cdot (\nabla \times (\mathbf{\Omega_f} \times \mathbf{B}))\,dV \\ &- \int_V \nabla \cdot \left(\frac{w_f}{\mu_0}(\mathbf{\Omega_f} \times \mathbf{B}) \times \frac{\partial \mathbf{B}}{\partial t}\right) dV \\ &+ \int_V \frac{1}{\mu_0}\left((\mathbf{\Omega_f} \times \mathbf{B}) \times \frac{\partial \mathbf{B}}{\partial t}\right) \cdot \nabla w_f \\ &+ \int_V \frac{w_f}{\mu_0}\frac{\partial \mathbf{B}}{\partial t} \cdot (\mathbf{\Omega_f} \times (\nabla \times \mathbf{B}))dV \\ &- \int_V w_f \mathbf{\Omega}_f^2 \mathbf{B} \cdot \frac{\partial \mathbf{B}}{\partial t} dV.\end{aligned} \tag{A.8}$$

Applying Gauss law to the second term results in

$$\begin{aligned}\frac{1}{2}\frac{dL_f}{dt} =& -\int_V \frac{w_f}{\mu_0}\frac{\partial \mathbf{B}}{\partial t} \cdot (\nabla \times (\mathbf{\Omega_f} \times \mathbf{B}))\,dV \\ &- \int_S \hat{\boldsymbol{n}} \cdot \left(\frac{w_f}{\mu_0}(\mathbf{\Omega_f} \times \mathbf{B}) \times \frac{\partial \mathbf{B}}{\partial t}\right) dV \\ &+ \int_V \frac{1}{\mu_0}\left((\mathbf{\Omega_f} \times \mathbf{B}) \times \frac{\partial \mathbf{B}}{\partial t}\right) \cdot \nabla w_f dS \\ &+ \int_V \frac{w_f}{\mu_0}\frac{\partial \mathbf{B}}{\partial t} \cdot (\mathbf{\Omega_f} \times (\nabla \times \mathbf{B}))dV \\ &- \int_V w_f \mathbf{\Omega}_f^2 \mathbf{B} \cdot \frac{\partial \mathbf{B}}{\partial t} dV.\end{aligned} \tag{A.9}$$

Again applying the vector identity $\mathbf{a} \cdot (\mathbf{b} \times \mathbf{c}) = \mathbf{c} \cdot (\mathbf{a} \times \mathbf{b})$ to the second and third term gives

$$\begin{aligned}\frac{1}{2}\frac{dL_f}{dt} =& -\int_V \frac{w_f}{\mu_0}\left(\nabla\times(\mathbf{\Omega_f}\times\mathbf{B})\right)\cdot\frac{\partial\mathbf{B}}{\partial t}dV\\ &-\int_S \frac{w_f}{\mu_0}\left(\hat{\boldsymbol{n}}\times(\mathbf{\Omega_f}\times\mathbf{B})\right)\cdot\frac{\partial\mathbf{B}}{\partial t}dS\\ &+\int_V \frac{1}{\mu_0}\left(\nabla w_f\times(\mathbf{\Omega_f}\times\mathbf{B})\right)\cdot\frac{\partial\mathbf{B}}{\partial t}dV\\ &+\int_V \frac{w_f}{\mu_0}(\mathbf{\Omega_f}\times(\nabla\times\mathbf{B}))\cdot\frac{\partial\mathbf{B}}{\partial t}dV\\ &-\int_V w_f\mathbf{\Omega}_f^2\mathbf{B}\cdot\frac{\partial\mathbf{B}}{\partial t}dV.\end{aligned} \tag{A.10}$$

We see that every term in this expression is now a product of $\frac{\partial\mathbf{B}}{\partial t}$.

Next we search an expression for $\frac{\partial L_d}{\partial t}$ as a summation of terms that are a product of $\frac{\partial\mathbf{B}}{\partial t}$:

$$\begin{aligned}\frac{1}{2}\frac{dL_d}{dt} =& \int_V \frac{w_d}{\mu_0}\mathbf{\Omega_d}\cdot\frac{\partial}{\partial t}\left((\nabla\cdot\mathbf{B})\mathbf{B}\right)dV\\ &-\int_V \left(w_d\mathbf{\Omega}_d^2\right)\mathbf{B}\cdot\frac{\partial\mathbf{B}}{\partial t}dV,\end{aligned} \tag{A.11}$$

or,

$$\begin{aligned}\frac{1}{2}\frac{dL_d}{dt} =& \int_V \frac{w_d}{\mu_0}\left(\mathbf{\Omega_d}\cdot\mathbf{B}\right)\nabla\cdot\frac{\partial\mathbf{B}}{\partial t}dV\\ &+\int_V \frac{w_d}{\mu_0}\left(\mathbf{\Omega_d}(\nabla\cdot\mathbf{B})\right)\cdot\frac{\partial\mathbf{B}}{\partial t}dV\\ &-\int_V \left(w_d\mathbf{\Omega}_d^2\right)\mathbf{B}\cdot\frac{\partial\mathbf{B}}{\partial t}dV\end{aligned} \tag{A.12}$$

Applying the identity $f\nabla\cdot\mathbf{a} = \nabla\cdot(f\mathbf{a}) - \mathbf{a}\cdot\nabla f$ to the first term, and identity $(\nabla\times\mathbf{a})\cdot\mathbf{b} = \mathbf{a}\cdot(\nabla\times\mathbf{b}) + \nabla\cdot(\mathbf{a}\times\mathbf{b})$ to the second and third term gives:

$$\begin{aligned}\frac{1}{2}\frac{dL_d}{dt} =& -\int_V \frac{w_d}{\mu_0}\nabla\left(\mathbf{\Omega_d}\cdot\mathbf{B}\right)\cdot\frac{\partial\mathbf{B}}{\partial t}dV\\ &+\int_V \frac{w_d}{\mu_0}\nabla\cdot\left((\mathbf{\Omega_d}\cdot\mathbf{B})\frac{\partial\mathbf{B}}{\partial t}\right)dV\\ &+\int_V \frac{w_d}{\mu_0}\left(\mathbf{\Omega_d}(\nabla\cdot\mathbf{B})\right)\cdot\frac{\partial\mathbf{B}}{\partial t}dV\\ &-\int_V \left(w_d\mathbf{\Omega}_d^2\right)\mathbf{B}\cdot\frac{\partial\mathbf{B}}{\partial t}dV\end{aligned} \tag{A.13}$$

Again applying the identity $f\nabla\cdot\mathbf{a} = \nabla\cdot(f\mathbf{a}) - \mathbf{a}\cdot\nabla f$, but this time on the third term, leads to

$$\begin{aligned}\frac{1}{2}\frac{dL_d}{dt} =& -\int_V \frac{w_d}{\mu_0}\nabla\left(\mathbf{\Omega_d}\cdot\mathbf{B}\right)\cdot\frac{\partial\mathbf{B}}{\partial t}dV\\ &+\int_V \nabla\cdot\left(\frac{w_d}{\mu_0}(\mathbf{\Omega_d}\cdot\mathbf{B})\frac{\partial\mathbf{B}}{\partial t}\right)dV\\ &+\int_V \frac{1}{\mu_0}\left(\mathbf{\Omega_d}(\nabla\cdot\mathbf{B})\nabla w_d\right)\cdot\frac{\partial\mathbf{B}}{\partial t}dV\\ &-\int_V \left(w_d\mathbf{\Omega}_d^2\right)\mathbf{B}\cdot\frac{\partial\mathbf{B}}{\partial t}dV\end{aligned} \tag{A.14}$$

Applying Gauss' theorem to the second term gives

$$\begin{aligned}\frac{1}{2}\frac{dL_d}{dt} = &-\int_V \frac{w_d}{\mu_0}\nabla\left(\boldsymbol{\Omega}_{\mathbf{d}}\cdot\mathbf{B}\right)\cdot\frac{\partial\mathbf{B}}{\partial t}dV \\ &+\int_S \hat{\boldsymbol{n}}\cdot\left(\frac{w_d}{\mu_0}(\boldsymbol{\Omega}_{\mathbf{d}}\cdot\mathbf{B})\frac{\partial\mathbf{B}}{\partial t}\right)dS \\ &+\int_V \frac{1}{\mu_0}\left(\boldsymbol{\Omega}_{\mathbf{d}}(\nabla\cdot\mathbf{B})\nabla w_d\right)\cdot\frac{\partial\mathbf{B}}{\partial t}dV \\ &-\int_V \left(w_d\boldsymbol{\Omega}_d^2\right)\mathbf{B}\cdot\frac{\partial\mathbf{B}}{\partial t}dV\end{aligned} \tag{A.15}$$

Remark that all terms have been written as a product of $\frac{\partial\mathbf{B}}{\partial t}$. We can now combine Eq. (A.10) with Eq. (A.15) to obtain an expression for dL/dt:

$$\frac{1}{2}\frac{\partial L}{\partial t} = -\int_V \frac{\partial\mathbf{B}}{\partial t}\cdot\mathbf{F}dV - \int_S \frac{\partial\mathbf{B}}{\partial t}\cdot\mathbf{G}dS, \tag{A.16}$$

where

$$\mathbf{F}_{\text{opt}} = \frac{1}{\mu_0}\left(\boldsymbol{\Omega}_f\times\mathbf{B}\right)\times\nabla w_f + \frac{1}{\mu_0}\left(\boldsymbol{\Omega}_d\cdot\mathbf{B}\right)\nabla w_d + w_f\mathbf{F}_f + w_d\mathbf{F}_d, \tag{A.17}$$

$$\mathbf{G}_{\text{opt}} = w_f\hat{\boldsymbol{n}}\times\left(\boldsymbol{\Omega}_f\times\mathbf{B}\right) - w_d\hat{\boldsymbol{n}}(\boldsymbol{\Omega}\cdot\mathbf{B}), \tag{A.18}$$

with

$$\mathbf{F}_f = \frac{1}{\mu_0}\nabla\times\left(\boldsymbol{\Omega}_f\times\mathbf{B}\right) + \mathbf{j}\times\boldsymbol{\Omega}_f + \boldsymbol{\Omega}_f^2\mathbf{B} \tag{A.19}$$

$$\mathbf{F}_d = -\frac{1}{\mu_0}\left(\nabla\cdot\mathbf{B}\right)\boldsymbol{\Omega}_{\mathbf{d}} + \frac{1}{\mu_0}\nabla\left(\boldsymbol{\Omega}_d\cdot\mathbf{B}\right) + \boldsymbol{\Omega}_d^2\mathbf{B} \tag{A.20}$$

DEPARTEMENT OF PHYSICS AND ASTRONOMY
Celestijnenlaan 200d bus 2412
3001 HEVERLEE, BELGIË
tel. + 32 16 32 71 24
fys.kuleuven.be